

Elevated temperature thermo-mechanical behaviour of cast irons : a numerical-experimental investigation

Citation for published version (APA):

Pina, J. C. (2015). *Elevated temperature thermo-mechanical behaviour of cast irons : a numerical-experimental investigation*. [Phd Thesis 1 (Research TU/e / Graduation TU/e), Mechanical Engineering]. Technische Universiteit Eindhoven.

Document status and date:

Published: 01/01/2015

Document Version:

Publisher's PDF, also known as Version of Record (includes final page, issue and volume numbers)

Please check the document version of this publication:

- A submitted manuscript is the version of the article upon submission and before peer-review. There can be important differences between the submitted version and the official published version of record. People interested in the research are advised to contact the author for the final version of the publication, or visit the DOI to the publisher's website.
- The final author version and the galley proof are versions of the publication after peer review.
- The final published version features the final layout of the paper including the volume, issue and page numbers.

[Link to publication](#)

General rights

Copyright and moral rights for the publications made accessible in the public portal are retained by the authors and/or other copyright owners and it is a condition of accessing publications that users recognise and abide by the legal requirements associated with these rights.

- Users may download and print one copy of any publication from the public portal for the purpose of private study or research.
- You may not further distribute the material or use it for any profit-making activity or commercial gain
- You may freely distribute the URL identifying the publication in the public portal.

If the publication is distributed under the terms of Article 25fa of the Dutch Copyright Act, indicated by the "Taverne" license above, please follow below link for the End User Agreement:

www.tue.nl/taverne

Take down policy

If you believe that this document breaches copyright please contact us at:

openaccess@tue.nl

providing details and we will investigate your claim.

**Elevated temperature thermo-mechanical
behaviour of cast irons:
a numerical-experimental investigation**

Juan Carlos Pina

Elevated temperature thermo-mechanical behaviour of cast irons:
a numerical-experimental investigation
by Juan Carlos Pina - Eindhoven, The Netherlands
Technische Universiteit Eindhoven, 2015 – Proefschrift.

A catalogue record is available from the Eindhoven University of Technology
Library.
ISBN: 978-94-91909-23-8

Cover image: Nodular cast iron microstructure, courtesy of Marc van Maris.

Typeset by the author with the L^AT_EX documentation system.
Cover design: María Gabriela Molinari
Printed by: Proefschriftmaken.nl || Uitgeverij BOXPress

This research was carried out under the project number MC2.06270 in the
framework of the Research Program of the Materials innovation institute (M2i)
(www.m2i.nl).

© Copyright, 2015, Juan Carlos Pina. All rights reserved.

Elevated temperature thermo-mechanical behaviour of cast irons: a numerical-experimental investigation

PROEFSCHRIFT

ter verkrijging van de graad van doctor aan de Technische
Universiteit Eindhoven, op gezag van de rector magnificus
prof.dr.ir. F.P.T. Baaijens, voor een commissie aangewezen
door het College voor Promoties, in het openbaar te
verdedigen op woensdag 13 mei 2015 om 14:00 uur

door

Juan Carlos Pina

geboren te Mendoza, Argentinië

Dit proefschrift is goedgekeurd door de promotoren en de samenstelling van de promotiecommissie is als volgt:

voorzitter:	prof.dr.ir. L.P.H. de Goey
1e promotor:	prof.dr.ir. M.G.D. Geers
copromotor(en):	dr.ir. V.G. Kouznetsova
leden:	prof.dr.-ing. W. Bleck (RWTH Aachen)
	prof.dr.ir. J.P. Ponthot (Université de Liège)
	prof.dr. J. Sietsma (TU Delft)
	dr.ir. J.A. van Oijen
adviseur(s):	dr.ir. J. Zijp (DAF Trucks NV)

**“Nunca, que no digan nunca,
porque un día de estos nos verán sonriendo.”**

Karamelo Santo, Nunca

Contents

Contents	i
Summary	iii
1 Introduction	1
1.1 Background and motivation	1
1.2 Mechanical and thermo-mechanical behaviour of cast irons	3
1.3 Brief account of different approaches used for modelling of cast irons	5
1.4 Scope and objective	6
1.5 Outline of the thesis	7
2 Thermo-mechanical analyses of heterogeneous materials	9
2.1 Introduction	9
2.2 Microstructural model	11
2.3 Isothermal mechanical analyses	16
2.4 Thermo-mechanical analyses: uniform temperature distribution . . .	20
2.5 Thermo-mechanical analyses: non-uniform temperature distribution	30
2.6 Conclusions	34
3 Microstructural study of the mechanical response of CGI	37
3.1 Introduction	37
3.2 Experimental procedure	39
3.3 Numerical simulations	45
3.4 Conclusions	51
4 Elevated temperature creep of pearlitic steels	55
4.1 Introduction	55
4.2 Elevated temperature tests on pearlitic steels	57
4.3 Thermo-viscoplastic model for pearlitic steels	59
4.4 Stress update algorithm - Numerical implementation	68
4.5 Parameter identification	70
4.6 Assessment of the model performance under uniaxial loading conditions	72
4.7 Conclusions	74
5 Time-dependent thermo-mechanical analyses of cast irons	77
5.1 Introduction	77

5.2	CGI microstructural model	79
5.3	Numerical simulations on CGI RVE	87
5.4	Conclusions	92
6	Conclusions and recommendations	95
6.1	Cast iron microstructural model	95
6.2	Summary of the results	96
6.3	Recommendations for future developments	98
A	Tensor and vector operation notation	101
B	2D computational homogenization	103
C	3D thermo-mechanical computational homogenization	107
C.1	Macro-to-micro scale transition	107
C.2	Micro-to-macro scale transition	109
D	Rule of mixture and Turner’s model	111
E	CTE and elastic mismatch study	113
F	Thermo-viscoplastic model Jacobian terms and derivatives	117
G	Thermo-viscoplastic model finite element implementation	119
G.1	Linearization	121
G.2	Stress update algorithm	122
G.3	Element tangent stiffness matrix	125
	Bibliography	129
	Acknowledgments	141
	Curriculum Vitae	143

Summary

Elevated temperature thermo-mechanical behaviour of cast irons: a numerical-experimental investigation

Nowadays, in many elevated temperature engineering applications demanding thermal and mechanical conditions are present. Therefore, a material which possesses a good combination of mechanical and thermal properties is required. This is the case of cast iron making it a frequent choice for components operating in challenging thermo-mechanical conditions.

The efficient design of these engineering components requires a deep understanding of the material mechanical and thermo-mechanical behaviour. Furthermore, in the case of diesel engine components with the continuous rise of the engine operating temperatures (to yield cleaner emissions), there is an increasing need for accurate models than can predict the response of the material at both the macro and micro levels. In the case of cast iron, the complex and heterogeneous microstructure makes the understanding and prediction of its thermo-mechanical behaviour very challenging.

In this work, a microstructure based modelling approach is followed to study the thermo-mechanical behaviour of two types of cast iron: *Flake or Lamellar Graphite Iron (FGI)* and *Compacted or Vermicular Graphite Iron (CGI)*. This approach makes possible to assess the impact the different microstructural features have on the material local and overall response. For example, it allows to study how some inherently microstructural process, such as damage initiation, are influenced by the different microstructural features found in cast iron. Moreover, when required, experiments have been performed to validate some of the fundamental modelling assumptions as well as to provide input for the model.

First, a microstructural model for FGI is introduced to study the response of the material under mechanical and thermo-mechanical loading conditions. To this end, the coupling between the mechanical and thermal fields and the influence of temperature on the mechanical and thermal properties of the microconstituents are incorporated. The complex microstructure of lamellar cast iron, is represented here by an idealized unit cell model that captures the main morphological features of the material, such as the sharpness and the 3D connectivity of the graphite inclusions. This simplified representation of the microstructure makes it possible to investigate the influence of different microstructural features and complex mechanical and thermo-mechanical loads on the local and macroscopic response of the material. The results indicate that graphite anisotropy plays a key role in the mechanical, thermal and thermo-

mechanical response of FGI at the micro and macro level.

The following chapter is focussed on understanding the micro-mechanics of CGI and in particular the role played by graphite anisotropy. The aim is to address how important is the mechanical anisotropy of graphite for the distribution of strains and deformation in the vermicular graphite particle. For that reason, an experimental-numerical approach is used to study the deformation of the graphite inclusions within CGI. First a set of in-situ micro-tensile tests on CGI samples are carried out in the scanning electron microscope (SEM). From these tests, high resolution images of the deforming graphite particles within CGI are obtained. These images are then used to calculate the strains within the graphite particles via a novel Global Digital Image Correlation (GDIC) procedure. The results from the test confirmed the mechanical anisotropy of vermicular graphite particles in cast irons. The second part of the chapter is dedicated to the development and analyses of 2D CGI microstructural models to computationally evaluate the influence of graphite anisotropy in CGI's mechanical behaviour. The SEM micrographs obtained from the tests are then used to create 2D CGI microstructural models. Good qualitative agreement is found between the computed strains within the graphite particles and the experimentally measured ones, validating the hypothesis that graphite is mechanically anisotropic in vermicular graphite particles. Moreover, a comparative analysis on the effect of the graphite anisotropy on the matrix response is performed, revealing that graphite anisotropy has a high impact on the micromechanical response of CGI. Therefore, it should not be neglected in order to accurately predict stress and strains distribution at the microstructural level.

Then, the elevated temperature creep of pearlite and/or pearlitic steels is investigated. The matrix material in cast irons is generally composed of a ferrite/pearlite mixture. When a higher strength cast iron is required, this mixture becomes predominantly pearlitic such as in the CGI used in diesel engine components. Therefore, understanding the time and temperature dependent behaviour of pearlite at temperatures corresponding to the diesel engine operating temperatures becomes instrumental in predicting the behaviour of cast irons in such conditions. In this chapter, an experimental-numerical approach is used to study the mechanical response of pearlitic steels in the temperature range 20 – 500 °C. A finite strain thermo-viscoplastic model is presented together with a set of elevated temperature tests (tensile and creep tests). The aim of the tests is twofold: first to provide insight in the elevated temperature mechanical response of the material; and second, to provide the data required to identify the corresponding material parameters. Furthermore, the model and the experimental data are instrumental in showing that the influence of temperature on the mechanical behaviour of pearlitic steels becomes significant for temperatures above 350 – 400 °C. Consequently, at this temperature level, pearlite no longer exhibits its well known room temperature structural integrity and creep resistance.

Finally, a new microstructural model for thermo-mechanical analyses of CGI is introduced which can be used for transient conditions such as the ones present in diesel engines during their operating life in the temperature range between 20 – 500 °C. The time and temperature dependency is incorporated in the model by means of the pearlite thermo-viscoplastic model. The aim is to investigate the time dependent

response of CGI for temperatures up to 500 °C. The results show that the effect of temperature on the mechanical response of CGI is dominant for temperatures above 350 °C. Furthermore, as the temperature is increased, the combined effect of time, temperature and cast iron microstructural heterogeneity enhances plastic deformation and damage evolution hereby reducing the time to failure of the material.

Introduction

1.1 Background and motivation

Good thermal properties, i.e. a high thermal conductivity and low thermal expansion coefficient, make cast irons ideal candidates for industrial applications in which a combination of these properties is required, e.g. in diesel engines for power generation used in automotive, marine and locomotive industries. In these applications, engine components like cylinder heads and blocks and exhaust manifolds are subjected to elevated temperature cycles during their operating life. Under these conditions, a high thermal conductivity, which enables fast heat transport, is required to reduce thermal gradients within the component.

Cast irons employed in cylinder heads are subjected to frequent temperature changes in the start-stop cycles of the engine. These conditions produce thermal expansion, which in constrained components, such as the cylinder head, give rise to high compressive stresses upon heating. Depending on the upper cycle temperature and dwell times, plastic deformation and stress relaxation in compression takes place during the hot part of the thermal cycle. Therefore, residual tensile stresses may develop when the component is cooled down (Figure 1.1). For high temperatures and long dwell times, the repetition of the heating and cooling cycles ultimately leads to cracking and Thermo-Mechanical Fatigue (TMF) failure of a component.

Cast irons are carbon-iron alloys in which the carbon content is above 2.14 in weight percentage (wt%). The high carbon content induces a microstructure composed of graphite inclusions surrounded by a ferrite/pearlite matrix, whereby the morphology of the graphite inclusions is defined by the chemical composition and cooling rate of the casting. Depending on this morphology cast irons can be classified as: *Nodular or Spheroidal Graphite Iron (SGI)*; *Compacted or Vermicular Graphite Iron (CGI)* and *Flake or Lamellar Graphite Iron (FGI)* (Figure 1.2) [125]. The morphology of the graphite inclusions plays a fundamental role in the resulting mechanical and thermal properties of the cast iron [44,116]. In CGI and FGI, the graphite inclusions form a 3D interconnected network which together with graphite's high thermal conductivity leads to thermal properties that out perform those found in steels. Conversely, the 3D interconnected network of graphite inclusions proves to be detrimental for the

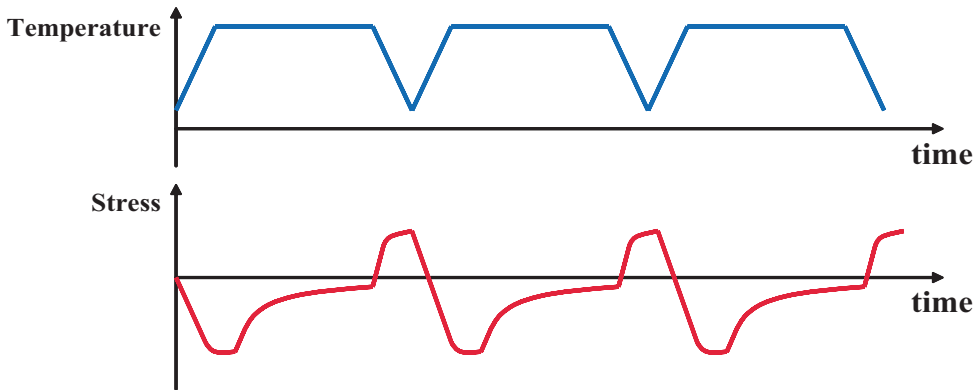
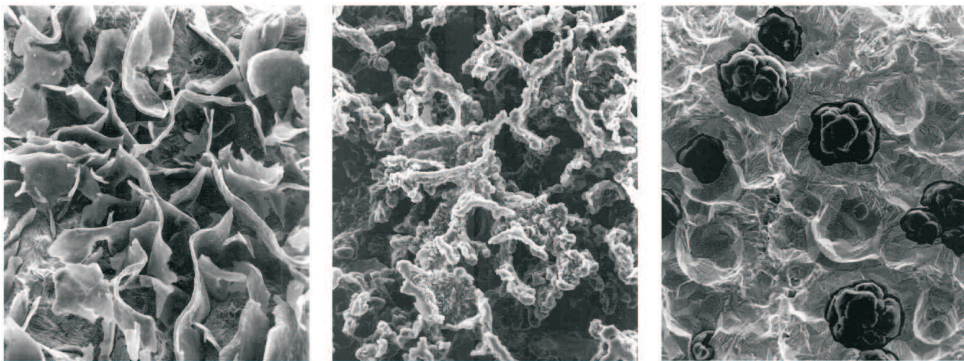


Figure 1.1: Schematic representation of thermal stresses developing during thermal cycling.

mechanical response of the material. Due to the graphite/matrix elastic and thermal mismatch and the sharp edges in the graphite inclusions, stress concentrations at the graphite/matrix interface occur, whereby the interface is a preferential location for crack initiation and propagation. Once crack propagation starts, the weaker graphite/matrix interface along the 3D network of graphite inclusions becomes the natural path for further crack growth. This makes CGI and FGI, in general, weaker and more brittle than steels. On the contrary, in SGI the graphite inclusions are present in the form of isolated graphite nodules. This yields a material with high ductility and strength but with thermal properties similar to those of steels.



a) Flake graphite.

b) Compacted graphite.

c) Spheroidal graphite.

Figure 1.2: Graphite morphologies of different cast irons: a) Flake or Lamellar Graphite Iron (FGI), b) Compacted or Vermicular Graphite Iron (CGI) and c) Nodular or Spheroidal Graphite Iron (SGI) [125].

Besides the morphology of graphite inclusions, the structure of the matrix has an

essential influence on the mechanical properties of cast irons (Figure 1.3) [126]. The ferrite/pearlite content influences the strength, ductility, microstructural stability and creep strength of the iron matrix. A predominantly ferritic matrix leads to a lower ultimate strength and a higher ductility. As the pearlite content increases, the response of the cast iron shifts from ductile to brittle, where a fully pearlitic matrix reveals a high ultimate strength and low ductility [73,126]. At temperatures above room temperature, creep strength and microstructural stability become relevant for the mechanical response of the cast irons. For that reason, a pearlitic matrix with a higher creep strength than ferrite, is preferred for elevated or high temperature applications. However, one drawback of pearlite is that for temperatures higher than 500 °C, the microstructure tends to become unstable [18, 56–58, 78, 114, 145, 151]. Depending on the temperature level and dwell time, pearlite can decompose into ferrite and graphite which weakens the matrix. Ferritic cast irons are microstructurally more stable at elevated temperatures because they are not affected by this problem.

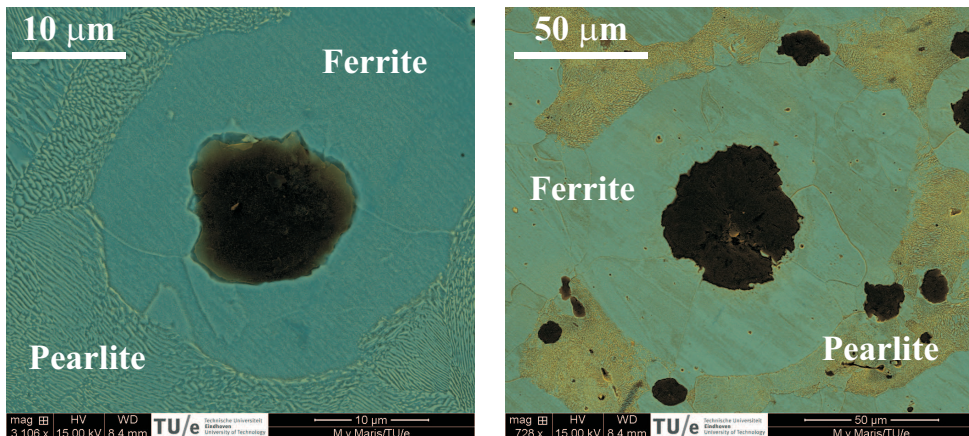


Figure 1.3: Matrix structure in a nodular cast iron: ferrite, pearlite and spheroidal graphite inclusions.

1.2 Mechanical and thermo-mechanical behaviour of cast irons

The efficient design of engineering components operating at elevated temperatures requires a deep understanding of the material mechanical and thermo-mechanical response. In the case of cast iron, the complex and heterogeneous microstructure makes the understanding and prediction of its behaviour challenging. Different microstructural features, like graphite morphology, graphite anisotropy, the graphite/matrix interface, the time and temperature dependent properties of the different phases and the elastic mismatch between the graphite and the matrix will determine the response of the material. For this reason, a proper understanding

of the relevant microstructural phenomena is required for a good estimation of its mechanical and thermo-mechanical behaviour.

From a mechanical point of view, various references [1, 2, 14, 19, 28–30, 71, 73, 84, 116, 121, 128] can be found in the literature that analysed the influence of different microstructural features (e.g. graphite morphology and volume fraction, ferrite/pearlite volume fraction) on the macroscopic response of cast irons. Also, work has been done to understand the process of damage initiation and propagation at the microstructural level [33, 35, 38, 41, 62, 73]. The two major factors affecting crack initiation seem to be the weak interface and the graphite/matrix elastic mismatch. The latter implies that, when loaded, the matrix and the graphite will deform in an incompatible manner, leading to stress concentrations and consequently crack initiation at the interface. Moreover, in case the interface proves to be stronger than the bonding between the graphite basal planes, the crack will nucleate in between the graphite planes.

In spite of the extensive amount of work in the literature on the micro-mechanical behaviour of nodular cast iron [33, 35, 38, 41, 62, 73], only few papers can be found that focussed on the study of lamellar [33, 62] and vermicular graphite irons [127]. Furthermore, the influence of graphite anisotropy on the mechanical and thermal response of cast iron has been scarcely examined in the past [41, 66].

Several investigations have been carried out to understand the various phenomena that influence the response of cast irons while operating at high temperatures. The studies looked into the effect of temperature on the mechanical [21–23, 44, 56–58, 78, 91, 113, 114, 151] and thermal [65, 68] properties of cast irons. The detrimental effect of an increased temperature on the mechanical properties is less evident in lamellar graphite iron compared to nodular and vermicular graphite irons, due to the moderate mechanical properties of lamellar graphite iron at room temperature. Besides the impact on the mechanical and thermal properties, temperature can also activate other processes such as pearlite decomposition, oxidation and creep [18, 56–58, 78, 99, 106, 114, 145, 149, 151, 154], which can accelerate the failure of the material. In general, temperature in excess of 500 °C and long exposure times are required for pearlite decomposition and oxidation to become relevant [18, 56–58, 78, 99, 106, 145, 149, 151, 154]. Significant creep or stress relaxation rates are observed, depending on the dwell time and stress or strain level, for temperatures above 400 to 450 °C [57, 58, 99, 106, 114, 149].

Finally, studies on cast iron TMF can also be found in the literature [18, 51, 56–58, 111, 114, 146, 154]. These studies suggest that under TMF conditions, the response of the material is driven by the upper cycle temperature and dwell time. These two parameters control the thermal stress cycle and consequently the residual stresses accumulating after each thermal cycle. TMF is affected by thermal expansion, thermal conductivity, elasticity constants, high temperature strength, creep and stress relaxation [58]. In addition, damage may be further accelerated by pearlite decomposition and oxidation, which are controlled by the upper cycle temperature, dwell time and chemical composition.

1.3 Brief account of different approaches used for modelling of cast irons

Different approaches have been followed in the past to investigate the mechanical, thermal and thermo-mechanical behaviour of cast irons. Phenomenological models have been used to predict the mechanical response of cast irons in the elastic and plastic regimes [6, 24, 42, 64, 76]. Gurson type models have been used to study the influence of damage on the mechanical response of nodular graphite iron [10, 54, 55, 86, 129], where it is assumed that after interface debonding the graphite nodules can be considered as voids. In recent years, more elaborate models have been developed to describe the behaviour of cast irons under complex thermo-mechanical conditions such as relevant for TMF [52, 118, 119, 134–136]. These models combine various ingredients (viscoplasticity, kinematic hardening, damage, etc.) to predict the time and temperature dependent cyclic plastic deformation of cast irons subjected to thermo-mechanical cycling. The main drawback of these models, is that they generally include a considerable amount of material parameters which need to be obtained via a tedious parameter identification processes. This requires a large amount of experimental data, which needs to be gathered from specific tests covering the entire spectrum of thermo-mechanical loading conditions. For each variation of graphite morphology, volume fraction and metal matrix composition, the entire testing procedure and parameter identification procedure has to be repeated again, making this a time-consuming and expensive process.

Following a different path, analytical models have been employed in the past to estimate the elastic [16, 33, 41, 43, 50] and thermal properties [63, 67] of cast irons. Different techniques such as Reuss and Voigt bounds, Hashin-Shtrikman bounds and self-consistent methods have been considered in these studies. In general, in these (semi)-analytical methods, cast irons are considered as two phase materials composed of isotropic or anisotropic graphite inclusions embedded in an isotropic metal matrix, whereby the influence of the particle shape is taken into account through the particle aspect ratio. The main limitation of these (semi)-analytical methods is that the interaction between individual particles is restricted and a perfect adhesion between graphite particles and metal matrix has to be assumed. The limited interaction between particles is a reasonable assumption for nodular cast iron, where the graphite inclusions are nearly isolated nodules, but this does not hold for lamellar and compacted cast irons with an interconnected graphite structure.

Microstructural modelling has been used to investigate the mechanical behaviour of cast irons. In the case of nodular cast iron, several finite element (FE) unit cell and microstructural models have been introduced in the literature to study the mechanical response of the material within its elastic and elasto-plastic regimes [17, 25–27, 31, 41, 82, 129]. However, the application of this approach to study lamellar and compacted cast irons is scarce, mostly due to the geometrical complexity of their microstructure. For the analysis of the mechanical response of compacted cast iron a direct discretization of 2D micrographs [47, 88, 89, 97] or a model of slender ellipsoids [50] has been used. Velichko *et al.* [144] have used focused ion beam (FIB) tomography images in a FE analysis to obtain the overall thermal and electrical conductivity of lamellar cast iron. Although the tomography-based

model is a geometrically exact representation of a small part of the microstructure, it becomes prohibitively computationally expensive if anisotropic and/or non-linear material properties are to be included.

1.4 Scope and objective

The objective of this thesis is to develop a time and temperature dependent microstructural model to study the thermo-mechanical behaviour of cast irons in the temperature range from 20 to 500 °C. A microstructural modelling approach is chosen because it allows to incorporate a broad spectrum of microstructural features in a straightforward manner. Furthermore, it is a practical tool to assess the impact of microstructural variations on the material local and global response. Current cast iron microstructural models available in the literature focus either on quasi-static mechanical conditions [17, 31, 41, 47, 82, 129] or high strain rate applications (i.e. machining) [25–27, 88, 89, 97]. Within the literature reviewed, no micromechanical models have been developed for elevated temperature mechanical conditions such as those present in engine components. The development of such a model, requires first to identify the microstructural features that dominate the response of the material. The following main drivers are here identified for the mechanical, thermal and thermo-mechanical response of cast irons:

- Morphology and volume fraction of the graphite particles.
- Matrix composition (ferrite/pearlite volume fraction).
- Constitutive behaviour of the different phases, graphite and matrix.
- Constitutive behaviour of the graphite/matrix interface.
- Temperature dependency of the mechanical and thermal properties.

In the microstructural models of nodular cast irons [17, 31, 41, 82] and compacted cast irons [47, 97], the graphite has until now been considered as an isotropic material and the values assigned to its elastic constants vary significantly between the different references. However, experimental observations of the structure of the graphite particles within cast iron provide clear evidence of a layered structure, mechanically strong in the “in-plane” direction and weak in the “out-of-plane” direction [35, 44, 60, 66, 94, 122, 144]. This layered structure suggests that graphite as found in cast irons, should reveal a certain degree of anisotropy in its mechanical and thermal properties. This hypothesis will be investigated here. Also, the importance of the anisotropy of the graphite particles on the mechanical and thermal behaviour of cast irons will be assessed.

In addition, for the temperature range considered here, several references [56–58, 106, 114, 118, 119, 149] suggest that cast irons are susceptible to creep and stress relaxation. As a consequence, the microstructural model should be able to predict time dependent response related to creep. In this work this time dependency will be incorporated via the matrix constitutive behaviour. Because in higher strength cast irons, such as CGI, the matrix material is predominantly pearlitic, focus will be

put on the time and temperature dependent behaviour of pearlite at temperatures between 20 to 500 °C.

To summarize, in this thesis the subsequent topics will be addressed:

- A microstructural model for cast irons will be developed that incorporates *(i)* the morphology and volume fraction of the graphite phase, *(ii)* the ferrite/pearlite volume fraction of the matrix, *(iii)* the constitutive behaviour, *(iv)* the temperature dependency of the mechanical and thermal properties of the different phases and *(v)* the constitutive behaviour of the interface.
- The mechanical anisotropy of the graphite particles will be investigated via numerical simulations and in-situ experiments.
- The elevated temperature creep of pearlite will be studied, for which a thermo-viscoplastic model for this will be proposed. This model will then be incorporated into the cast iron microstructural model.
- The response of cast irons under several mechanical and thermal conditions will be investigated.

Concerning the constitutive behaviour of the graphite/matrix interface, quantitative data on the interface behaviour is still lacking. For this reason, only two limiting cases will be considered, i.e. a loose interface (no bonding) and a fixed perfectly bonded interface.

1.5 Outline of the thesis

The thesis is organized as follows. In Chapter 2, a microstructural model for lamellar graphite iron (FGI) is introduced to study its response under mechanical and thermo-mechanical loading conditions. To this end, the coupling between the mechanical and thermal fields and the influence of temperature on the mechanical and thermal properties of the microconstituents are incorporated. The complex microstructure of lamellar cast iron is represented by an idealized unit cell model that captures the main morphological features of the material, such as the 3D connectivity and the sharpness of the graphite inclusions.

Next, in Chapter 3, experiments and numerical simulations are used to study the deformation of the graphite inclusions within CGI. The main goal is to investigate the relevance of the graphite mechanical anisotropy for the mechanical behaviour of vermicular cast irons. In-situ micro-tensile tests on CGI samples are carried out in a Scanning Electron Microscope (SEM) and a novel digital image correlation procedure is developed to achieve reliable strain measurements at the scale of the graphite particles (10-50 μm). The second part of the Chapter is dedicated to the development and analyses of 2D CGI microstructural models based on the SEM micrographs. The model is first used to validate the assumption of graphite is mechanical anisotropy by confronting the experimentally measured strains with those estimated from the model. Then, the model is used to evaluate the effect of graphite's anisotropy on the matrix deformation by comparing the results of two models, one in which some

graphite particles are considered as anisotropic and one in which all the particles are modelled as isotropic.

In Chapter 4, an experimental-numerical approach is used to study the mechanical response of pearlitic steels in the temperature range from 20 to 500 °C. A finite strain thermo-viscoplastic model is presented together with a set of elevated temperature tests (tensile and creep tests). The aim of the tests is twofold: first, to provide insight in the elevated temperature mechanical response of the material; and second, to provide the data required to identify the corresponding material parameters. The model is an extension of the model developed by [46] to finite strains. Furthermore, a yield surface is introduced to account for the characteristic yield point found in pearlitic steels and a modified thermal function is proposed based on the experimental observations.

A new microstructural model for elevated temperature mechanical analyses of CGI is introduced in Chapter 5. The point of departure of the model is the cast iron microstructural model discussed in Chapters 1 and 2, where the temperature dependent thermal and mechanical properties of the graphite and matrix are included, as well as the morphology and anisotropy of the graphite inclusions. The time dependency is incorporated via the pearlite matrix through the thermo-viscoplastic model developed in Chapter 4, which is implemented within a FE framework. The microstructural model provides insight into the time dependent response of CGI for temperatures up to 500 °C. Furthermore, the role played by the matrix and graphite in CGI's local and global transient response is also investigated.

Finally, in Chapter 6 the main conclusions are presented. In addition, recommendations for future research in the field of cast iron thermo-mechanical modelling and potential applications are discussed.

Thermo-mechanical analyses of heterogeneous materials with a strongly anisotropic phase: the case of cast iron

Based on

J.C. Pina, V.G. Kouznetsova, M.G.D. Geers,

Thermo-mechanical analyses of heterogeneous materials with a strongly anisotropic phase: the case of cast iron, accepted for publication at the International Journal of Solids and Structures.

2.1 Introduction

Many advanced high performance materials are heterogeneous at a certain scale, with complex microstructures composed of two or more constituents exhibiting different mechanical and physical properties. This microstructural complexity makes the engineering and performance prediction of such materials a challenging task. Furthermore, it requires a good understanding of the microscale phenomena and a proper multi-scale approach to extract the macroscopic material response.

Cast iron is a typical example of such a material, which presents a complex heterogeneous microstructure composed of anisotropic graphite inclusions embedded in a ferrite/pearlite matrix. According to the morphology of the graphite inclusions, cast irons can be classified as: *Flake or Lamellar Graphite Iron (FGI)*, *Compacted or Vermicular Graphite Iron (CGI)* and *Spheroidal, Nodular or Ductile Graphite Iron (SGI)*. The graphite morphology plays a decisive role in the resulting mechanical and physical properties of cast iron [116]. In particular, the complex 3D connectivity of the graphite network found in FGI and CGI, combined with the graphite shape and its local anisotropy are important microstructural factors. For example, nodular cast iron (SGI) contains spherical inclusions dispersed in a metal matrix, which results in a relatively high strength and ductility, but its thermal conductivity is close to that of steels. On the contrary, lamellar cast iron (FGI) contains graphite inclusions in the form of lamellas or flakes that form a 3D interconnected network. An example of the lamellar cast iron microstructure is shown in Figure 2.1.a. Although the sharp graphite edges act as local stress concentrators, leading to an overall strength decrease, the 3D interconnected network of graphite results in a material with a high thermal conductivity and a relatively low thermal expansion coefficient. In be-

tween nodular and lamellar cast iron is compacted cast iron (CGI). In CGI, the 3D interconnected graphite network is also present, however the flake type inclusions are replaced by vermicular worm shaped ones leading to a coral like morphology. This type of microstructure results in mechanical and physical properties that are intermediate between FGI and SGI [68, 125, 144]. This makes lamellar and compacted cast irons a popular option for heavy-duty thermo-mechanical applications (e.g. truck engines).

The complex microstructure of cast irons makes the estimation of their effective properties a challenging task. In the literature several papers can be found in which analytical models are used to predict the elastic [16, 33, 41, 43, 50] and thermal properties [63, 67] of cast irons. The different approaches considered range from simple Reuss and Voigt bounds, to the more advanced Hashin-Shtrikman bounds and self-consistent methods. In general, in these (semi)-analytical methods, cast irons are considered as two phase materials composed of isotropic or anisotropic graphite inclusions embedded in an isotropic metal matrix, in which the influence of the shape of the particle is taken into account through the particle aspect ratio. The main drawbacks of the (semi)-analytical methods is that no interaction between individual particles is considered and a perfect adhesion between graphite particles and metal matrix has to be assumed. The lack of interaction between particles is not a problem in nodular cast iron, where the graphite inclusions are nearly isolated nodules, but this does not hold for lamellar and compacted cast irons where the graphite inclusions form a 3D interconnected network.

In the particular case of nodular cast iron, several finite element unit cell models have been introduced in the literature to study the mechanical response of the material within elastic and elasto-plastic regimes [17, 31, 41, 82]. However, to the best of our knowledge this approach has not been used to study lamellar and compacted cast irons. For the analysis of the isothermal mechanical response of compacted cast iron a direct discretization of 2D micrographs [47, 97] or a model of slender ellipsoids [50] has been used. These approaches do not include the 3D interconnectivity and are therefore not applicable to transport properties and coupled effects. Recently, Velichko *et al.* [144] have used FIB-tomography images in a FEM analysis to obtain the overall thermal and electrical conductivity of lamellar cast iron. Although the tomography based model is a geometrically exact representation of a small part of the microstructure, it becomes prohibitively computational expensive if anisotropic and/or non-linear material properties are to be included.

In this work, a microstructural model for lamellar cast iron is introduced to study the response of the material under mechanical and thermo-mechanical loading conditions. To this end, the coupling between the mechanical and thermal fields and the influence of temperature on the mechanical and thermal properties of the microconstituents are incorporated. The complex microstructure of lamellar cast iron, is represented here by an idealized unit cell model that captures the main morphological features of the material, such as the sharpness and the 3D connectivity of the graphite inclusions. This simplified representation of the microstructure makes it possible to investigate the influence of different microstructural features (i.e. matrix/graphite interface, graphite anisotropy, matrix nonlinear material behaviour, etc.) and complex mechanical and thermo-mechanical loads on the local and macro-

scopic response of the material.

The main innovative and original contributions of this chapter can be summarized as:

- a systematic methodology for the thermo-mechanical analysis of heterogeneous materials with anisotropic constituents based on a multi-scale computational homogenization approach;
- multi-scale analysis of the influence of the different microstructural parameters on the local and overall response of lamellar cast iron;
- an approach, enabling the incorporation of mechanical and thermal nonlinearities of the properties of the microconstituents and the interface in the model;
- the unit cell model for lamellar cast iron, which in a simplified manner accounts for the main morphological features of the material.

Even though this chapter focuses on lamellar cast iron as a case study, the methodology and results presented are applicable to a broader class of heterogeneous materials with complex 3D interconnected microstructures composed of anisotropic constituents under thermo-mechanical loads.

This chapter is composed of five parts. In Section 2.2 the microstructural model is introduced. The mechanical analysis is presented in Section 2.3. Here, the influence of graphite anisotropy and the interface condition is evaluated. Then, in Section 2.4, the thermo-mechanical analysis is discussed, in which a uniform temperature distribution over the microstructural unit cell is considered. The influence of graphite anisotropy on the material thermal expansion is studied. In addition, different thermal loads are investigated to assess their influence on the local and overall response. In Section 2.5 the model is extended to a fully coupled thermo-mechanical analysis. First, in Section 2.5.1 the model for heat transfer analysis is presented. Then, in Section 2.5.2 the fully coupled thermo-mechanical analysis is discussed. Finally, in Section 3.4 the main conclusions are summarized.

2.2 Microstructural model

2.2.1 Geometry

Among the different methods for solving the governing equations in a direct 3D microstructural analysis, the finite element method (FEM) is used here since it is well suited for complex geometries and non-linear material behaviour. To create a 3D FE model of the microstructure, in general two approaches can be followed. In the first approach, the material microstructure can be obtained experimentally from tomography analyses and exported to FEM [144]. A geometrically precise description of the microstructure can be obtained in this way. However, because of the large number of voxels required to provide a good representation of the microstructure, the problem becomes computationally very expensive. Moreover the use of advanced material (e.g. anisotropy, non-linear mechanical and thermal properties) or interface

models to describe the behaviour of the micro-constituents can significantly increase the computational cost of the many degree-of-freedom model [144]. The second approach is to build a more compact 3D FE model based on an idealized geometry that is sufficiently representative of the actual material microstructure. This model needs to include all relevant features of the material microstructure that may have a significant impact on the overall response. In spite of the fact that the geometrical representation of the microstructure no longer exactly resembles that of the real material, the underlying complex material response of the micro-constituents still apply. This enables a feasible analysis of certain complex mechanisms, like the combination of the plastic deformation, temperature dependent material properties, thermal cycling and residual stresses, which is otherwise not at reach with a fully detailed 3D model. This second approach is therefore adopted here.

Departing from the concept of local periodicity, that is by now well established in computational homogenization [45], a unit cell is introduced in Figure 2.1.b, which is a representation of the idealized material microstructure. Despite its geometrical simplicity, this unit cell preserves two essential features of lamellar cast iron. Firstly, the interconnected graphite network is incorporated, as clearly illustrated by the 3x3x3 periodic stacking of the unit cells in Figure 2.1.c. Secondly, the sharp edges of the lamellas are also present making it possible to evaluate their influence on, for example, damage initiation and propagation at the microlevel. Although the random orientation of the graphite lamellas is not included in this unit cell (since the lamellas only span in orthogonal directions), arbitrary 2D cross-sections of the 3D model (Figure 2.1.d) exhibit more geometrical diversity than one would expect, and qualitatively resembling 2D images of the real microstructure (Figure 2.1.a).

The volume fraction of graphite in this unit cell is 12%. Assuming the matrix material consists of 50% pearlite and 50% ferrite, this corresponds to approximately 4.14% weight percent of carbon, which is within a typical range for lamellar cast irons.

The graphite hexagonal crystalline structure (Figure 2.2.a) has an important effect on the cast iron behavior. Graphite particles have a layered structure with strong covalent bonds within the basal planes (so-called *a-direction*) and weak van der Waals bonds between the basal planes (*c-direction*) [35, 44]. This layered structure results in a pronounced anisotropy of graphite's mechanical and physical properties. The graphite basal planes in lamellar cast iron are typically oriented parallel to the graphite flakes [122]. Hence, the graphite lamellas in the unit cell will be modelled as a transversely isotropic material as illustrated in Figure 2.2.b. For each of the three perpendicular graphite planes, the isotropic behaviour holds in the corresponding graphite plane (graphite XY, graphite YZ or graphite ZX from Figure 2.2.b), and the anisotropic out-of-plane behaviour applies to the directions perpendicular to this plane.

2.2.2 Material properties

The metal matrix of cast iron usually consists of a pearlite/ferrite mixture. Since the present study focuses on the effects of the graphite interconnectivity and anisotropy on the behavior of the lamellar cast iron, the physical difference between these

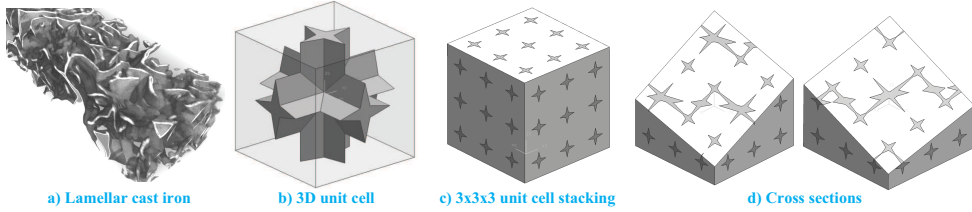


Figure 2.1: Lamellar cast iron unit cell: a) Lamellar cast iron microstructure, b) 3D unit cell, c) 3x3x3 periodic unit cell stacking, d) 3x3x3 periodic unit cell model cross sections, dark-graphite, light-steel matrix.

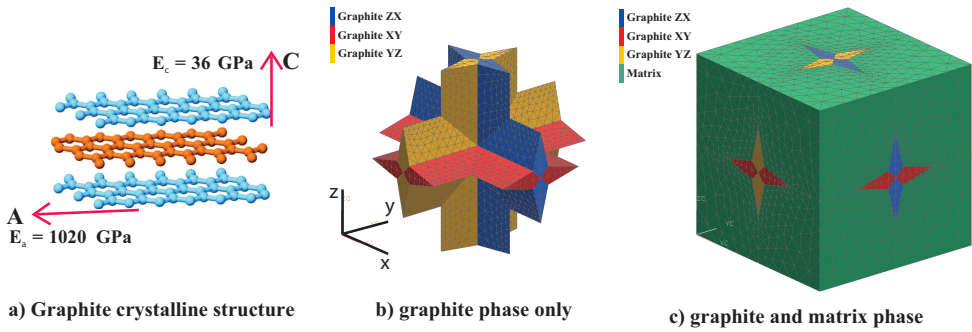


Figure 2.2: Lamellar cast iron 3D unit cell showing the finite element discretization and the graphite orientations: a) graphite crystalline structure, b) graphite lamellas, each colour represents the orientation of graphite's transversal plane of isotropy with respect to the global coordinate system, c) full unit cell including the matrix.

matrix phases will not be resolved explicitly. The matrix will be considered as a homogeneous isotropic elasto-plastic material, composed of 50% pearlite and 50% ferrite. The Young's modulus of the matrix as a function of temperature is based on the data of Bonora and Ruggiero [17], see Figure 2.3.a. The Poisson's ratio has been assumed temperature independent and equal to 0.29 [32, 48]. The matrix flow stress evolution as a function of the plastic strain is based on the work by Allain and Bouaziz [5]. This physically based model predicts the flow stress of a pearlitic/ferritic mixture by evaluating the contribution of each phase. The resulting flow stress at different temperatures used in the simulation is shown in Figure 2.3.b.

As mentioned before, graphite is modelled as a transversely isotropic material. In the present work, the values of the graphite elastic constants estimated by Blakslee *et al.* [15], given in Table 3.3, are used. A large degree of anisotropy can be noticed, with the in-plane elasticity modulus almost five times exceeding that of the matrix, while the out-of-plane modulus is almost five times lower than that of the matrix. The elastic properties of the graphite have been assumed temperature independent in the considered range of temperatures.

In order to assess the impact of the graphite anisotropy on the local and overall

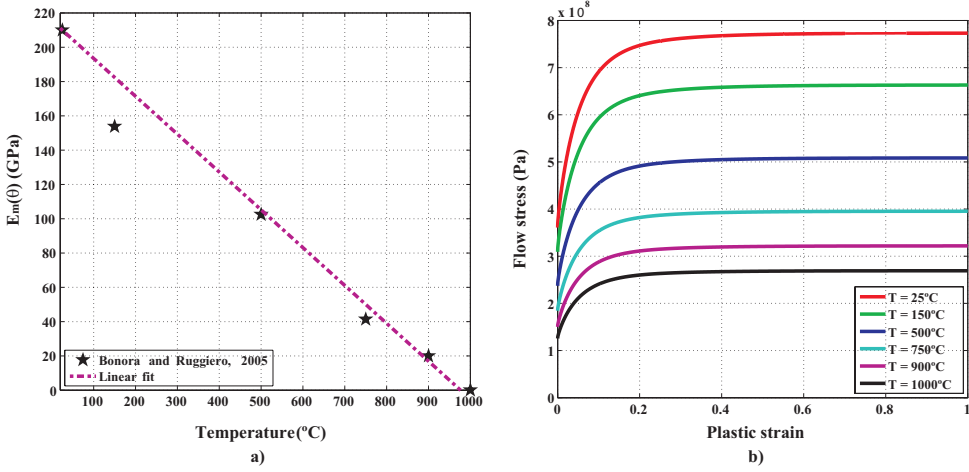


Figure 2.3: Mechanical properties of the pearlite-ferrite matrix as a function of temperature: a) Young's modulus [17]; b) flow stress.

Table 2.1: Graphite elastic constants: in-plane (directions 1 & 2) and out-of-plane (direction 3) Young's moduli, Poisson's ratios and shear moduli [15].

$E_{11} = E_{22}$ [GPa]	E_{33} [GPa]	$G_{23} = G_{31}$ [GPa]	ν_{12}	$\nu_{23} = \nu_{31}$
1020.4	36.364	0.280	0.163	0.012

response, the behavior of a unit cell with the anisotropic graphite will be compared to the response of a geometrically identical unit cell in which the graphite would be isotropic. In the first isotropic graphite model, average values between the in-plane and out-of-plane mechanical properties are considered, i.e. $E_{11} = E_{22} = E_{33} = 528$ GPa and $\nu_{12} = \nu_{23} = \nu_{31} = 0.0875$. In addition, two other isotropic graphite models will be studied, i.e. with the elastic modulus and Poisson's ratio taken equal to either graphite's in-plane or out-of-plane elastic constants respectively (see Table 3.3 for the values). These two models will provide, respectively, upper and lower bounds for the unit cell overall mechanical response.

The thermal properties of the graphite and matrix are presented in Figures 2.4 and 2.5. In Figure 2.4, the thermal expansion coefficients (CTE) of the matrix and graphite are shown. The matrix CTE values are in between the in-plane and out-of-plane CTEs of the graphite, with the latter being very small or even negative. In Figure 2.5, the thermal conductivities of the different phases (pearlite, ferrite and graphite), used in the simulations, are presented. The thermal conductivities of the matrix constituents (pearlite and ferrite) and the graphite, given in the literature

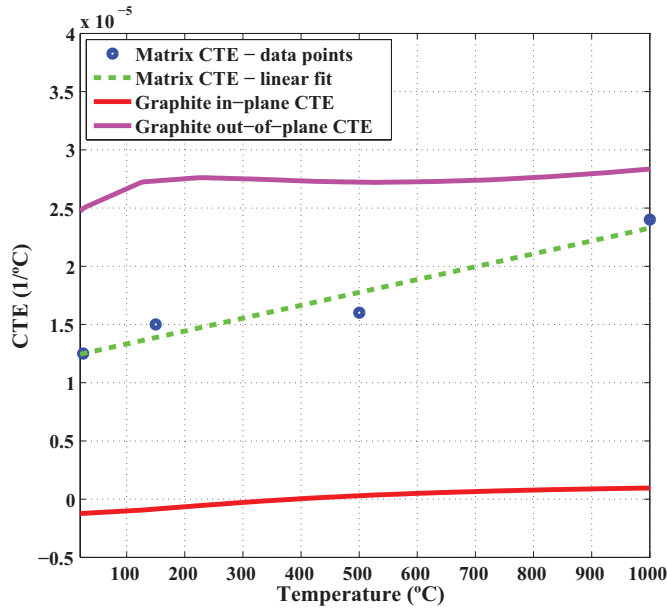


Figure 2.4: Thermal expansion coefficients (CTE) of the phases: matrix CTE from Bonora and Ruggiero [17]; graphite CTE from Morgan [98].

[67], differ an order of magnitude. Here the values of the thermal conductivities of the matrix mixture is chosen such to provide a good approximation of its overall thermal conductivity. Again, a big difference can be seen between the in-plane and out-of-plane properties of the graphite. In this case, the in-plane thermal conductivity of the graphite is one order of magnitude higher than the out-of-plane value and that of the matrix. The density and the heat capacity values [67] of the graphite and the matrix are presented in Table 2.2.

Table 2.2: Graphite and matrix density and heat capacity [67].

	Density [kg/m^3]	Heat capacity [$\text{J}/(\text{kg} \text{ } ^\circ\text{C})$]
Graphite	2250.00	707.68
Matrix	7820.00	477.00

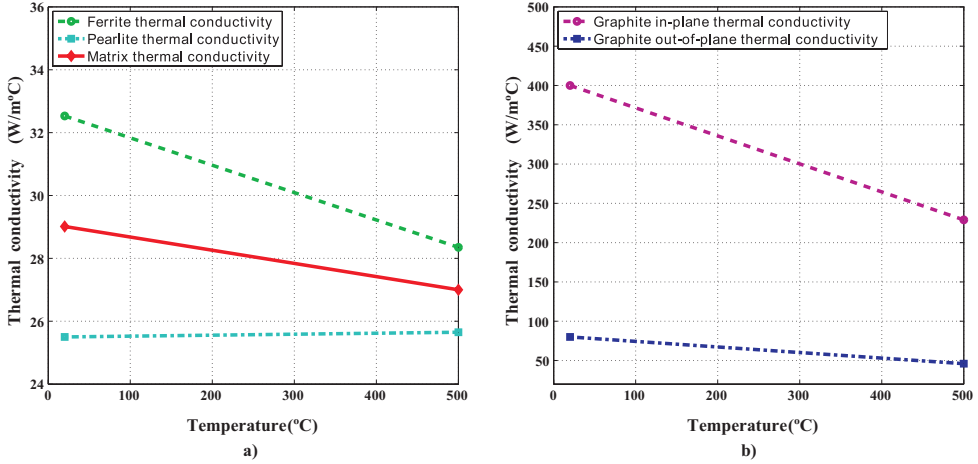


Figure 2.5: Thermal conductivity of the phases [67]: a) matrix thermal conductivity; b) graphite thermal conductivity.

2.3 Isothermal mechanical analyses

The lamellar graphite unit cell model defined in the previous section, will be exploited here to study the effect of graphite's anisotropy and the interface conditions on the mechanical response at both the micro and macro scales. The periodic boundary conditions, as summarized in Appendix C, have been applied to the unit cell. The overall unit cell deformation of 0.5% in the z-direction has been prescribed in such a way, that the homogenized stress state remains uniaxial (see Appendix C). In the next section, the graphite/matrix interface will be considered fixed. In Section 2.3.2, the effect of this interface condition will be studied in more detail.

2.3.1 Effect of graphite anisotropy

To study the effect of the anisotropy of the graphite, on the global and local material response, the unit cell response with the transversely isotropic graphite model and the isotropic graphite models are compared. The material constants used were detailed in Section 2.2.2.

The homogenized macroscopic stress-strain response for the four different models is presented in Figure 2.6. The anisotropic graphite model and the isotropic model with the average values of graphite elastic constants are now compared. Both models show a similar response in the elastic and plastic regimes. However, prior to macroscopic yielding the isotropic graphite model exhibits a stiffer response than the anisotropic graphite model whereas after yielding this trend is reversed. This behaviour results from the local response of the unit cells presented in Figure 2.7, where the local von Mises stresses in the matrix and the graphite are plotted. Note that the stresses in the matrix are one order of magnitude lower than the stresses in the graphite. Therefore, variations in the graphite stresses have a significant impact

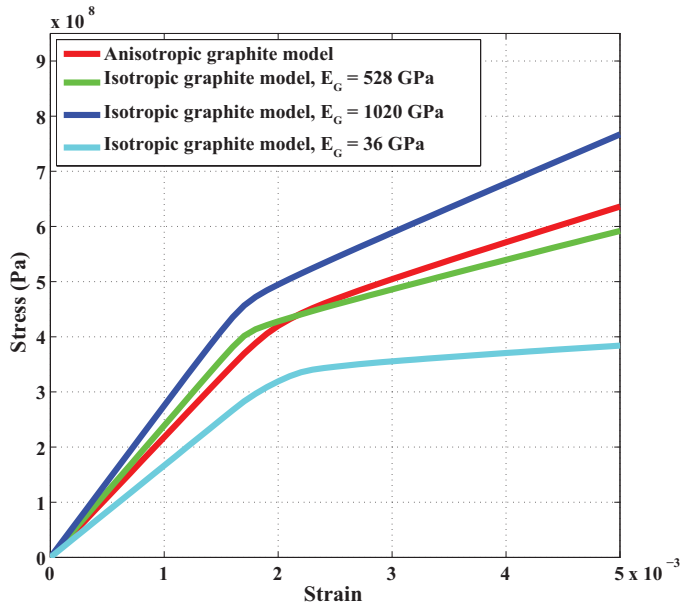


Figure 2.6: Homogenized macroscopic stress-strain response of the unit cells with the anisotropic graphite model and the three isotropic graphite models.

on the macroscopic response. Prior to macroscopic yielding (Figure 2.7.a), higher stresses are observed in the unit cell with the isotropic graphite model, both in the matrix and the graphite. On the other hand, at the end of the macroscopic loading (Figure 2.7.b), despite the higher local stresses in the matrix in the isotropic graphite model, a higher macroscopic stress results for the anisotropic graphite unit cell, through the higher local stresses in the graphite phase.

The graphite anisotropy has a clear impact on the matrix local response, leading to two distinctly different stress distributions for the unit cells with either isotropic or anisotropic graphite. The stresses in Figure 2.7 reveal that graphite anisotropy initially triggers a larger plastification area of the matrix (Figure 2.7.a right), subsequently evolving to an area of high stresses surrounding the entire graphite/matrix interface (Figure 2.7.b right). On the other hand, when graphite is taken isotropic, the higher stresses are localized at the tip of the lamellas (Figures 2.7.a and 2.7.b left). Moreover, the isotropic model shows a zone of high stresses extending far away from the graphite tips, which is not present in the anisotropic model. If these two models are to be used for the study of microscale damage mechanisms, the response would be entirely different. This emphasizes the importance of incorporating graphite anisotropy into the modelling of cast iron. More generally, the anisotropy of microconstituents in high contrast multi-phase and composite materials, is a key factor for the investigation of microscale phenomena.

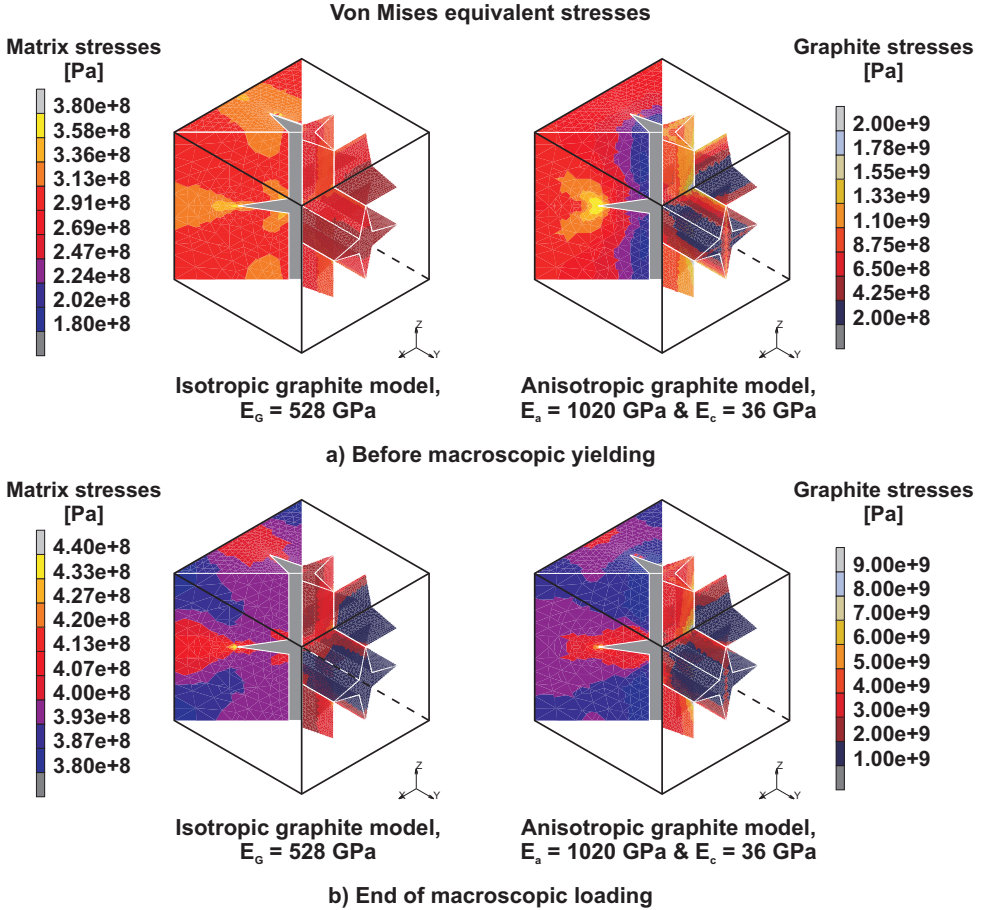


Figure 2.7: Local equivalent von Mises stresses in the matrix and the graphite: a) before macroscopic yielding, macroscopic strain equal to 0.15 %; b) end of macroscopic loading, macroscopic strain equal to 0.50 %. Left isotropic graphite model and right graphite model, vertical loading direction.

2.3.2 Effect of interface condition

In heterogeneous materials, the properties of the interface between different micro-constituents play a key role in defining the local and overall responses.

For this reason, a microscale interface model is often included in the study of micro- and macro-scale phenomena. One way to model the behaviour of interfaces is through so-called cohesive zone models [143,150]. However, for a correct description of the interface behaviour accurate data on the interface strength and dissipated energy under different loading modes is required. Although for some interfaces this information can be obtained experimentally [79,143], it turns out to be a difficult task in most other cases. Lamellar cast iron is such a case, where due to the complex 3D microstructure the characterization of the interface is not straightforward.

Due to the lack of quantitative data on the matrix-graphite interface behaviour, the two limiting cases are therefore considered instead, i.e. a loose interface and a fixed interface. In spite of their simplicity, these limiting cases provide lower and upper bounds, for the response of a material with a more complex interface behaviour. To model the loose interface, the matrix and the graphite are defined as two separate contact bodies, without friction.

The unit cell with anisotropic graphite, as developed before, is used. Two load cases are considered: *i*) uniaxial tension and *ii*) uniaxial compression. In both cases an axial strain up to 0.5% is prescribed in the z-direction according to the procedure summarized in Appendix C.

The homogenized macroscopic stress-strain response for the two interface conditions and the two loading cases are presented in Figure 2.8. Obviously, when the interface is fixed, the response in tension and compression is nearly identical. On the other hand, the loose interface model yields different results in either tension or compression.

The differences observed in the macroscopic response again emerge from the microstructural behaviour. The local equivalent von Mises stresses for the matrix and graphite phases are shown in Figure 2.9. The load cases yielding a similar macroscopic behaviour (i.e. fixed interface tension and compression and loose interface compression) also show similar equivalent stresses distributions in both the matrix and graphite. A noticeably different situation is observed for the tensile load case with loose interface. When the tensile load is applied the matrix/graphite interface opens. The interfacial opening accommodates a part of the applied macroscopic strain, thus leading to, on average, lower stresses in both the graphite and the matrix. This results in a weaker macroscopic response, see Figure 2.8. At the same time, the interface opening around sharp lamella edges leads to local stress concentrations in the matrix that are more pronounced than in the fixed interface models.

These results emphasize the critical roll of the interface mechanics in cast irons, which typically exhibit a noticeable difference between tension and compression [1, 118].

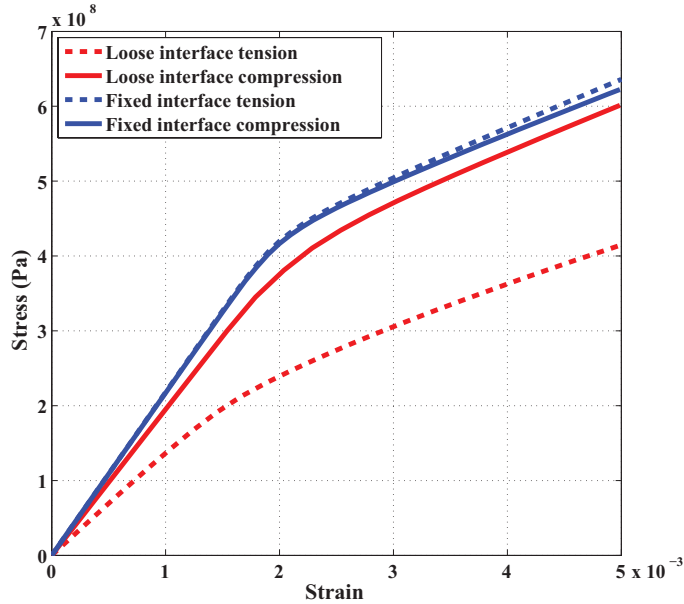


Figure 2.8: Influence of the interface condition on the homogenized strain-stress response of the unit cells with different interface conditions under uniaxial tension and compression.

2.4 Thermo-mechanical analyses: uniform temperature distribution

In the previous section, the influence of the mechanical properties of the micro-constituents on the overall local and macroscopic response under applied mechanical load was discussed. In this section, the response of the microstructural unit cell model described in Section 2.2 under uniform thermal loading is investigated. The aim of this study is to analyze the influence of the mismatch in mechanical and thermal properties of the microstructural phases on the macroscopic thermo-mechanical response.

Cast irons, in particular lamellar and compacted types, are often used in applications subjected to cyclic thermal loads, where a high thermal conductivity and a low thermal expansion are essential. So far only a few examples of microstructural simulations of these phenomena in cast iron have been presented in the literature [17, 144]. However, for metal matrix composites (MMC) a vast amount of models, mostly analytical, have been developed for the prediction of the overall coefficient of thermal expansion (CTE) and other effects, e.g. the influence of residual stresses [7, 9, 34, 37, 102, 115, 117, 123, 124, 138].

For a composite material with a given phase volume fraction, several microstructural characteristics contribute to the observed overall thermal expansion. One of the most important features is the interconnectivity of the phases, i.e. if at least one of the phases forms a continuous 3D network. Another important characteristic is the

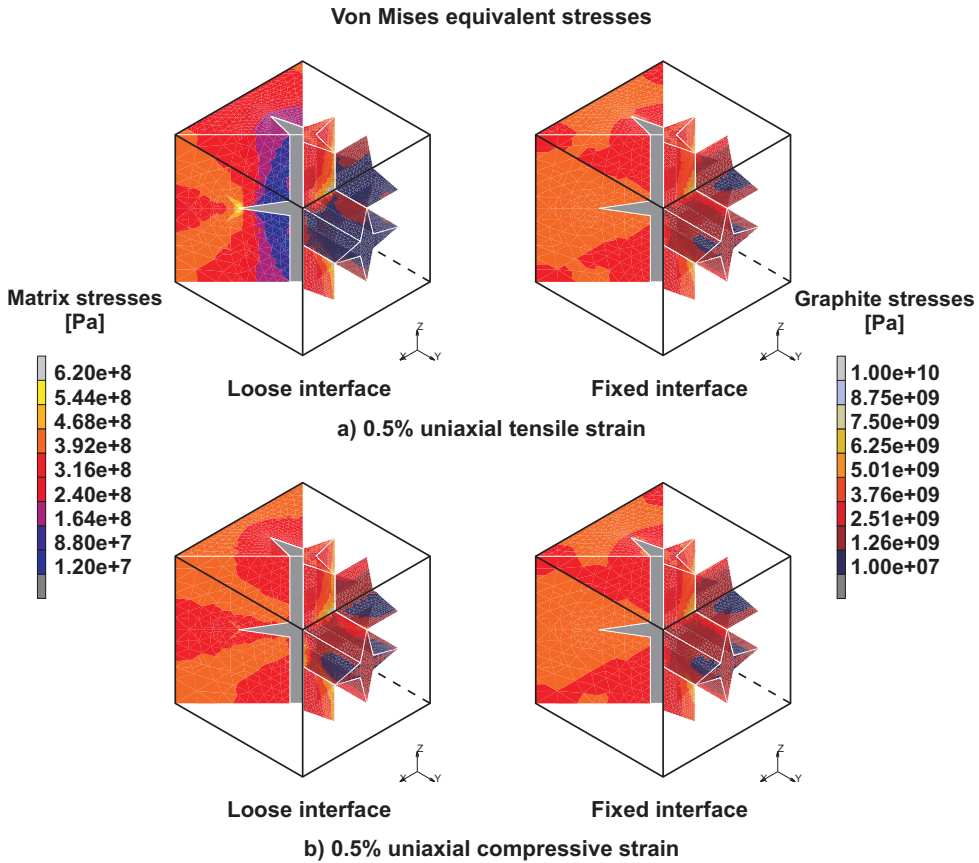


Figure 2.9: Local equivalent von Mises stresses in the matrix and in graphite: a) 0.5% uniaxial tensile strain; b) 0.5% uniaxial compressive strain both in the vertical direction. Left: model with loose interface condition; right: model with fixed interface condition.

mismatch in elastic and CTE constants of the phases, which can also depend on the temperature and direction (anisotropy). The residual stresses, e.g. resulting from the processing, may also have a substantial contribution. Even though the precise local geometrical details of the phases are usually not important for the overall CTE of the composite, they do define the extent of plastic deformation and damage, which may accumulate with thermal cycling, thus defining the lifetime.

In the following sections, all these aspects will be studied in detail through the analysis of the proposed lamellar cast iron microstructural unit cell.

2.4.1 Effect of graphite anisotropy

First, the effect of the graphite anisotropy on the overall CTE and the corresponding microscale phenomena is evaluated. To this purpose, the response of the microstruc-

tural unit cell incorporating the elastic and CTE anisotropy of the graphite is confronted to the response of the unit cell, with isotropic elastic and CTE constants for the graphite. In both cases, the matrix is modeled as isotropic elasto-plastic with temperature dependent properties. The interface is considered fixed, the influence of the interface condition will be studied in a subsequent section. The unit cells have been subjected to a uniform temperature increase from 20 °C to 500 °C, allowing an overall free expansion. The homogenized CTE is computed as the instantaneous ratio between the resulting overall strain and temperature increment. Note, that due to the particular geometrical arrangement of the graphite inclusion, the expansion of the unit cell is the same in the three principal directions, even when anisotropy of graphite is included.

The overall CTEs computed using the two unit cell models are shown in Figure 2.10. For comparison, analytical estimates given by the rule of mixtures (ROM) and Turner’s model, providing, respectively, the upper and lower bounds for the CTE of a composite consisting of two isotropic linear elastic phases [9, 37, 72, 123], are also shown. The expressions for these analytical estimates are given in Appendix D. The observed non-linearity of the overall CTE as a function of temperature is the result of the temperature dependent mismatch between the phases.

Figure 2.10 shows that the results obtained with the unit cell with the isotropic graphite almost coincide with the prediction of Turner’s model. Indeed, Turner’s model is known to be a good estimate for composites with a 3D interconnected microstructure, where one phase constrains the dilatation of the other phase and where the stress state in both components is nearly hydrostatic. This situation is also present here, where the low thermal expansion of the graphite constraints the dilatation of the matrix leading to a predominant hydrostatic stress state. Furthermore, to accommodate the high strain mismatch between the two phases, the matrix needs to deform plastically next to the graphite/matrix interface. That is why, the extent of plastic deformation is restricted to the regions surrounding graphite lamellas, with a very limited amount of plastic deformation concentrated near the graphite lamella tips (Figures 2.11.b).

More importantly, Figure 2.10 reveals that when the microstructural constituents are anisotropic, the analytical estimates fail. The overall CTE computed from the unit cell with anisotropic graphite is significantly lower than in all isotropic estimates. Moreover, it exhibits a noticeably non-linear dependence on the temperature, which is a result of the temperature dependent mismatch of the elastic properties of the phases.

The distribution of the microscale fields is shown in Figures 2.11.c and d. Due to the anisotropy of graphite, the phase mismatch in CTE and elastic constants is large, and opposite for the graphite in-plane and out-of-plane directions, see Section 2.2.2. A large strain mismatch needs to be accommodated around the matrix-graphite interface, leading to high deviatoric stresses, see Figure 2.11.c. Larger areas of plastic deformation results compared to the unit cell with isotropic graphite, see Figure 2.11.d. These phenomena may play a decisive role in the initiation and evolution of microstructural damage leading to fracture.

The major conclusion that can be drawn from this analysis is that although the theoretical models provide adequate predictions for the thermal expansion of materials

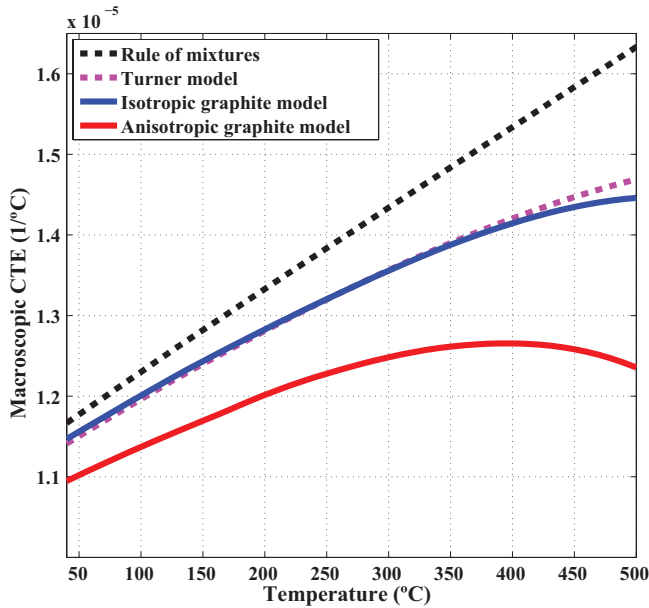


Figure 2.10: Macroscopic CTE for the lamellar cast iron unit cells with isotropic and anisotropic graphite, compared to the rule of mixtures and Turner model estimates.

with isotropic phases, they yield inaccurate estimates when high contrast anisotropy (in mechanical and/or thermal properties) is present in at least one of the phases. A microstructure-based modelling approach provides a tool to determine correct CTE values.

2.4.2 Effect of interface condition

In this section the role of the interface condition (fixed or loose) on the CTE is investigated. The results from the previous section are compared with the equivalent models, using a loose frictionless interface. Since the expansion due to the temperature change is free no separation between the two phases takes place even when a loose interface condition is used. However, relative sliding of the two phases is possible.

The computed macroscopic CTEs of the unit cells with the isotropic and anisotropic graphite and with fixed and loose interface are compared in Figure 2.12. The CTEs obtained with the loose interface conditions are slightly higher than the ones obtained with the fixed interface conditions. The large in-plane CTE mismatch between the matrix and the graphite, in both the isotropic and anisotropic graphite models, together with graphite's 3D interconnected network implies that graphite strongly constraints the matrix thermal expansion. It therefore dominates the macroscopic thermal expansion of the material. A fixed interface condition between the two phases adds an additional constraint. Now the matrix thermal expansion is not only

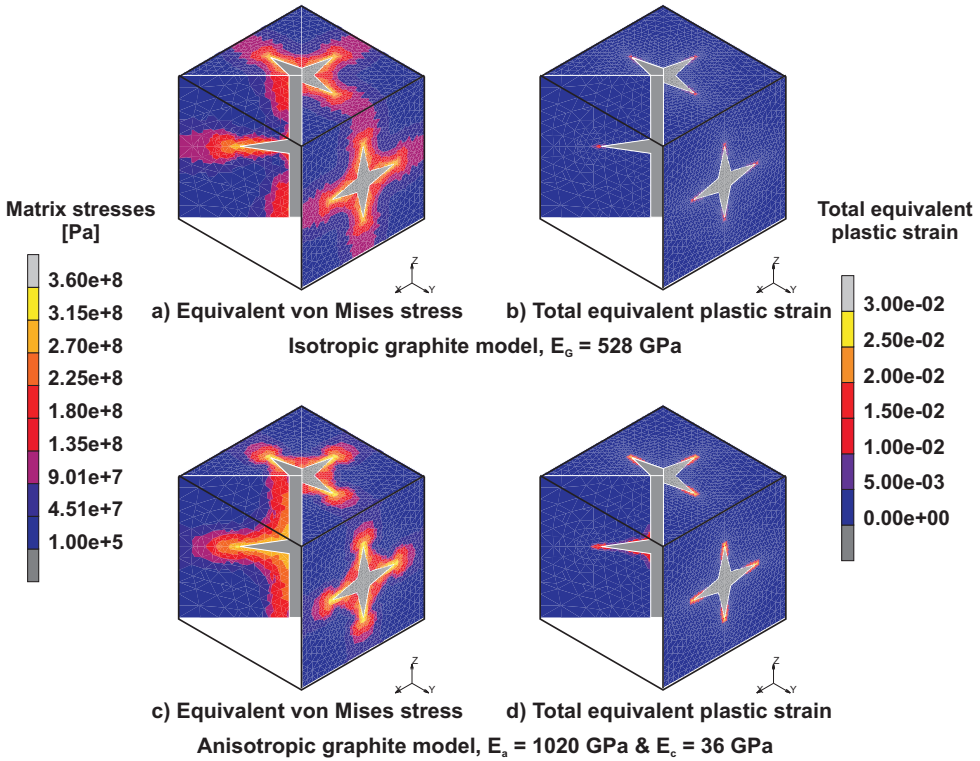


Figure 2.11: Local equivalent von Mises stresses (left) and total equivalent plastic strain (right) in the matrix at 500 °C. Top: isotropic graphite model; and bottom: anisotropic graphite model.

controlled by the 3D graphite network, but the relative interface sliding of the two phases is also inhibited, making the constraint imposed by the graphite even more effective. Moreover, as shown in Figure 2.13, this triggers differences in terms of stresses and strains between the models with fixed and loose interface conditions. In the unit cell models with fixed interface, the strain mismatch between the matrix and the graphite is accommodated locally by the elastic and/or plastic deformation of the two phases near the interface (Figures 2.13b and d). For the loose frictionless interface, the strain mismatch is mostly accommodated by the relative sliding of the two phases leading to lower stresses at the interface (Figures 2.13a and c).

From Figures 2.12 and 2.13 it can be concluded that although the interface condition has a limited influence on the macroscopic CTE, it has a major impact on the local stresses and strains to accommodate the local mismatches.

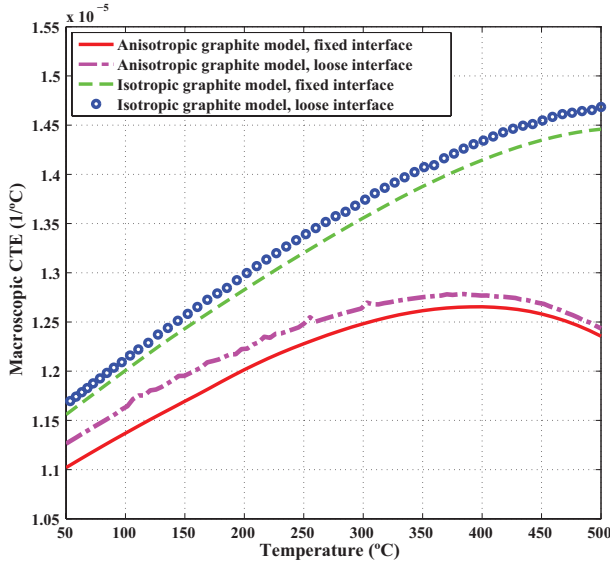


Figure 2.12: Macroscopic CTE obtained from the unit cell models with isotropic and anisotropic graphite, considering fixed and loose graphite/matrix interfaces.

2.4.3 Effect of processing history

The CTE and elastic mismatch of the phases not only affects the overall thermal expansion behaviour but can also lead to internal residual stresses, when the material is cooled down from a processing temperature to room temperature. These stresses can give rise to local plastic deformation of the matrix that will influence the response of the material upon subsequent thermal and mechanical cycles. These effects have been previously studied in the literature in the context of metal matrix composites [7,100,102,124]. To our knowledge, the case of cast iron has not been studied before. In cast irons, after solidification is completed, the temperature below which no further microstructural changes are expected to take place upon further cooling is estimated to be 723 °C, the eutectoid temperature. Assuming this temperature corresponds to the stress free state as an upper bound, the effect of residual stresses on the overall CTE is evaluated by first simulating a cool down step from 723 °C to 20 °C and then increasing the temperature to 500 °C, an operational temperature. The local and overall response of the material is compared with its equivalent behaviour without any thermal history, see Figure 2.14. Figure 2.14.a shows that the overall CTE of the composite is considerably increased when the thermal history is included. Once the material cools down from the stress free temperature 723 °C, the plastic deformations start to develop already for a temperature drop of 100 °C due to the local CTE mismatch. Upon reaching room temperature, high residual stresses are present, shown in Figure 2.14.b. These residual stresses will lead to a higher

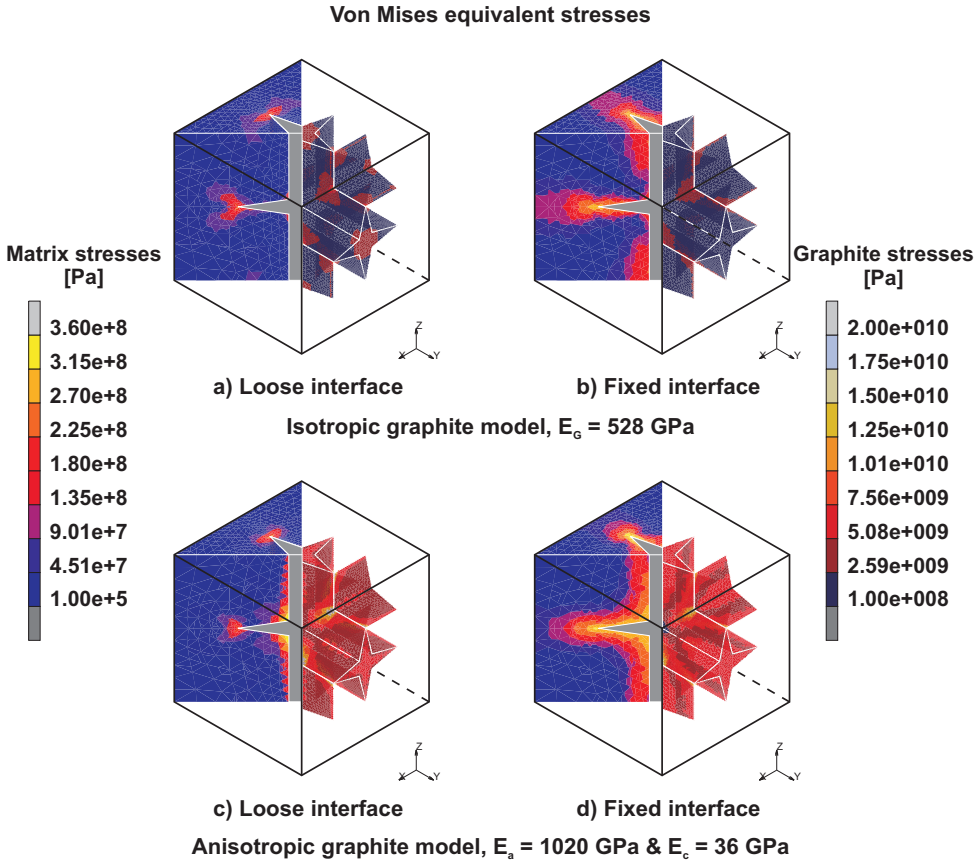


Figure 2.13: Local equivalent von Mises stresses in the matrix and in the graphite for the unit cell models with isotropic (top) and anisotropic graphite (bottom) after a temperature change from 20 °C to 500 °C. Left models with the loose frictionless interface condition and right models with the fixed interface condition.

overall CTE (Figure 2.14.a) and a higher local stress in the matrix (Figure 2.15) during subsequent operating conditions.

2.4.4 Effect of thermal cycling

When a heterogeneous material is subjected to a repeated temperature change, the thermal expansion and elastic mismatch between the phases produces a strain mismatch that has to be accommodated by the elastic and, possibly, plastic deformation of the phases. The extent of the presence of plastic deformation and depends on different factors, like CTE and elastic mismatch, yield strength and hardening behaviour of the ductile phase, volume fraction of the brittle phase and magnitude of the temperature change [102, 130]. For a fixed volume fraction and temperature

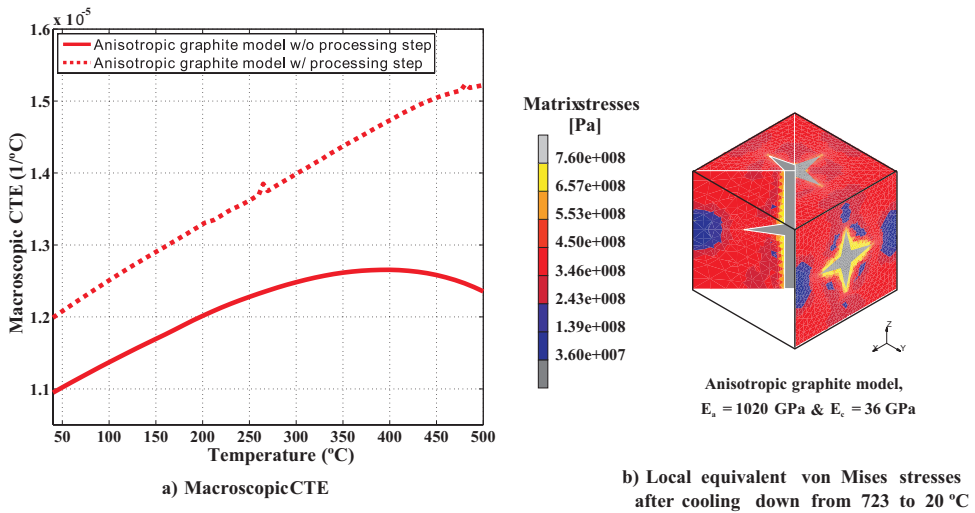


Figure 2.14: Macroscopic CTE (a) and local response (b) of the unit model with anisotropic graphite, with and without thermal processing step.

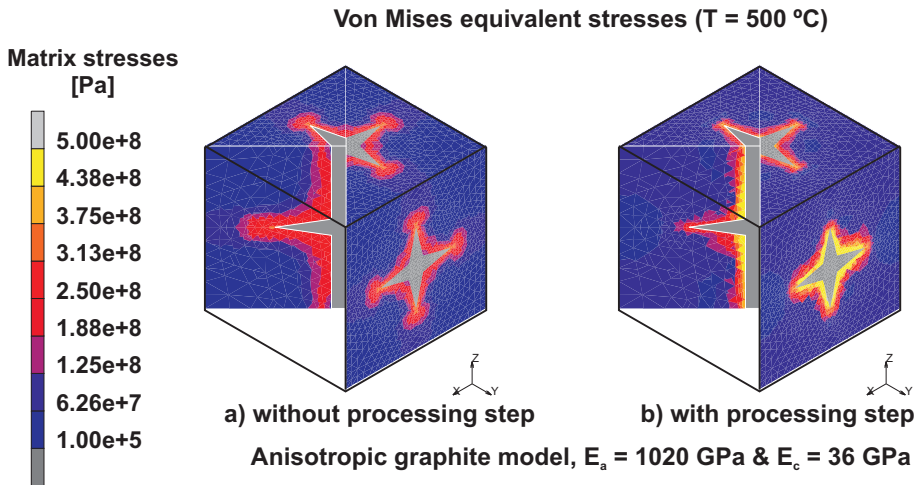


Figure 2.15: Local equivalent von Mises stresses in the matrix for the unit cell models with anisotropic graphite after a temperature change from 20 °C to 500 °C: a) without prior thermal processing step, b) with prior thermal processing step.

change, the cyclic plastic strain accumulation is mainly controlled by the strain mismatch, yield strength and hardening behaviour of the ductile phase.

In a temperature dependent elasto-plastic material with hardening, the current flow stress depends on the previous deformation history and on the temperature. With every temperature reversal the yield surface expands. After a certain number of cycles the size of the yield surface will become large enough to prevent no further plastic deformation. The number of cycles at which the plastic strain saturation is reached and its level depends on the hardening behaviour of the matrix and the internal strain mismatch. The strain mismatch determines the magnitude of the internal stresses that constitutes the driving force for the plastic strain accumulation.

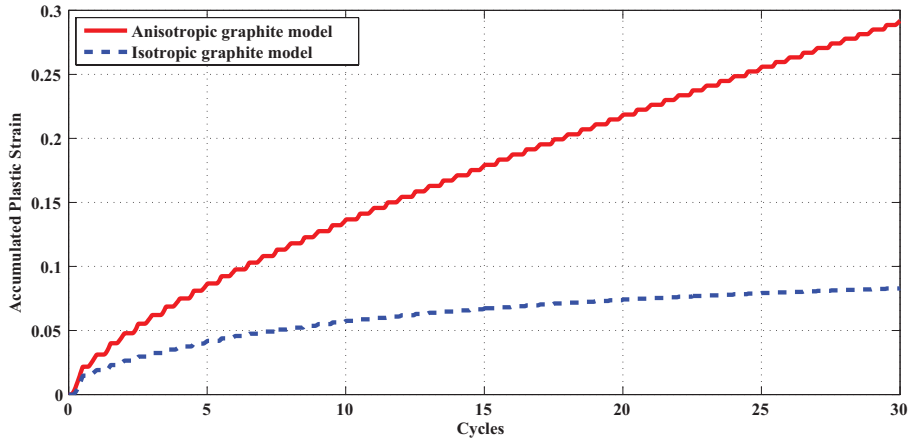
To numerically evaluate the effect of the strain mismatch and ductile phase hardening on the local elasto-plastic response of the matrix during thermal cycling, the influence of the strain mismatch and matrix hardening behaviour is next studied. First, the influence of the strain mismatch is evaluated by comparing the response of the anisotropic and isotropic graphite unit cell models. As discussed in Section 2.4.1, the anisotropic graphite unit cell model has a higher strain mismatch than the isotropic graphite model, for the same matrix yield strength and hardening. Both models were subjected to 30 thermal cycles (20 °C - 500 °C - 20 °C) and allowed to expand freely in all directions. The plastic strain accumulation is quantified in a point of the matrix located near the inner corner of the graphite (see Figure 2.1). The results are shown in Figure 2.16.a.

After 30 cycles, the isotropic graphite unit cell model is asymptotically saturating. The anisotropic graphite model, on the other hand, with a higher strain mismatch, still shows a continuous and steady increase of the accumulated plastic strain.

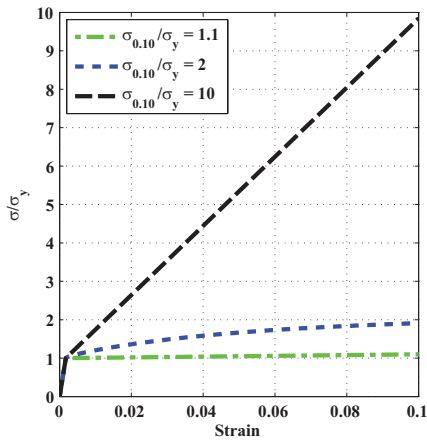
The influence of the matrix hardening is next assessed. To this aim, the isotropic graphite model is considered to focus on the effect of the matrix hardening only. Three cases are compared: low hardening, high hardening and medium hardening. The first two cases are modelled by linear hardening controlled by the ratio between the stress at 10% plastic strain and the initial yield stress ($(\sigma_{0.10}/\sigma_y)$). This ratio equals 1.1 for the low hardening and 10 for the high hardening. For the medium hardening case, the same hardening as the one used in the lamellar cast iron model defined in Section 2.2.2 ($(\sigma_{0.10}/\sigma_y) \approx 2.0$) is used. The models were first subjected to a cool down from processing temperature, as described in the preceding section, and then subjected to 15 thermal cycles (20 °C - 500 °C - 20 °C). As in the previous case, free expansion of the unit cells in all directions is allowed.

In Figure 2.16.b.2, the local response of the considered matrix point is compared for the models with different hardening rates (Figure 2.16.b.1).

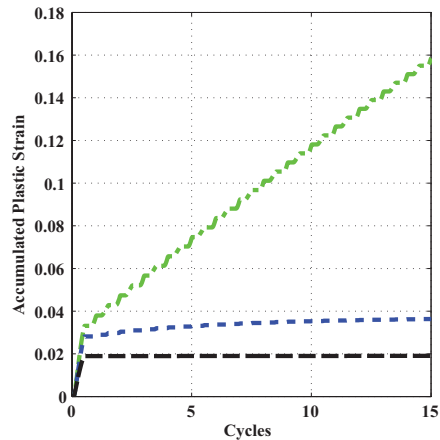
The results presented in Figure 2.16.b show that matrix hardening plays an important role in plastic strain accumulation during thermal cycling. For low hardening, the accumulated plastic strain will increase continuously with every thermal cycle because the yield surface remains nearly constant. On the other hand, in the case of high hardening the accumulated plastic strain saturates after a few thermal cycles, expanding the yield surface sufficiently to prevent further plasticity.



a) anisotropic & isotropic graphite models, influence of strain mismatch



b.1) matrix flow stress curves



b.2) isotropic graphite model, effect of matrix hardening

Figure 2.16: Plastic strain accumulation in the matrix during thermal cycling: a) strain mismatch effect for the isotropic and anisotropic graphite models, b) effect of the matrix hardening: b.1) adopted matrix flow stress curves, b.2) matrix plastic strain accumulation for the isotropic graphite unit cell model with different matrix hardening levels.

2.5 Thermo-mechanical analyses: non-uniform temperature distribution

In the previous section, the thermal expansion response of the lamellar cast iron unit cell model under different thermal loads was discussed. The temperature distribution at the micro level was assumed to be uniform and equal to the macroscopic applied temperature, i.e. no temperature gradient was present. This is a valid assumption if the temperature variations at the representative microstructural size is small enough. In cases where this assumption does not hold, i.e. in the presence of strong temperature gradients, a coupled thermo-mechanical analysis is required. This is the subject of this section. First, heat transfer analysis will be discussed in Section 2.5.1, followed by fully coupled thermo-mechanical simulations in Section 2.5.2.

2.5.1 Heat transfer analyses

The thermal conductivity of cast irons has been extensively studied by Helsing and Grimvall [63] and Holmgren et al. [65, 67, 68, 126] who reviewed different analytical approaches to estimate the effective thermal properties based on microconstituents properties. The limitation of these methods is that they tend to be inaccurate for heterogeneous materials in which one phase forms an interconnected network, like graphite in lamellar cast iron.

In this work, the computational homogenization approach for heat conduction developed by Özdemir et al. [103] (briefly summarized in Appendix C) is used for the heat transfer analysis of lamellar cast iron. The temperature and heat flux distribution at the micro level is thereby determined for a given macroscopic temperature and temperature gradient. These local fields can then be used to estimate the macroscopic thermal conductivity of the material.

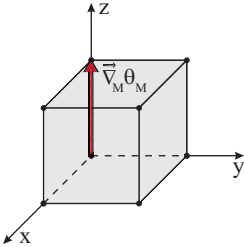
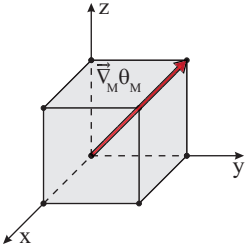
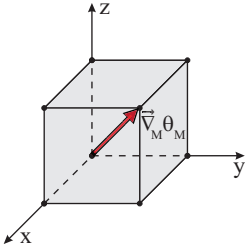
Three different loading cases are defined to determine the effective thermal conductivity of lamellar cast iron. For all load cases, the macroscopic temperature θ_M is linearly increased from 20 °C to 500 °C while the applied temperature gradient is kept constant. To study the influence of the direction of the temperature gradient on the local and overall thermal response of the unit cell, the direction of the temperature gradient has been varied, while leaving its magnitude unchanged. The prescribed macroscopic thermal loading, given by the macroscopic temperature θ_M and temperature gradient $\vec{\nabla}_M \theta_M$, is summarized in Table 2.3.

As in the previous sections, the influence of graphite's anisotropy is assessed by using two models: one with an anisotropic (transversely isotropic) and one with an isotropic thermal conductivity for graphite. The temperature-dependent properties of the different phases are given in Section 2.2 and Figure 2.5.

In Figure 2.17, the local heat flux distribution in the matrix and the graphite for the anisotropic and isotropic graphite unit cell models for load case 1 are presented. In both cases, graphite, which has a higher thermal conductivity than the matrix, is the natural heat conduction path through the material. For this reason, the heat flux in graphite is higher than in the matrix. When the heat flux in the matrix is examined, only small differences between both models can be found. On the contrary, the heat flux distribution in the graphite shows noticeable differences in the response of the

Table 2.3: Thermal loads for heat transfer analyses.

	Load case 1	Load case 2	Load case 3
θ_M	(20 to 500) °C	(20 to 500) °C	(20 to 500) °C
$(\vec{\nabla}_M \theta_M)_x$	0	0	$(20/\sqrt{3})$ °C/mm
$(\vec{\nabla}_M \theta_M)_y$	0	$(20/\sqrt{2})$ °C/mm	$(20/\sqrt{3})$ °C/mm
$(\vec{\nabla}_M \theta_M)_z$	20 °C/mm	$(20/\sqrt{2})$ °C/mm	$(20/\sqrt{3})$ °C/mm

isotropic and anisotropic graphite models. The heat flux in the graphite lamella oriented parallel to the direction of the applied temperature gradient is much higher in the anisotropic graphite model than in the isotropic graphite model. This example clearly shows that the anisotropy of graphite's thermal conductivity plays a key role in the local thermal response of the material.

The local differences in the graphite heat flux is reflected in the global effective conductivity shown in Figure 2.18.a and Figure 2.18.b, for both unit cell models and the three load cases.

Two observations are to be made. First, the macroscopic conductivity is noticeably different for the isotropic and anisotropic graphite model. Second, the estimated macroscopic thermal conductivity obtained from the unit cell model with anisotropic graphite is the same for the three load cases. This shows that the model presents an overall isotropic response at the macro level in spite of the anisotropy of one of the phases. This isotropic thermal conductivity has also been confirmed experimentally. In Figure 2.18.b, the calculated macroscopic thermal conductivities are compared with experimental data available from the literature [3, 68, 120, 126]. The figure shows that the estimate provided by the microstructural unit cell model with anisotropic graphite falls within the band of experimental data, except for temperatures close to room temperature. Despite the uncertainty in the data on thermal conductivity of the graphite and the matrix, see Section 2.2.2, the values used in this work yield a good estimate of the lamellar cast iron thermal conductivity.

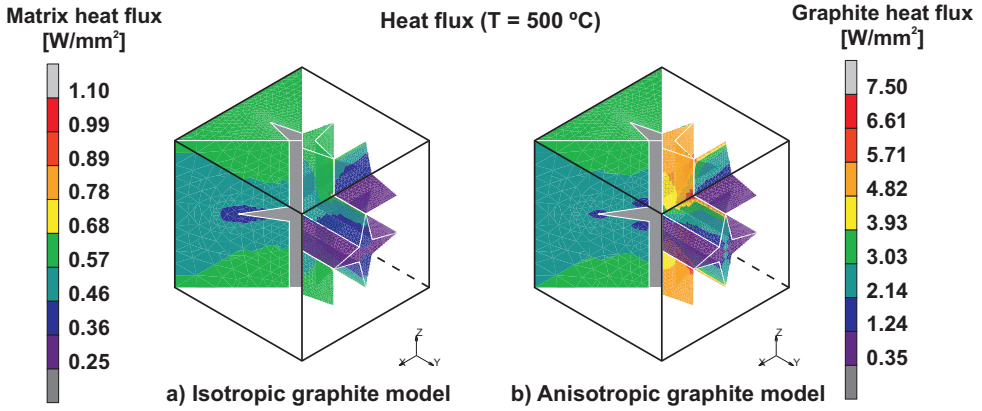


Figure 2.17: Local heat flux distribution in the matrix and graphite for the unit cell models with isotropic (a) and anisotropic graphite (b) at 500 °C for load case 1.

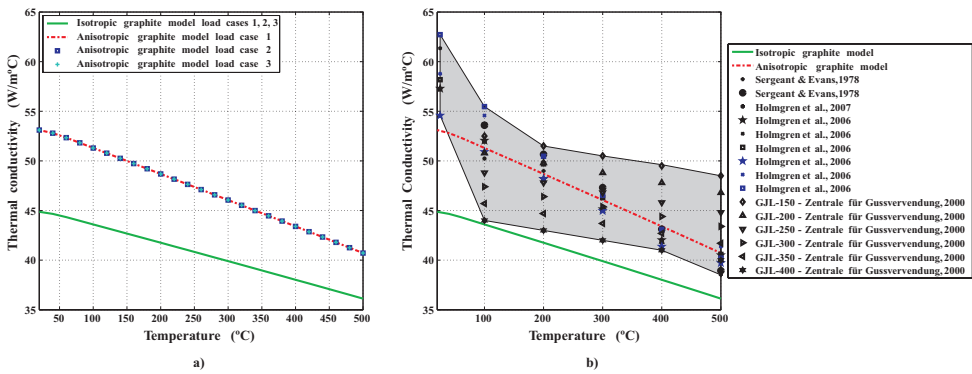


Figure 2.18: Macroscopic thermal conductivity: a) Isotropic graphite model load cases 1,2 and 3 and anisotropic graphite model load cases 1,2 and 3; b) Comparison of the microstructural model estimate with experimental data from literature [3, 68, 120, 126].

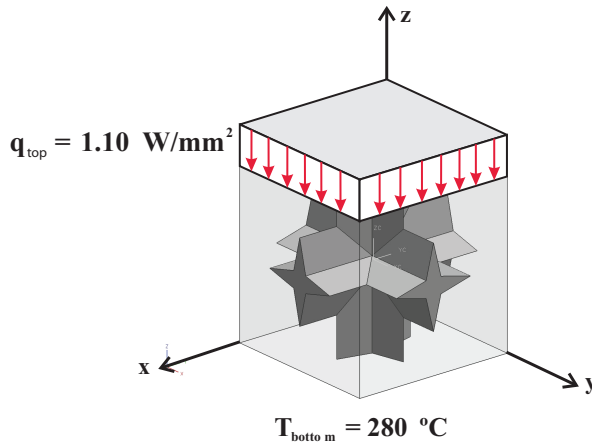


Figure 2.19: Prescribed thermal boundary conditions for the coupled thermo-mechanical analysis

2.5.2 Coupled thermo-mechanical analysis

In order to study the influence of anisotropic on the local temperature and stress fields under general thermo-mechanical loading condition, a coupled thermo-mechanical analysis is next carried out. In this case, the temperature distribution at the micro level is no longer assumed to be uniform. To this end, the model used in Section 2.4 for the thermo-mechanical analyses with a uniform temperature distribution is combined with the model for the heat transfer analysis. This coupled thermo-mechanical analysis is carried out by means of a staggered scheme. For every load increment, the temperature distribution obtained from the thermal analysis is used as the thermal load for the subsequent mechanical analysis.

The prescribed thermal boundary conditions are showed in Figure 2.19: at the bottom of the unit cell the temperature is fixed to $280\text{ }^{\circ}\text{C}$, while at the top a heat flux of 1.1 W/mm^2 is applied, and periodic boundary conditions are used on the lateral faces. With respect to the mechanical boundary conditions, the displacement in the z direction is left free while displacements in the x and y directions are suppressed. Steady state conditions are assumed for the heat transfer analysis.

The resulting temperature profiles are shown in Figure 2.20.a and Figure 2.20.c, emphasising the impact of the graphite thermal conductivity on the heat transfer properties of lamellar cast iron. The temperature difference between top and bottom is smaller in the anisotropic graphite model than in the isotropic one. Moreover, the resulting stresses (Figure 2.20.b and Figure 2.20.d), differ considerably between the models. In this case, not only graphite's anisotropy in the mechanical properties and thermal expansion is responsible for the different results but also the anisotropy of its thermal conductivity.

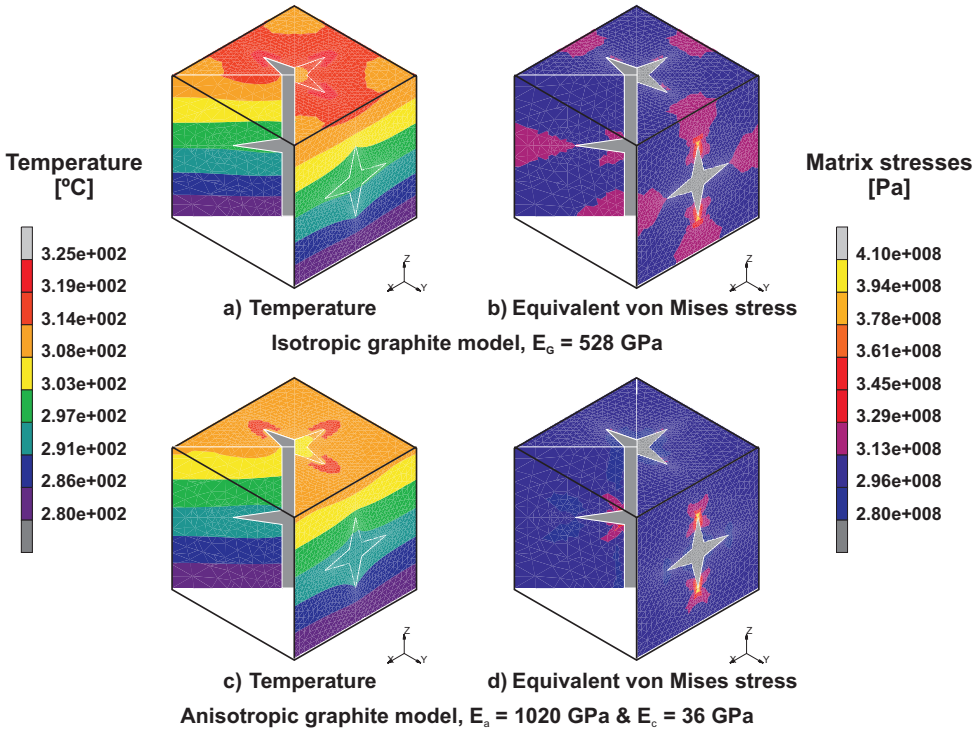


Figure 2.20: Coupled thermo-mechanical analysis: isotropic and anisotropic graphite model temperature distribution and equivalent von Mises stresses.

2.6 Conclusions

In this chapter, a systematic approach for the thermo-mechanical analysis of heterogeneous materials with anisotropic constituents has been presented based on the multi-scale computational homogenization approach. This approach allows to assess the influence of the microstructure on the local and overall mechanical, thermal and thermo-mechanical response. Lamellar cast iron is a typical example revealing highly anisotropic properties for one of its phases. The method itself is general and can be used for other anisotropic composite materials. The morphology of the micro-constituents, the mechanical and thermal non-linearities of the properties of the phases can be included in a straightforward manner. Furthermore, the conclusions presented here partially apply to other (composite) materials with highly anisotropic constituents. From the different analyses carried out the following conclusions result:

- Anisotropy plays a key role in the mechanical, thermal and thermo-mechanical response of heterogeneous materials at the micro and macro scale.
- Analytical models yield inaccurate estimates of the composite CTE when anisotropy is present in one of the phases.

- Replacing an anisotropic constituent with an isotropic one with average mechanical and/or thermal properties leads to an incorrect estimation of the micro-level deformation and temperature fields. The inaccurate description of the behaviour at the micro-level leads to an erroneous prediction of the macroscopic material response. In addition, mechanisms that are strongly related to the local response of the material, e.g. damage, cannot be predicted in a reliable manner.
- The interface condition (fixed or loose) has an important influence on the tensile mechanical response of the material. However, it has virtually no influence on the response in compression. In the thermo-mechanical analysis, and for the thermo-mechanical conditions considered here, the interface has a limited effect on the overall thermal expansion of heterogeneous materials with a 3D interconnected microstructure.
- Prior thermal processing step, may lead to high residual stresses at the microstructural level. These residual stresses lead to a higher macroscopic CTE and to higher local stresses during subsequent operating cycles.
- In the presence of a ductile phase, hardening of the ductile phase plays an important role in plastic strain accumulation over the cycles.

Microstructural study of the mechanical response of CGI: an experimental and numerical approach

Based on
J.C. Pina, S. Shafqat, V.G. Kouznetsova, J.P.M. Hoefnagels, M.G.D. Geers,
Microstructural study of the mechanical response of Compacted Graphite Iron: an experimental and numerical approach, to be submitted.

3.1 Introduction

Cast irons belong to the group of ferrous alloys whose carbon content is higher than 2.14% in weight percentage (wt%). Nevertheless, in most cast irons it is close to 3 wt%. Besides carbon, other alloying elements like silicon, magnesium and copper are frequently added (Table 3.1). The high carbon content present in cast irons leads to the formation of graphite inclusions that give cast irons their characteristic microstructure composed of graphite particles embedded in a pearlitic and/or ferritic matrix. Depending on the chemical composition and cooling rate of the casting process, *lamellar*, *vermicular* or *nodular* graphite inclusions appear. Accordingly, the resulting cast irons are generally classified based on the morphology of the graphite inclusions as: *Flake or Lamellar Graphite Iron (FGI)*, *Compacted or Vermicular Graphite Iron (CGI)* and *Spheroidal, Nodular or Ductile Graphite Iron (SGI)*. While the graphite particles in SGI are more isolated graphite nodules, in FGI and CGI the graphite inclusions form a 3D interconnected network that plays a crucial role in determining the mechanical and thermal properties of the material. In particular, the interconnected graphite network together with its high thermal conductivity and a low thermal expansion results in a material with better heat conduction properties and lower thermal expansion compared to most steels. Furthermore, the vermicular shaped graphite inclusions in CGI, as compared to the sharp lamellas present in FGI, make CGI a material with better mechanical properties than FGI.

The experimental findings in the literature on microstructural deformation mechanisms in cast irons [33, 35, 38, 41, 62, 73, 127] are mostly related to the role played by the interface and the graphite/matrix elastic mismatch in damage initiation and propagation at the microstructural level. The influence of the graphite anisotropy on the microstructural mechanical response of cast irons has only been briefly ad-

dressed, i.e. only in relation to its role in crack initiation within the graphite particles [35]. In terms of microstructural modelling of the local response of nodular cast irons [17, 31, 41, 82] or compacted graphite irons [47, 97], the graphite has been generally considered as an isotropic material, whereby the values assigned to its elastic constants show high variability between different references.

In contrast to the frequently made modelling assumption on graphite isotropy, experimental observations of the structure of graphite particles within cast iron indicate that graphite inclusions present a layered structure with strong covalent bonds within the basal planes (“a” crystallographic direction) and weak van der Waals bonds between them (“c” crystallographic direction) [35, 44, 60, 66, 94, 122, 144]. This structure makes graphite a transversely isotropic material, mechanically strong in the “in-plane” direction and weak in the “out-of-plane” direction.

The crystallographic orientation of graphite within a given particle is determined by its morphology, which in turn is closely related to the particle growth mechanism. Lamellar graphite grows predominantly in the “a” crystallographic direction [44, 60]. As a consequence, the basal planes are parallel to the lamella growth direction. In nodular graphite, the conical graphite crystals grow in a radial pattern from the nucleus along the “c” direction [44, 60, 66, 94]. Vermicular graphite presents a more complex growth pattern which alternates between the “a” and “c” directions [66]. Initially, close to the nucleus, vermicular particles grow in a similar way as nodular graphite. However, upon further growth the branches grow preferentially in the “a” direction as in lamellar graphite [60]. Clearly, the frequently made assumption of isotropic graphite inclusions is invalid, as shown in these observations.

This chapter aims to study the graphite crystallographic anisotropy in vermicular graphite particles and its influence on CGI micromechanical behaviour. In particular the following research question will be addressed:

- How important is the mechanical anisotropy for the distribution of strains and deformation in vermicular graphite particle?

To address this questions, an experimental-numerical approach is followed to study the deformation of the graphite inclusions within CGI. First, in-situ micro-tensile tests on CGI samples are carried out in a scanning electron microscope (SEM). From these tests, a sequence of high resolution images of the deforming graphite particles within CGI is obtained. These images are then used to calculate the strains within the graphite particles via an advanced Global Digital Image Correlation (GDIC) procedure to achieve reliable strain measurements at the scale of the graphite particles (10-50 μm). The method introduce here, combines the use of reference grids on top of the sample together with a dedicated GDIC algorithm to correct for image artifacts and distortions often found in SEM. This is discussed in Section 3.2. The second part of the chapter is dedicated to the development of 2D microstructural models to computationally evaluate the influence of graphite anisotropy on CGI’s mechanical behaviour. To this end, in Section 3.3.1 SEM micrographs are used to create 2D CGI microstructural models. Next, in Section 3.3.2 the computed strains within the graphite inclusions are compared to the experimentally measured strains. Then, in Section 3.3.3, a comparative analysis on the effect of the graphite anisotropy

on the matrix response is performed by confronting the results of two models, one in which some graphite particles are considered anisotropic and one in which all the particles are assumed isotropic. Finally, the main conclusions are presented in Section 3.4.

3.2 Experimental procedure

3.2.1 Material and sample preparation

The material considered here is a pearlitic CGI with a carbon content between 3.60-3.90 weight percentage (wt%). The detailed chemical composition of the material is specified in Table 3.1.

Table 3.1: Chemical composition (wt%) of the pearlitic CGI [51].

C	Ti	Cr	Mn	Cu	Sn	Pb	Si
3.60-3.90	< 0.015	< 0.10	0.15-0.40	0.75-0.95	0.06-0.10	< 0.002	1.90

Dog-bone shaped samples were extracted by electrical discharge machining from the valve bridges of a newly produced truck engine cylinder head. The samples cross section was 1 mm thick and 5 mm width, with a gauge length of 35 mm. Care was taken to develop a reproducible procedure to metallographically prepare the surface of the samples by successive grinding, polishing and fine polishing steps, in order to yield a scratch free surface. No etching was applied to avoid undesirable effects on the graphite/matrix interface.

Tensile tests were carried out using a Kammrath-Weiss micro-tensile stage. The samples were loaded up to fracture by applying a prescribed displacement at a rate of 1 $\mu\text{m/s}$. The micro-tensile stage was placed inside a FEI QUANTA 600 FEG scanning electron microscope (SEM). Four successful high resolution tests were performed. In each test, one graphite particle was preselected and monitored (in-situ) during the tests. Three tests were used to study particles whose principal axis (i.e. parallel to the particle growth direction) was perpendicular to the loading direction, and one in which it was parallel. High resolution micrographs were obtained in the secondary electron (SE) mode at increasing global strain levels. Between four to five micrographs were taken at each global strain level.

3.2.2 SEM based digital image correlation

Quantifying the local deformation of the graphite particles requires the use of a high resolution imaging system such as SEM. However, the use of SEM comes at a cost when it is used together with digital image correlation (DIC) to quantify the deformation of the microstructure. Due to the inherent nature of the imaging

generation by SEM, image artifacts and distortions are frequently present, which are a particular concern at high magnifications and high resolutions [77, 131, 132]. This makes the use of DIC at the length scales required in this work challenging, especially when the strain resolution reflect the variations in local elastic properties in different directions. A more detailed account of the various challenges encountered in SEM with DIC and some related approaches to tackle them can be found in [77, 131, 132]. All these methods, rely on averaging over multiple images to reduce the detrimental influence of SEM scanning artifacts.

Here, an alternative approach is followed which consists in the use of a reference grid surrounding a given region of interest (ROI) within the sample. The reference grid is placed on top of the sample. When the sample is deformed under loading, the reference grid moves with the sample, but remains undeformed. In this work, measurements are performed simultaneously at two length scales: the macroscopic scale of the tensile sample, and the microscopic scale of a graphite particle. Accordingly, two reference grids are used. This is illustrated in Figure 3.1, where the two reference grids are shown. At the macroscopic level an aluminum mask is used as reference grid 1, which is used to correct for the scanning artifacts at a “global” level (Figures 3.1.a and b). At the microscopic level, reference grid 2 is used to correct for the scanning artifacts when measuring at the graphite particle scale (Figures 3.1.c and d). Reference grid 2 is a 5 μm thin micromachined Al-1wt% Cu plate [11], with holes of various sizes.

Image correlation procedure

As discussed in [12, 101, 142], in GDIC an image g taken in the current deformed configuration is correlated with an image f taken in the reference undeformed configuration to determine the unknown displacement field resulting from the deformation of the sample. Based on this method, a novel DIC algorithm has been developed which combines GDIC with the adopted reference grid for each scale (Figure 3.1), thereby minimizing errors triggered by using digital image correlation with SEM images. The development of this improved methodology is explained in detail in a separate paper to be published in the near future, as it involved a mathematical extension of the global DIC algorithm as well as extensive validation tests that go well beyond the scope of the present work. Only the general principles of the methodology are briefly reviewed here.

At each length scale, i.e. sample (macro) scale and graphite particle (micro) scale, the following procedure is used to determine the unknown displacement field:

1. The ROI in both, the reference configuration f and the current configuration g , is masked leaving only the reference grid unmasked (see Figures 3.1.b and 3.1.d).
2. The unmasked and undeformed reference grid in the current configuration g is correlated to the unmasked reference grid of the reference configuration f , yielding an “artificial” displacement field arising only from SEM imaging artifacts.

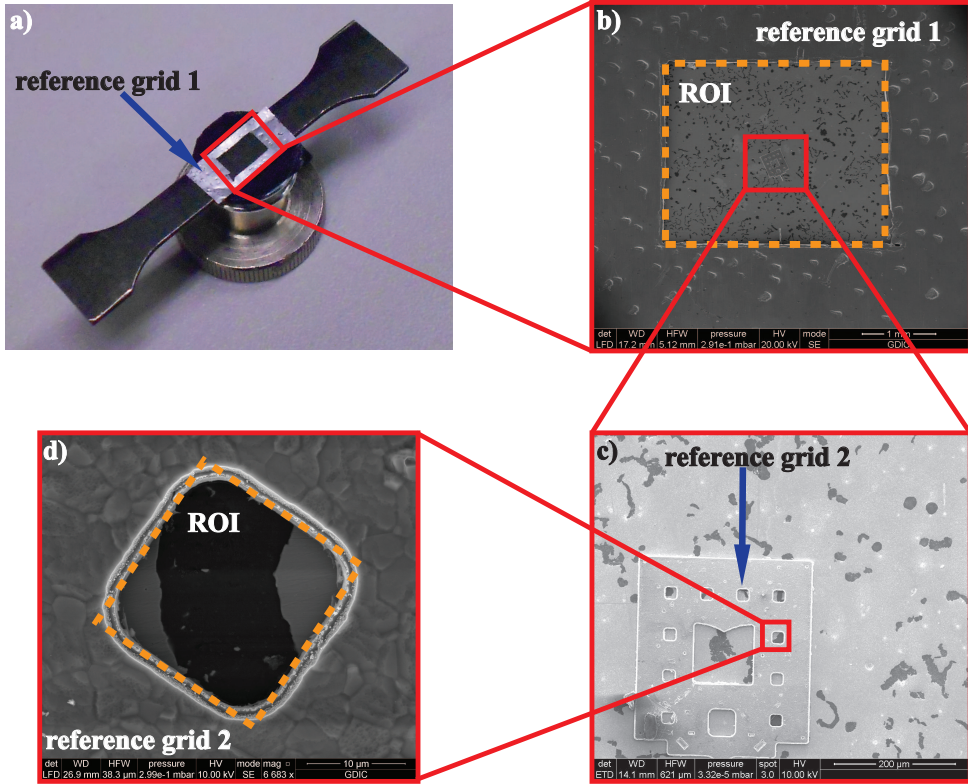


Figure 3.1: CGI tensile sample with reference grids at two different scales: (a,b) macroscopic scale with reference grid 1; (c,d) graphite particle scale with reference grid 2.

3. In the current configuration g , the “artificial” displacement field computed on the reference grid is interpolated over the ROI, and this displacement in the ROI is subtracted from to the current configuration g resulting in a corrected “deformed” image g^* , which should now be nearly artifact free.
4. The reference grid and other image redundant areas, e.g. the metal matrix surrounding the graphite in Figure 3.1.d, are masked in both f and g^* .
5. The unmasked ROI of the “deformed” image g^* , is correlated with its counterpart corresponding to the reference configuration f , yielding the required displacement field corrected for the SEM imaging artifacts and distortions.

This image correlation procedure is used in the following subsection to study the deformation of vermicular graphite particles within CGI.

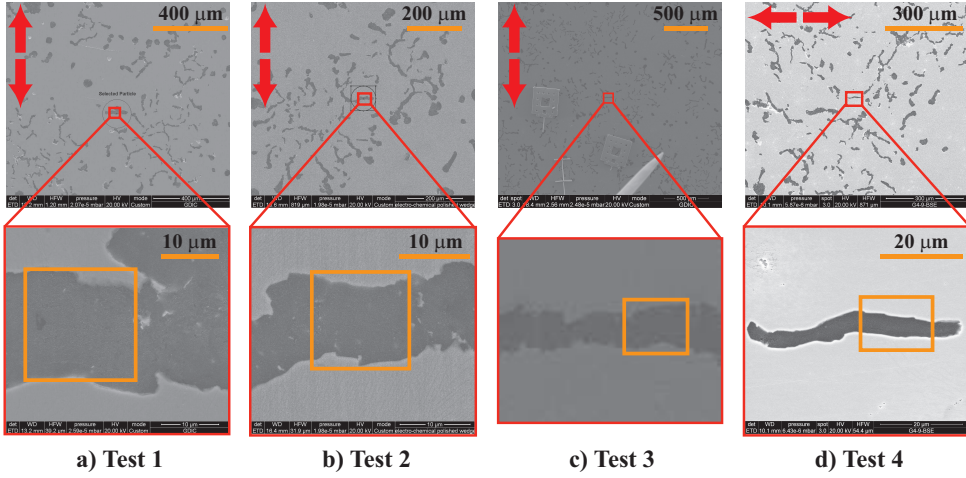


Figure 3.2: Selected graphite particles indicating the area used to measure the strains. The arrows indicate the sample loading direction.

3.2.3 Experimental results

The deformation of the graphite particles within CGI follows a complex pattern which depends on several microstructural characteristics. Some of them are: the shape of the particle and its crystallographic orientation, the particle orientation relative to the loading direction, cracking within the particle and graphite/matrix interface debonding. In the present chapter, the focus is on studying the micro-mechanical behaviour of vermicular graphite particles and the influence of their crystallographic anisotropy. For this reason, in each experiment, the deformation of a simple particle is traced. Then, the strains for each particle are calculated via the GDIC procedure described in the previous subsection.

Three particles oriented perpendicular to the loading direction (tests 1, 2 and 3) and one parallel to the loading direction (test 4) are studied, see Figure 3.2. The particles were selected such that at least one part shows a clearly oriented graphite structure running parallel to the particle long axis. This is indicated in Figure 3.2 where the selected particles are presented and the ROI within each particle is highlighted. Here, it is assumed that the alignment of the visible topographical features on the graphite particle surface is related to the crystallographic orientation of the graphite. This assumption agrees with previous studies performed by Holmgren et al. [66] and Velichko et al. [144]. In this way, graphite’s “a” crystallographic orientation is coincident with the particle’s long axis.

The test results are presented in Figure 3.3 in terms of the measured principal strains, ε_{max} and ε_{min} , within the considered ROI of the particles, as a function of the axial global strain of the sample. For every test and at each loading step, several images were taken, yielding several strains measurements for each test.

The standard deviation, for both principle strains, is shown in Table 3.2 for all tests.

It can be observed that in ε_{max} , the standard deviation is relatively small and in the same range as reported in [131, 132]. The same is observed for the standard deviation of ε_{min} for tests 3 and 4. On the other hand, ε_{min} for tests 1 and 2 reveal a higher standard deviation than the other cases. This can be attributed to the fact that in tests 1 and 2, ε_{min} is oriented along the vertical direction of the images. As discussed in [131, 132], the scanning artifacts are more dominant in the vertical scan direction, resulting in a higher spread in the calculated strains. The achieved resolution in the calculated strains, equals the highest level of accuracy obtained for SEM-DIC until now [131, 132]. Typical SEM artifact correction procedures depend upon averaging techniques integrating numerous images at each loading step. In the method introduced here, a smaller number of images is required at each loading step, considerably enhancing speed. Furthermore, apparent out-of-plane displacements due to rigid body motion of the test specimen or variations in magnification (due to SEM instabilities) can be easily and accurately dealt with.

Table 3.2: Strain resolution.

Strain standard deviation [%]				
	Test 1	Test 2	Test 3	Test 4
ε_{max}	0.011	0.012	0.009	0.019
ε_{min}	0.055	0.035	0.011	0.019

In Figure 3.3.a the principal maximum strain ε_{max} for the particles perpendicular to the loading direction is shown. As expected, when a particle is deformed along its transversal direction (coincident with graphite’s *weak* “c” direction) graphite can be easily deformed, leading to higher strains inside the particles compared to the global axial strain of the sample. This response is consistent for the three particles analysed, which reach peak strains ranging from 0.6% to 1.0%. From this point onwards, in two of the particles, the strain reaches a plateau. The strain saturation can be related to graphite/matrix interface debonding and/or local plastic deformation of the matrix material surrounding the particle as will be discussed in Section 3.3.2. Both of these mechanisms reduce or stop the load transferred from the matrix to the graphite, leading to a drastic change in the slope of the measured strains.

The principal minimum strain ε_{min} for the particles perpendicular to the loading direction is shown in Figure 3.3.b. A higher spread can be noticed in the ε_{min} strain (in tests 1 and 2) as compared to ε_{max} . This is not the case with test 3, in which ε_{min} decreases up to -0.15% and saturates at approximately the same global strain level as ε_{max} . The strains presented in Figure 3.3.b represent the deformation due to lateral contraction in the direction of the *stronger* “a” orientation of the graphite

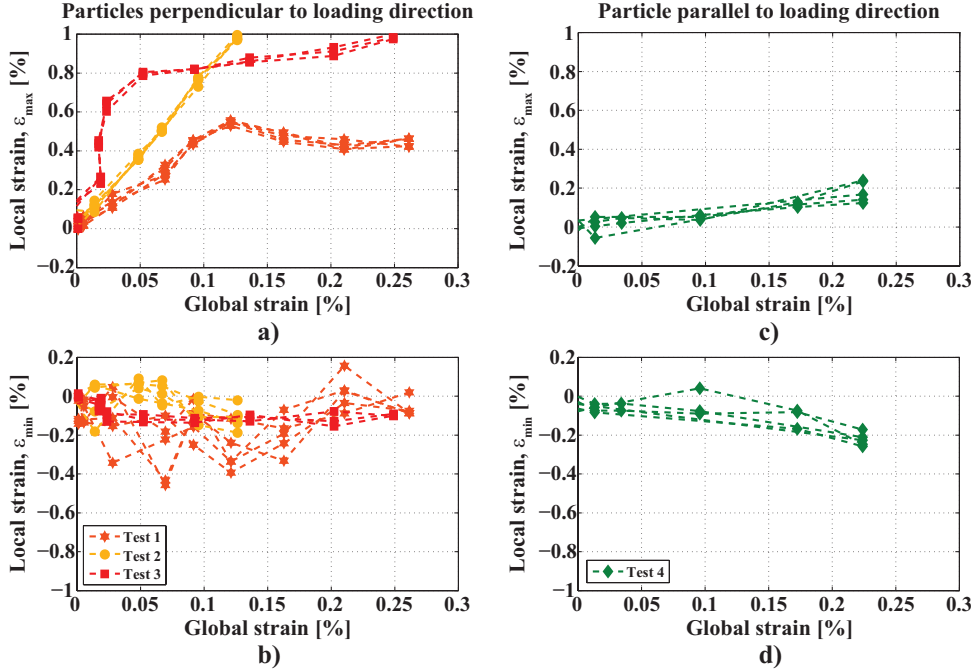


Figure 3.3: Strains in the graphite particles obtained via GDIC: left) particles oriented perpendicular to the loading direction; right) particle oriented parallel to the loading direction. For every test and at each loading step, several images were taken yielding several strains measurements for each test.

particles. Therefore, the graphite shows a higher resistance to the deformation leading to the observed smaller strains.

A different trend is observed for the principal strains within the particle parallel to the loading direction, see Figures 3.3.c and d. Both principal strains appear to grow linearly with increasing global strain, and no signs of nonlinearity can be noticed within the considered applied strain range. The maximum principal strains ϵ_{max} are lower than those shown in Figure 3.3.a. This is due to the relative orientation of the graphite planes within the particle with respect to the loading direction. In test 4, the particle is loaded in a direction which is almost coincident with graphite's strong in-plane "a" direction. Therefore, the resistance of the particle to deformation is considerably higher than in the previous cases (test 1, 2 and 3), where the particles were loaded along the graphite weak "c" direction. For test 4, the weak "c" direction is oriented perpendicular to the loading direction. As a result, the particle can be easily deformed in that direction and the magnitude of ϵ_{min} becomes comparable to the magnitude of ϵ_{max} .

Overall, it can be concluded that the experimental results confirm a pronounced graphite anisotropy within vermicular graphite particles in CGI.

3.3 Numerical simulations

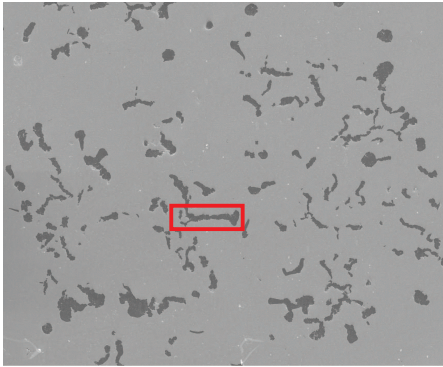
The experimental results discussed in the previous section confirm that vermicular graphite particles are mechanical anisotropic. In this section, numerical simulations are used, to study the influence of the anisotropy of the graphite particles on the local mechanical behaviour of CGI. To this end, two microstructural models, corresponding to two tests discussed in the previous section are created. The models are first used to numerically estimate the strains in the graphite particles investigated in the previous section. The resulting strains are then compared to those obtained from the corresponding experiments in order to quantify the mechanical anisotropy in vermicular graphite particles. Next, the effect of graphite's anisotropy on the surrounding matrix material is examined by looking into the resulting matrix stress and strain fields.

3.3.1 2D CGI microstructural model

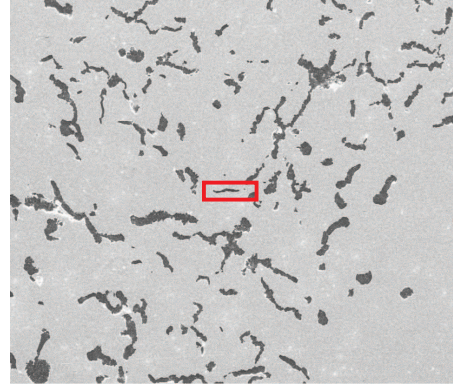
Since a few decades, the Finite Element Method (FEM) based microstructural modelling has become a popular approach to study the microstructural response of materials with complex microstructures. This approach will be pursued here. The use of FEM to model the microstructure allows to incorporate complex material constitutive laws at the level of the phases and interfaces in a straightforward manner. For the simulation, an appropriate Representative Volume Element (RVE) is required, which sufficiently well captures the material microstructure (i.e. volume fraction, morphology and distribution of the different constituents). To this aim, CGI micrographs are directly used to create an RVE with a geometry and FE mesh accommodating the material microstructure. The process involves converting every pixel of the micrograph into a quadrilateral finite element. Next, the pixel grey level is used to define whether it belongs to the matrix or the graphite. In this way, the resulting 2D microstructural model is an adequate representation of the original microstructure. The size of the RVE is defined such that it includes a sufficient number of graphite particles, but does not become too computationally expensive. In addition, the graphite area fraction of each RVE is verified to ensure that it is within the values corresponding to the average graphite content in CGI (10 – 12% volume fraction). Following the above procedure, two RVEs are created: one based on test 3 and one based on test 4 of Section 3.2.3. The original micrographs with the selected regions and the resulting RVEs are presented in Figure 3.4. The resulting number of finite elements in the RVE of test 3 is 509694 and 888264 for the RVE of test 4. In both cases, a plane stress deformation state is assumed.

The CGI investigated in this chapter has a predominant pearlitic matrix composed of 95% pearlite and 5% ferrite. Here, it is assumed that the matrix material is homogeneous isotropic elasto-plastic, with a Young's modulus of 209 GPa and a Poisson's ratio of 0.29. The yield stress evolution (hardening) is described by the model of Allain and Bouaziz [5], which predicts the yield stress of the pearlite-ferrite mixture by evaluating the contributions of both phases. The resulting hardening curve, used as input in the simulations, is presented in Figure 3.5.

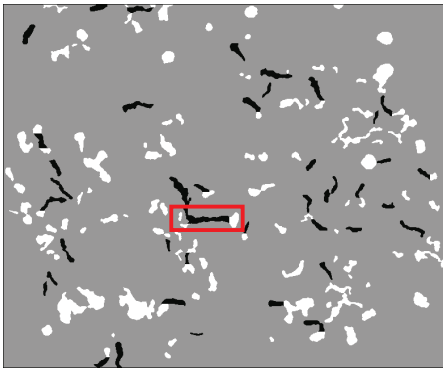
As discussed previously, in general, graphite is a highly anisotropic constituent, as



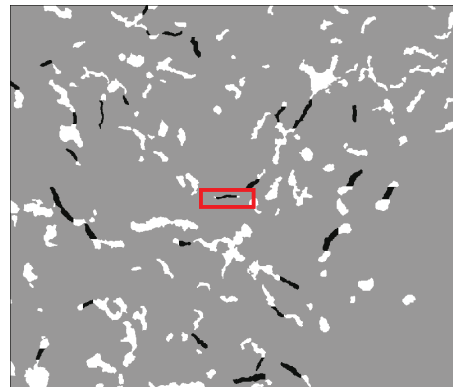
a) Test 3, original microstructure



c) Test 4, original microstructure



b) Test 3, FE model



d) Test 4, FE model

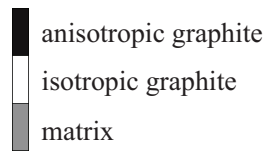
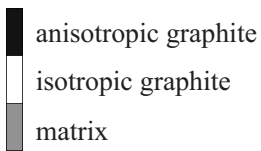


Figure 3.4: 2D CGI microstructural models: left) micrograph and model for test 3; right) micrograph and model for test 4.

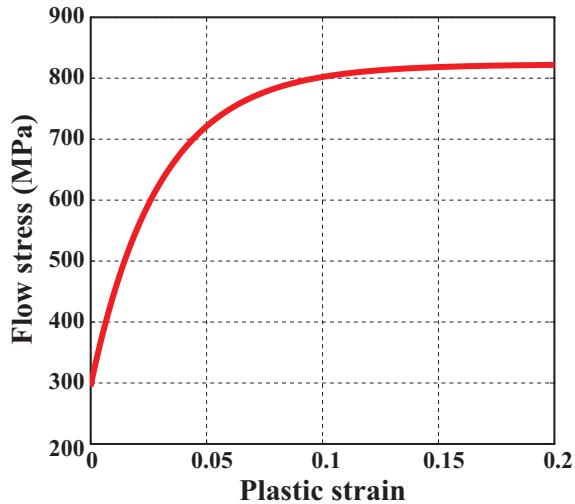
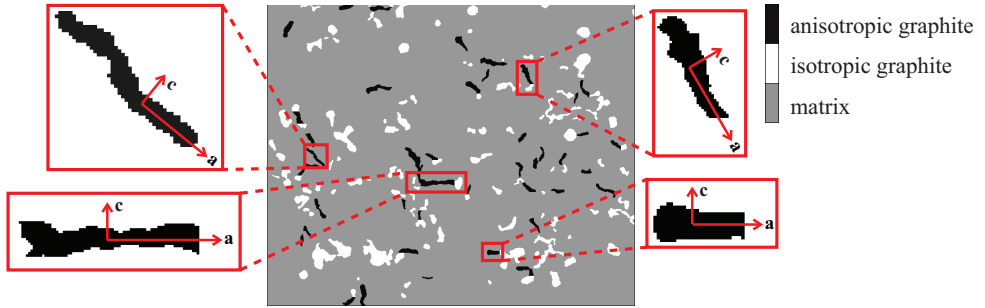


Figure 3.5: Pearlitic matrix yield stress and hardening behaviour.

a consequence of its crystal structure with strong in-plane covalent bonds and weak van der Waals bonds in the out-of-plane direction. Due to this, graphite’s crystallographic orientation in the different graphite particles is expected to play a key role in its mechanical behaviour within CGI. Although lamellar and nodular graphite particles present a clear crystallographic orientation, as discussed in the introduction, the situation is more complex in vermicular graphite due to its particular growth mechanism [60]. For modelling purposes, two groups of particles have therefore been identified: *i*) vermicular particles with a presumed preferred growth direction and corresponding crystallographic orientation; *ii*) graphite particles with an ambiguous growth direction and/or nodular graphite particles, as illustrated in Figure 3.6. In the first group of particles, the crystallographic orientation has been assumed to follow the particle growth direction. As shown in Figure 3.6, this group corresponds to vermicular graphite particles or elongated parts of vermicular particles with a more complex shape. Figure 3.6 also illustrates how the crystallographic orientations of the particles are assigned. In the second group of particles, graphite has been assumed isotropic (Figure 3.6). The anisotropic graphite particles have been modelled as a transversely isotropic material with the elastic constants given by Blakslee *et al.* [15] as summarized in Table 3.3. The elastic constants of the “isotropic” graphite particles are determined by the average of the values between the in-plane and out-of-plane values, i.e. $E = 528$ GPa and $\nu = 0.0875$. In addition, to assess the impact of graphite anisotropy on the local response of CGI, models with only isotropic graphite particles are also considered for comparison purposes. Furthermore, in all the models presented in this chapter, the graphite/matrix interface has been regarded as perfect (fully bonded). Hence comparisons between the numerical and experimental results are only valid up to the point of interface debonding.

Table 3.3: In-plane and out-of-plane Young’s moduli, Poisson’s ratios and shear moduli of graphite [15].

E_a [GPa]	E_c [GPa]	G_{ac} [GPa]	ν_a	ν_{ac}
1020.4	36.364	0.280	0.163	0.012

**Figure 3.6:** Illustration of the assigned crystallographic orientations to the vermicular graphite particles in the CGI microstructural model corresponding to test 3.

The loading applied on the microstructural model mimics the loading on a small microstructural volume within the uniaxial tensile sample. Periodic boundary conditions (as described in Appendix B) are used and a global strain of 0.3% is applied to the RVE in the x-direction such that the resulting average stress state is uniaxial (see Appendix B for more details).

3.3.2 Strains in the graphite particles: experimental vs numerical

In Figure 3.7, the experimentally measured strains in the selected graphite particles (as presented in Section 3.2.3, Figure 3.3) are compared the computed strains from the RVE simulations discussed in the previous section.

Considering the principal strain ε_{max} in both particles, perpendicular (Figure 3.7.a) and parallel (Figure 3.7.c) to the loading direction, it can be noticed that the model with anisotropic graphite qualitatively reproduces the response of both graphite particles better than the model with “isotropic” graphite. Indeed, the principal strain ε_{max} is considerably higher for the particle perpendicular to the loading direction (Figure 3.7.a) than for the one parallel to the loading direction (Figure 3.7.c). On the contrary, no such difference is observed for the model with “isotropic” graphite where the difference in the strains between the two particles is much lower.

Moreover, the slopes of the local strain curves for both ε_{max} and ε_{min} in the particle

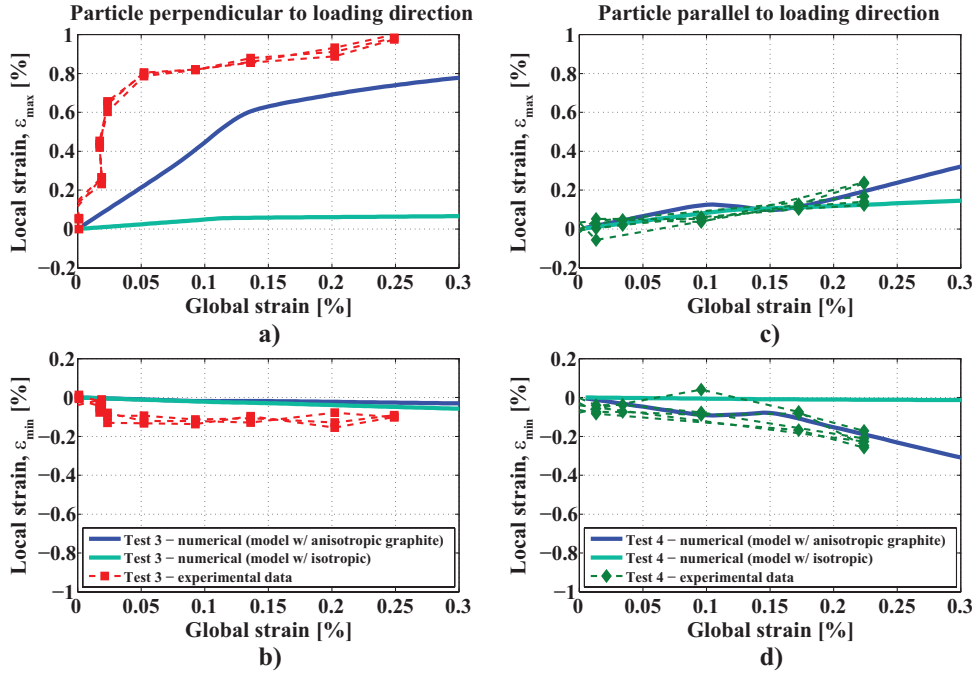


Figure 3.7: Strains in the graphite particles experimental vs numerical results: left) strains in the particles perpendicular to the loading direction; right) strains in particle parallel to the loading direction.

parallel to the loading direction are captured well by the models with the anisotropic graphite. Again, this is not the case for “isotropic” graphite models (Figures 3.7.c and d). Therefore, the results from the simulations seem to confirm that a preferred crystallographic orientation indeed exists within the vermicular graphite particles, triggering the experimentally observed anisotropic mechanical behaviour.

The second effect in Figure 3.7, is the nonlinearity of the local strains with increasing applied global strain, which occurs both in the experimental and numerical results. The most pronounced example of this nonlinearity can be seen in the principal strain ε_{max} in the particle perpendicular to the loading direction (Figure 3.7.a). The numerical simulations indicated that this is related to the local plastic deformation of the matrix next to the graphite particles. This is illustrated in Figure 3.8 where the matrix equivalent plastic strain for test 3, for both the “isotropic” and anisotropic graphite models are presented. The nonlinearity in ε_{max} , which takes place at a global strain of approximately 0.13 %, results from the extensive plastic deformation that occurs in the transition between a global strain of 0.12 % (Figures 3.8.a and c) to 0.135 % (Figures 3.8.b and d). Moreover, Figure 3.7.a also reveals that the non-linearity of the “isotropic” graphite model is much less pronounced as compared to the anisotropic graphite model case. This discrepancy is related to the lower and more homogenous distribution of the local plastic strains in the RVE with “isotropic”

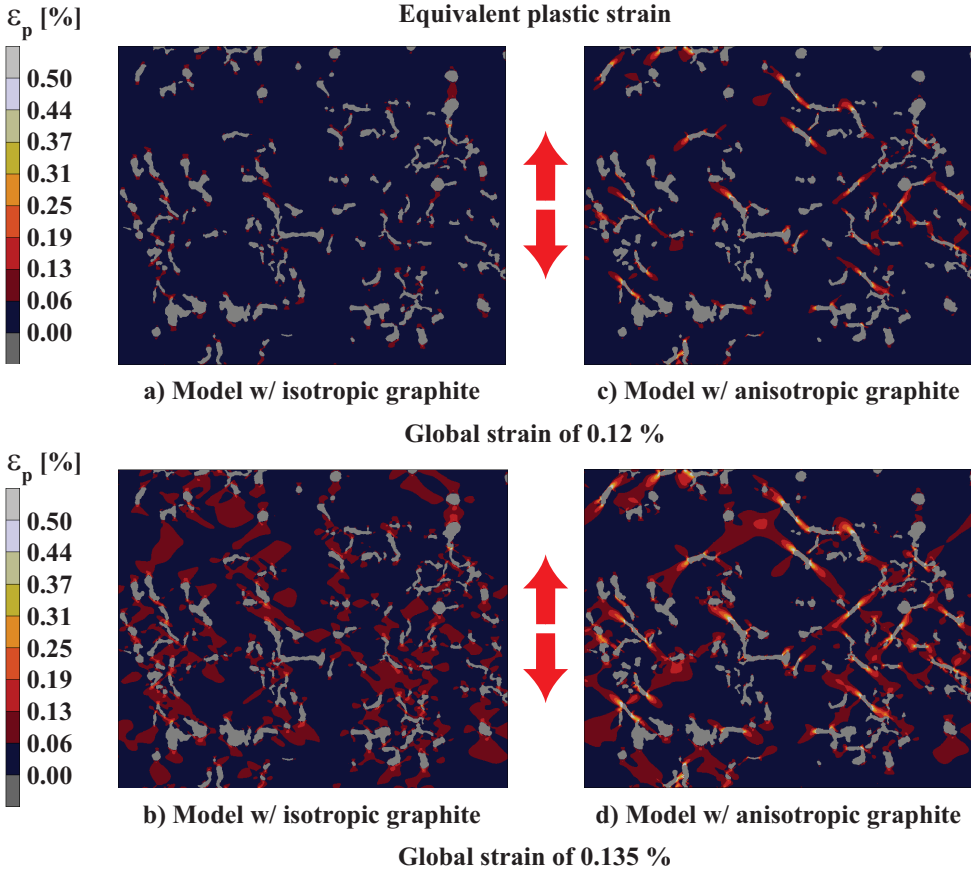


Figure 3.8: Equivalent plastic strain in the matrix for the model of test 3: a), c) global strain of 0.12 %; b), d) global strain of 0.135 %. Left: model with isotropic graphite, right: model with anisotropic graphite. The arrows indicate the loading direction.

graphite particles as shown in Figures 3.8.a and b.

3.3.3 CGI RVE local strain fields

To assess the influence of graphite anisotropy on CGI's local response, the local strain fields obtained from the RVE simulations are further examined. The ε_{22} strain component (parallel to the loading direction) for the RVE corresponding to test 3 is shown in Figure 3.9. The strain component presented is parallel to the loading direction. The strains in the graphite particles are plotted in subfigures a and c, while those in the matrix are plotted in b and d. The results correspond to an applied global strain of 0.15%. At this global strain level, no interface debonding was observed in the tests. The results from the RVE simulations are therefore expected

to provide an adequate description of the real microstructural behaviour, at least qualitatively.

The results show that in the model with anisotropic graphite, high strains are found in the vermicular graphite particles oriented perpendicular to the loading direction while low strains are present in the vermicular particles oriented parallel to the loading direction (Figure 3.9.c). Furthermore, in all particles with no preferential crystallographic orientation, i.e. modelled as isotropic (see Figure 3.4), the resulting strains are low. This observation extends to the model with “isotropic” graphite (Figure 3.9.a), where it applies to all the graphite particles.

The analysis of Figures 3.9.b and d reveals that the response of the matrix is strongly affected by the anisotropy of the graphite particles. The model with “isotropic” graphite (Figure 3.9.b) shows a more uniform distribution of the matrix strains, which on average appear to be higher than the average matrix strain observed in the model with anisotropic graphite (Figure 3.9.d). The higher heterogeneity present in the model with anisotropic graphite can be explained by its more compliant behaviour when deformed in the direction perpendicular to the growth direction. Due to the weak bonding between the graphite basal planes, a similar situation is observed in vermicular particles oriented at an angle with the loading direction, which undergo high shear deformation. As a consequence, when the material is loaded, the deformation will be concentrated in the graphite particles oriented perpendicular or at an angle with respect to the loading direction, reducing the strains in the surrounding matrix (Figure 3.9.d). In addition, at the tip of these particles in the graphite/matrix interface high matrix strains occur which induce plastic deformation, as observed in Figure 3.8.d, and ultimately interface debonding. On the other hand, in the model with “isotropic” graphite, the graphite particles are in all directions more stiff than the surrounding matrix. Hence, the matrix has to deform more to accommodate the global deformation of the material (Figure 3.9.b).

The results confirm that the graphite anisotropy plays an important role in the microstructural response of CGI. Together with the particle orientation relative to the loading direction, the graphite anisotropy determines whether the particle behaves as a hard or soft inclusion. The former reinforces the matrix, while the latter yields high localized deformations and strain concentrations in the surrounding matrix (Figure 3.9). Furthermore, as illustrated in Figure 3.8, the anisotropy in the vermicular graphite particles leads to considerably higher plastic strains in the matrix. As a consequence, the assumption of isotropic graphite can easily lead to an underestimation of the damage initiation and evolution at the microstructural level in CGI.

3.4 Conclusions

The aim of this chapter was to study the mechanical anisotropy of the vermicular graphite particles found in CGI, induced by the intrinsic crystallographic anisotropy of graphite. The experimental and numerical approach used was instrumental to substantiate these analyses, and to understand the influence of the graphite crystallographic anisotropy on the CGI micromechanical response.

The main conclusions of this work are:

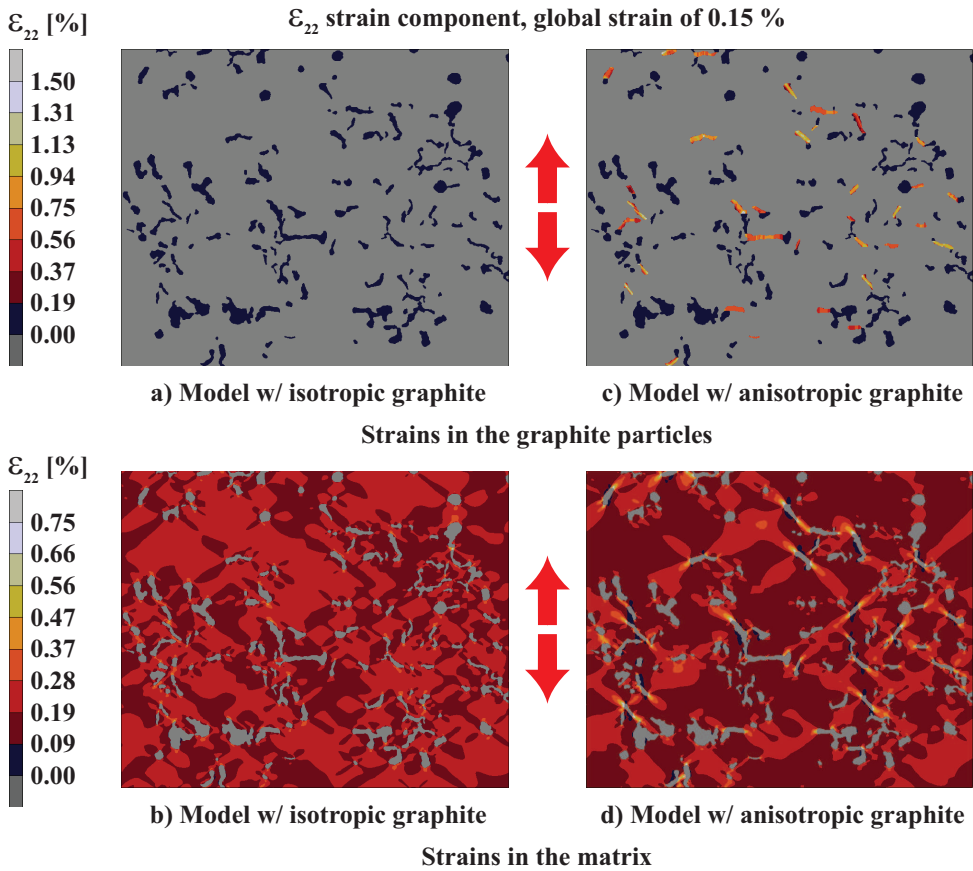


Figure 3.9: ε_{22} strain component (parallel to the loading direction) in the graphite particles (top) and the matrix (bottom) for test 3, at a global strain of 0.15 %. Left: model with isotropic graphite, right: model with anisotropic graphite. The arrows indicate the loading direction.

- A unique experimental procedure has been developed and applied to obtain reliable strain measurements at the scale of the graphite particles (i.e. 10-50 μm). The method makes use of a set of reference grids placed on top of the sample and an advanced GDIC procedure to correct for the image artifacts and distortions frequently present in SEM. This enables to use the high magnification and high resolution imaging capabilities of SEM as required by the dimensions of the graphite particles. Furthermore, small strains have been measured with a standard deviation between $0.9 \cdot 10^{-4}$ to $5 \cdot 10^{-4}$.
- Experimental evidence has been obtained confirming the mechanical anisotropy of vermicular graphite particles in cast irons.
- 2D CGI microstructural models have been developed to study the micromechanical response of CGI. These models have been used to simulate two of the tests performed to measure the strains in the graphite particles. The results from the numerical simulations show that:
 - The strains in the graphite particles estimated from the models show a qualitatively good agreement with the experimentally measured strains.
 - The agreement between the experimental and the numerical results provides a solid confirmation of the hypothesis on graphite is mechanical anisotropy in vermicular graphite particles in cast irons.
 - The nonlinearity of the strains in the graphite particles, as a function of the global applied strain, is the result of a pronounced increase of matrix plastic yielding in the areas surrounding the graphite particles.
 - The anisotropy of the graphite particles has a high impact on the micromechanical response of CGI, in particular regarding the plastic deformation of the matrix material. Therefore, neglecting the anisotropy of the graphite particles, as commonly done in the literature, will lead to an underestimation of the onset of microstructural damage.

Elevated temperature creep of pearlitic steels

Based on
J.C. Pina, V.G. Kouznetsova, M.G.D. Geers,
Elevated temperature creep of pearlitic steels, *Mechanics of Time-Dependent Materials* (2014)
18:611–631.

4.1 Introduction

Pearlitic steels are characterized by high strength, hardness and creep resistance at room temperature. Furthermore, when deformed above the yield limit they show a higher hardening rate than most ferritic steels while presenting acceptable levels of ductility [70, 81, 112]. The reason behind these unique mechanical properties can be traced back to the microstructure. Pearlitic steels have a carbon content that is close to the eutectoid composition (0.76 wt%), which yields a microstructure composed of closely spaced cementite and ferrite layers. It is this particular microstructure of soft ferrite packed between hard cementite walls that leads to the high strength and hardening of pearlitic steels [40, 83]. These properties make pearlitic steels ideal candidates for applications such as railways, springs and wires/cables where structural integrity and minimum irreversible deformation over time are required for the entire service life. Moreover, in the case of drawn wires the high strain hardening behaviour of pearlitic steels allows to reach high strength levels [81].

Most pearlitic steels are used at low temperatures (or room temperature) even though high temperature conditions may apply in some applications. For instance, situations in which steel wires and rails are used in environments where temperatures in excess of room temperature are frequently present, e.g. in the steel making industry where large volumes of molten steel and other alloys need to be handled, or in the facilities for the production of large castings, such as those required for turbines or valves of hydroelectrical power plants. Furthermore, in the case of steel wires used in pre-stressed concrete structures, the behaviour of the material during and after the exposure to high temperatures, e.g. fire, plays a key role in the ability of a building or structure to sustain its structural integrity. This relates not only to the structural response during the fire but also the effect that the high temperature exposure has on the residual properties of steel wires [8]. Another elevated temperature application can be found in diesel engines such as those used for power generation in the

automotive, marine and locomotive industries. For example, in truck engines, the cylinder head and the cylinder block are frequently made of cast iron as well as other high temperature components, e.g. the exhaust manifold. Cast iron is a ferrous alloy composed of graphite inclusions embedded in a largely pearlitic matrix. Due to the engine operating conditions during service life, these components are subjected to long holding times at temperatures in the range between 350 – 550 °C. Under these conditions phenomena like creep and stress relaxation are frequently observed in cast irons [57, 149]. It is reasonable to assume that this time dependent response originates from the pearlitic matrix rather than the graphite inclusions.

The above examples emphasize the importance of understanding the elevated and high temperature response of pearlite. Although the room temperature mechanical behaviour of pearlite and/or pearlitic steels is well documented, little information can be found in the literature regarding the effects of temperature on the mechanical response. The few available studies focus on the role played by the temperature on the strain rate sensitivity of pearlite in relation to Dynamic Strain Aging (DSA) [53, 139]. However, they provide no information regarding to the creep or relaxation behaviour of the material. This matter has been addressed by [8] for drawn pearlitic steel wires, undergoing severe strain hardening during production. Their results show that stress relaxation becomes relevant for temperatures ranging from 300 °C to 400 °C, depending on the pre-load level. Such studies are not available for other pearlitic steels.

From a modelling perspective, rate-independent models have been developed to predict the flow stress of pearlite using properties of the underlying microstructure, such as the interlamellar spacing and the friction stress in the ferrite-cementite lamella [5, 40]. Following a different approach, rate-dependent models have been developed for high strain rate applications, such as modelling of machining processes, with application to cast iron [27, 88, 96]. To the best of our knowledge, up to date, no studies, either experimental or numerical, on the creep and stress relaxation behaviour of pearlite or pearlitic steels have been presented in the literature.

The aim of this chapter is to provide insight into the creep properties of pearlitic steels for temperatures up to 500 °C. To this end, elevated temperature tests are performed on a pearlitic steel, for which a thermo-viscoplastic model is developed. The purpose of the tests is twofold: (1) to provide information on the elevated temperature response of pearlitic steels; (2) to identify the required material parameters. The model is then used to illustrate the influence of temperature and loading on the creep properties of pearlitic steels.

The point of departure for the modelling is the viscoplastic model proposed by [46] for polycrystalline metals. One important aspect of the proposed model is its straightforward characterization procedure, which only requires a reduced set of experimental data. In the model introduced here only steady-state creep-rate data and stress-strain tensile curves at different temperature levels are required.

The novel aspects of the present contribution can be summarized as follows:

- The experimental and numerical results presented in this chapter indicate that the influence of temperature on the mechanical behaviour of pearlitic steels becomes relevant for temperatures above 350 – 400 °C. This leads to fast

deterioration of the creep resistance of the material for temperatures above 350 – 400 °C.

- A thermo-viscoplastic model for pearlitic steels is proposed that allows to study the time and temperature dependent response under creep and stress relaxation conditions. The novel features of the model are:
 - Extension of the model developed by [46] to finite strains.
 - Introduction of a yield surface to account for the characteristic marked yield point found in pearlitic steels.
 - Modification of the thermal function based on the experimental observations.
- Elevated temperature tests (tensile and creep tests) on pearlitic steels are presented, which are used to illustrate the high temperature response of pearlitic steels and to characterize the model parameters:
 - Tensile tests at different temperature levels: 20 °C, 350 °C, 420 °C and 500 °C.
 - Creep tests at 420 °C for different pre-load levels.
 - Set of model parameters obtained from the above experimental data.

The outline of the chapter is as follows. The elevated temperature tests on a pearlitic steel are presented in Section 4.2. The finite strain thermo-viscoplastic model is described in Section 4.3. First, the kinematics, including thermal deformation, is introduced followed by the elastic constitutive model. Then, in Section 4.3.4 the thermo-viscoplastic model is thoroughly discussed together with the relevant evolution equations for the internal variables. Next, in Section 4.4, the stress update algorithm is treated. The parameter identification procedure is presented in Section 4.5. In Section 4.6, the assessment of the model under different loading conditions is performed. Finally, in Section 4.7 the conclusions are discussed.

4.2 Elevated temperature tests on pearlitic steels

4.2.1 Experimental procedure

The elevated temperature tests were performed on C75 pearlitic spring steel sheets of 1 mm thickness. The chemical composition is specified in Table 4.1. Dog-bone-shaped samples were cut from the pearlitic steel sheets, with a cross section of 14.97 mm² and an initial gauge length of 25.34 mm. After cutting, the samples were annealed for two hours at 1150 °C and then cooled down at a rate of 92.5 °C/hr inside the oven under controlled vacuum conditions ($4 \cdot 10^{-3}$ Pa).

The tests were performed in a Gleeble 3800 thermo-mechanical testing system. The system is equipped with a direct resistance heating system to heat up the specimens and water cooled clamps. For the present work, the strain was measured at the centre of the sample with a strain gauge and the tests were carried out in force control mode. The tests were performed under controlled vacuum conditions between 24 and 38.7 Pa.

Table 4.1: Chemical composition (wt%) of the C75 pearlitic steel.

C	Si	Mn	P	S	Cr
0.7080	0.3010	0.7270	0.0085	0.0043	0.3260

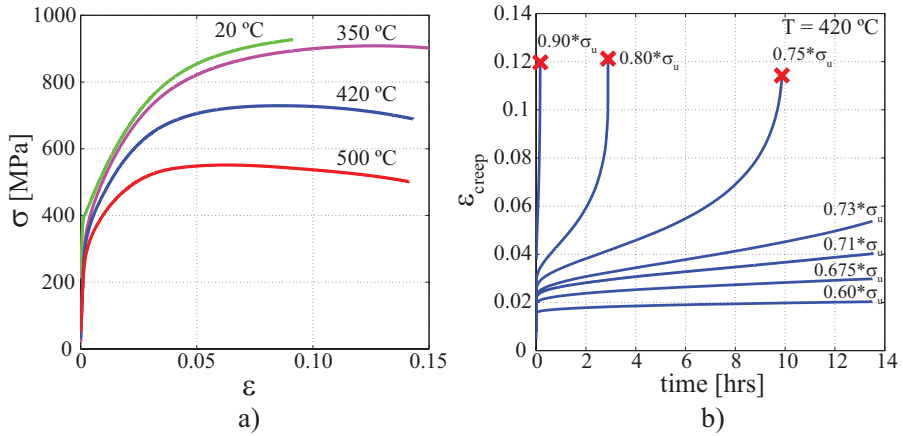


Figure 4.1: Elevated temperature tests on C75 pearlitic steel: a) true stress-strain curves from monotonic tensile tests at different temperatures, and b) creep curves for tests at 420 °C with different load levels; the cross indicates that the sample has failed before the end of the test.

4.2.2 Elevated temperature tests

Two types of tests were performed in order to characterize the elevated temperature response of the pearlitic steel under consideration. First, a set of monotonic tensile tests at temperatures ranging from room temperature to 500 °C and a strain rate of $8 \cdot 10^{-4} \text{ s}^{-1}$ were carried out. Heating-up was done at a rate of 1 °C/s . Two tests were performed at each temperature. Second, a set of creep tests at 420 °C were carried out to characterize the time dependent response of the material. The tests were performed for different load levels ranging from $0.6\sigma_u$ to $0.9\sigma_u$, where σ_u is the tensile strength at 420 °C obtained from the corresponding monotonic tensile test. The same heating rate was used as for tensile testing, but in this case once the test temperature was reached, the temperature was held at this level for 9 hours to stabilize the system before applying the load. The load was applied at a strain rate of $8 \cdot 10^{-4} \text{ s}^{-1}$. A holding time of 13.5 hours was used in all the tests except in those where failure occurred earlier. Two tests were done at each load level. The results from both sets of tests are presented in Figure 4.1. For all the curves, the average between the two measurements is plotted.

From the results shown in Figure 4.1 two interesting features related to the effect of the temperature and the load level can be pointed out. In Figure 4.1.a, it is obvious that between 20 °C and 350 °C the response of the material is only mildly influenced by the temperature. The most noticeable effect is the increase in ductility. For the test temperatures above 350 °C the effect of temperature becomes more significant and even detrimental for the mechanical response of the material. Increasing the temperature leads to a marked drop in the maximum tensile strength (Figure 4.1.a), while the ductility remains nearly the same. The observed thermal softening of pearlitic steels can be related to the increase in deformability of cementite with temperature as revealed by [74]. In their study, [74] evaluated the effect of temperature on the deformation and fracture of cementite in steels. Their findings indicate that cementite becomes highly deformable for temperatures above 400 °C. As a consequence, for temperatures above 400 °C, the deformation of pearlite is no longer exclusively controlled by the movement of dislocations within the ferrite, but also in the cementite layers leading to an overall softer response.

The creep tests at 420 °C, Figure 4.1.b, give insight in the role played by the stress level during the test. As expected, the time to rupture is reduced as the stress level is increased. For stress levels below $0.73\sigma_u$, by the time the test was stopped (after 13.5 hours), fracture was not yet reached. Between, $0.73\sigma_u$ and $0.75\sigma_u$ a sharp transition can be observed and failure is reached within 10 hours. Increasing the creep stress further accelerates the process and the time to rupture reduces further to minutes for $0.90\sigma_u$. In addition, from Figure 4.1.b the elongation at fracture can be determined. A value $\varepsilon_u \approx 12\%$ is found, which is close to the value observed in the tensile test at 420 °C.

The experimental data acquired provides clear evidence of the influence of the temperature and stress level on the mechanical response of pearlitic steels. The results presented in Figure 4.1, indicate that the mechanical response of pearlitic steels becomes sensitive to temperature for temperatures above 350 °C. Moreover, the combination of temperature and stress can lead to plastic deformation and subsequent failure due to creep within hours.

4.3 Thermo-viscoplastic model for pearlitic steels

A principal ingredient in any viscoplastic framework is the definition of the relation between the viscous stress τ_v and the norm of the viscoplastic strain rate or viscoplastic multiplier $\dot{\gamma}_{vp}$. In the literature, several expressions can be found for $\dot{\gamma}_{vp}$, see for example [20] and [36]. In most cases, the relation between $\dot{\gamma}_{vp}$ and the viscous stress τ_v is expressed in terms of a power law function such as in the classical viscoplastic Perzyna model [108]:

$$\dot{\gamma}_{vp} = \eta \left(\frac{\tau_v}{\varphi_0} \right)^N, \quad (4.1)$$

where η is the fluidity parameter, N is the strain rate sensitivity parameter and φ_0 is a scaling parameter or drag strength. Equation (4.1) provides a straightforward relation between $\dot{\gamma}_{vp}$ and τ_v . However, when the effect of temperature needs to be

included, this expression becomes highly non-linear due to the strong dependency of η and N on the temperature [20]. Besides, the unknown functions that describe the relations between η and N and the temperature may be quite complex.

An alternative approach is to separate the effects of temperature and strain rate sensitivity on the viscoplastic strain rate $\dot{\gamma}_{vp}$. This methodology makes use of the Zener-Hollomon decomposition [152,153] of the viscoplastic strain rate, whereby the strain rate sensitivity parameters, such as η and N in (4.1), no longer depend on the temperature. Therefore, the parameter identification process is simplified and the amount of the required experimental data is reduced.

In this work, the latter approach is followed. To this end, a viscoplastic model is developed which stems from the model proposed by [46]. In this model, the viscoplastic strain rate is based on the Zener-Hollomon relation [152,153], in which the viscoplastic strain rate is obtained as the product of two functions: an Arrhenius type thermal function, and a function known as Zener parameter. The thermal function accounts for the sensitivity of the viscoplastic strain rate to the temperature, whereas the Zener parameter characterizes the strain rate sensitivity. This provides a simple way to incorporate the influence of temperature on the viscoplastic strain rate. The evolution of the internal variables due to isotropic hardening, as well as dynamic and thermal recovery are also taken into account. The main differences between the new model and the one originally developed by [46] are:

- Pearlitic steels, as all iron-carbon alloys present a marked yield point that needs to be accounted for. Therefore, a temperature dependent yield surface is included in the model.
- For simplicity, no back stress is considered, i.e. kinematic hardening is not included in the model.
- The model is extended to finite deformations to describe the high visco-plastic strains.

4.3.1 Kinematics

In the present model the kinematics is described in terms of the right Cauchy-Green strain tensor \mathbf{C} defined as:

$$\mathbf{C} = \mathbf{F}^T \cdot \mathbf{F}, \quad (4.2)$$

where \mathbf{F} is the deformation gradient tensor that is classically given by:

$$\mathbf{F} = (\vec{\nabla}_0 \vec{x})^T, \quad (4.3)$$

with $\vec{\nabla}_0$ the gradient with respect to the reference configuration, and \vec{x} the vector that defines the position in the deformed current configuration. See Appendix A for the summary of the notation of tensor operations used in this chapter.

The material velocity is taken into account by the spatial velocity gradient tensor \mathbf{L} and its symmetric and skew-symmetric parts, i.e., the rate-of-deformation tensor \mathbf{D} and the spin tensor $\mathbf{\Omega}$ respectively:

$$\mathbf{L} = (\vec{\nabla} \vec{v})^T = \dot{\mathbf{F}} \cdot \mathbf{F}^{-1} = \mathbf{D} + \mathbf{\Omega}, \quad (4.4)$$

with $\vec{\nabla}$ the gradient with respect to the current configuration, and

$$\vec{v} = \frac{d\vec{x}}{dt}, \quad (4.5)$$

$$\dot{\mathbf{F}} = \frac{d}{dt}(\mathbf{F}). \quad (4.6)$$

The rate of the right Cauchy-Green strain tensor is determined by taking the material time derivative of \mathbf{C} , that is:

$$\dot{\mathbf{C}} = \frac{d}{dt}(\mathbf{F}^T \cdot \mathbf{F}) = \mathbf{F}^T \cdot \dot{\mathbf{F}} + \dot{\mathbf{F}}^T \cdot \mathbf{F} = 2\mathbf{F}^T \cdot \mathbf{D} \cdot \mathbf{F}. \quad (4.7)$$

The thermal and mechanical contributions to the thermo-mechanical deformation process are introduced here via the multiplicative decomposition of the deformation gradient tensor \mathbf{F} into a thermal part \mathbf{F}_{th} and a mechanical part \mathbf{F}_M [59]:

$$\mathbf{F} = \mathbf{F}_{th} \cdot \mathbf{F}_M, \quad J = J_{th} J_M, \quad (4.8)$$

with

$$\mathbf{F}_M = (\vec{\nabla}_0 \vec{x}_M)^T, \quad J_M = \det \mathbf{F}_M > 0, \quad (4.9a)$$

$$\mathbf{F}_{th} = (\vec{\nabla}_M \vec{x})^T, \quad J_{th} = \det \mathbf{F}_{th} > 0, \quad (4.9b)$$

where \mathbf{F}_M performs the mapping between the reference configuration Ω_0 and the intermediate mechanical configuration Ω_M , and \mathbf{F}_{th} maps the deformation from Ω_M to the current configuration Ω . Alternative decompositions can also be found in the literature [59, 69, 85] but they will not be discussed here. The particular choice (4.8) has been made here for algorithmic reasons, as will be evident in section 4.4.1.

In addition, \mathbf{F}_M is further decomposed into elastic and viscoplastic parts via:

$$\mathbf{F}_M = \mathbf{F}_e \cdot \mathbf{F}_{vp}. \quad (4.10)$$

with

$$\mathbf{F}_{vp} = (\vec{\nabla}_0 \vec{x}_{vp})^T, \quad J_{vp} = \det \mathbf{F}_{vp} = 1, \quad (4.11a)$$

$$\mathbf{F}_e = (\vec{\nabla}_{vp} \vec{x}_M)^T, \quad J_e = \det \mathbf{F}_e > 0, \quad (4.11b)$$

where the hypothesis of volume-preserving plastic flow has been used in the definition of \mathbf{F}_{vp} [36].

Considering the multiplicative decomposition of the deformation gradient tensor, equations (4.8) and (4.10), the expression for the spatial velocity gradient tensor \mathbf{L} in terms of its thermal, elastic and viscoplastic parts can be obtained as an additive decomposition:

$$\mathbf{L} = \mathbf{L}_e + \mathbf{L}_{vp} + \mathbf{L}_{th} = (\mathbf{D}_e + \boldsymbol{\Omega}_e) + (\mathbf{D}_{vp} + \boldsymbol{\Omega}_{vp}) + (\mathbf{D}_{th} + \boldsymbol{\Omega}_{th}), \quad (4.12)$$

where \mathbf{L}_e , \mathbf{L}_{vp} and \mathbf{L}_{th} are given by:

$$\mathbf{L}_e = \mathbf{F}_{th} \cdot \dot{\mathbf{F}}_e \cdot \mathbf{F}_e^{-1} \cdot \mathbf{F}_{th}^{-1}, \quad (4.13a)$$

$$\mathbf{L}_{vp} = \mathbf{F}_{th} \cdot \mathbf{F}_e \cdot \dot{\mathbf{F}}_{vp} \cdot \mathbf{F}_{vp}^{-1} \cdot \mathbf{F}_e^{-1} \cdot \mathbf{F}_{th}^{-1}, \quad (4.13b)$$

$$\mathbf{L}_{th} = \dot{\mathbf{F}}_{th} \cdot \mathbf{F}_{th}^{-1}. \quad (4.13c)$$

Finally, an expression for the additive split of $\dot{\mathbf{C}}$ in its thermal, elastic and viscoplastic parts can be obtained by introducing equations (4.8) and (4.10) into (4.7). This yields:

$$\dot{\mathbf{C}} = \dot{\mathbf{C}}_e + \dot{\mathbf{C}}_{vp} + \dot{\mathbf{C}}_{th}, \quad (4.14)$$

with

$$\begin{aligned} \dot{\mathbf{C}}_e &= \mathbf{F}^T \cdot \left[\mathbf{F}_{th} \cdot \dot{\mathbf{F}}_e \cdot \mathbf{F}_e^{-1} \cdot \mathbf{F}_{th}^{-1} + \mathbf{F}_{th}^{-T} \cdot \mathbf{F}_e^{-T} \cdot \dot{\mathbf{F}}_e^T \cdot \mathbf{F}_{th}^T \right] \cdot \mathbf{F} \\ &= 2\mathbf{F}^T \cdot \mathbf{D}_e \cdot \mathbf{F}, \end{aligned} \quad (4.15a)$$

$$\begin{aligned} \dot{\mathbf{C}}_{vp} &= \mathbf{F}^T \cdot \left[\mathbf{F}_{th} \cdot \mathbf{F}_e \cdot \dot{\mathbf{F}}_{vp} \cdot \mathbf{F}^{-1} + \mathbf{F}^{-T} \cdot \dot{\mathbf{F}}_{vp}^T \cdot \mathbf{F}_e^T \cdot \mathbf{F}_{th}^T \right] \cdot \mathbf{F} \\ &= 2\mathbf{F}^T \cdot \mathbf{D}_{vp} \cdot \mathbf{F}, \end{aligned} \quad (4.15b)$$

$$\dot{\mathbf{C}}_{th} = \mathbf{F}^T \cdot \left[\dot{\mathbf{F}}_{th} \cdot \mathbf{F}_{th}^{-1} + \mathbf{F}_{th}^{-T} \cdot \dot{\mathbf{F}}_{th}^T \right] \cdot \mathbf{F} = 2\mathbf{F}^T \cdot \mathbf{D}_{th} \cdot \mathbf{F}. \quad (4.15c)$$

where \mathbf{D}_e , \mathbf{D}_{vp} and \mathbf{D}_{th} are the elastic, viscoplastic and thermal rate-of-deformation tensors, respectively. The constitutive relations for \mathbf{D}_{vp} and \mathbf{D}_{th} will be defined in the following sections.

It should be noted that in the literature the development of the finite deformation (thermo-) elasto-viscoplastic models often follows the concept of dual variables, see e.g. [85] and [61]. The detailed derivations in the view of the dual stress and strain measures pertaining to the multiplicative decomposition (4.8) have been presented by [59].

4.3.2 Thermal deformation

As mentioned before, the thermal effects are incorporated in the model via the thermal part of the deformation gradient tensor \mathbf{F}_{th} , which is assumed to be purely volumetric [59, 85]. For isotropic materials (mechanical and thermal) \mathbf{F}_{th} , can be defined as:

$$\mathbf{F}_{th} = \phi(T)^{1/3} \mathbf{I}. \quad (4.16)$$

The scalar function $\phi(T)$ describes the volumetric deformation induced by a temperature change $(T - T_0)$ relative to a reference temperature T_0 . The simplest form for $\phi(T)$ is [59, 85]:

$$\phi(T) = 1 + \alpha(T - T_0), \quad (4.17)$$

where α is the volumetric thermal expansion coefficient which, in general, can be temperature dependent.

Furthermore, from equations (4.13c) and (4.16) the symmetric and skew symmetric parts of \mathbf{L}_{th} can be obtained as:

$$\mathbf{D}_{th} = \frac{1}{2} \left[\mathbf{L}_{th} + \mathbf{L}_{th}^T \right] = \frac{1}{3} \frac{1}{\phi} \frac{d\phi}{dT} \dot{T} \mathbf{I}, \quad (4.18a)$$

$$\mathbf{\Omega}_{th} = \frac{1}{2} \left[\mathbf{L}_{th} - \mathbf{L}_{th}^T \right] = 0, \quad (4.18b)$$

Equation (4.18b) shows that when it is assumed that \mathbf{F}_{th} induces only volumetric deformations in the material, the thermal spin tensor $\mathbf{\Omega}_{th}$ vanishes.

4.3.3 Thermodynamics based constitutive framework

Following the well established continuum thermodynamics approach, see e.g. [61] among others, the dissipation inequality is used as the point of departure. This inequality states that the specific dissipation at a material point should be non-negative for an arbitrary thermomechanical process. In the form of Clausius-Duhem inequality this reads

$$-\rho_0(\dot{\psi} + \eta\dot{T}) + \frac{1}{2} \mathbf{S} : \dot{\mathbf{C}} - \frac{\vec{q}_0}{T} \cdot \vec{\nabla}_0 T \geq 0 \quad (4.19)$$

where ρ_0 is the mass density with respect to the reference configuration; ψ and η are the Helmholtz free energy and the entropy density, respectively, both per unit of mass; \vec{q}_0 is the heat flux vector per unit referential area and per unit of time. The 2nd Piola-Kirchhoff stress tensor \mathbf{S} is defined as:

$$\mathbf{S} = J\mathbf{F}^{-1} \cdot \boldsymbol{\sigma} \cdot \mathbf{F}^{-T} = \mathbf{F}^{-1} \cdot \boldsymbol{\tau} \cdot \mathbf{F}^{-T}, \quad (4.20)$$

where $\boldsymbol{\sigma}$ and $\boldsymbol{\tau} = J\boldsymbol{\sigma}$ are the Cauchy stress tensor and the Kirchhoff stress tensor, respectively.

The Helmholtz free energy ψ can be taken to consist of two parts, the elastic part $\psi_e(\mathbf{C}_e, T)$ dependent on the elastic deformation and the temperature, for example through the dependence of the elastic constants on the temperature, and the thermal part $\psi_{th}(T)$, see for example [90],

$$\psi(\mathbf{C}_e, T) = \psi_e(\mathbf{C}_e, T) + \psi_{th}(T) \quad (4.21)$$

$$\dot{\psi} = \frac{\partial \psi_e}{\partial \mathbf{C}_e} : \dot{\mathbf{C}}_e + \frac{\partial \psi_e}{\partial T} \dot{T} + \frac{d\psi_{th}}{dT} \dot{T} \quad (4.22)$$

Substitution of (4.14), (4.15), (4.18a) and (4.22) into (4.19), with account for (4.20), gives

$$\begin{aligned} & \left(\frac{1}{2} \mathbf{S} - \rho_0 \frac{\partial \psi_e}{\partial \mathbf{C}_e} \right) : \dot{\mathbf{C}}_e + \boldsymbol{\tau} : \mathbf{D}_{vp} \\ & + \left(\frac{1}{3\phi} \frac{d\phi}{dT} \text{tr}(\boldsymbol{\tau}) - \rho_0 \frac{\partial \psi_e}{\partial T} - \rho_0 \frac{d\psi_{th}}{dT} - \rho_0 \eta \right) \dot{T} - \frac{\vec{q}_0}{T} \cdot \vec{\nabla}_0 T \geq 0 \end{aligned} \quad (4.23)$$

The standard arguments of the Coleman-Noll procedure lead to the constitutive relations for the 2nd Piola-Kirchhoff stress tensor \mathbf{S} and the entropy density η

$$\mathbf{S} = 2\rho_0 \frac{\partial \psi_e}{\partial \mathbf{C}_e} \quad (4.24)$$

$$\eta = \frac{1}{3\rho_0\phi} \frac{d\phi}{dT} \text{tr}(\boldsymbol{\tau}) - \frac{\partial \psi_e}{\partial T} - \frac{d\psi_{th}}{dT} \quad (4.25)$$

and the residual inequalities

$$\boldsymbol{\tau} : \mathbf{D}_{vp} \geq 0 \quad (4.26)$$

$$-\frac{\bar{q}_0}{T} \cdot \vec{\nabla}_0 T \geq 0 \quad (4.27)$$

In the remainder of this chapter only homogeneous temperature fields will be considered and thus the constitutive relation for the entropy (4.25) and the Fourier's inequality (4.27) won't be further elaborated.

Adopting the expression for the elastic free energy as used by [140]

$$\rho_0 \psi_e = \frac{1}{2} \lambda \ln^2(J_e) + \frac{1}{2} \mu [\mathbf{C}_e : \mathbf{I} - 3 - 2 \ln(J_e)] \quad (4.28)$$

with λ and μ the Lamé's constants, which can be expressed as functions of the Young's modulus, E , and Poisson's ratio, ν

$$\lambda = \frac{\nu E}{(1 + \nu)(1 - 2\nu)}, \quad \mu = \frac{E}{2(1 + \nu)} \quad (4.29)$$

relation (4.24) yields

$$\mathbf{S} = \lambda \ln(J_e) \mathbf{C}_e^{-1} + \mu (\mathbf{I} - \mathbf{C}_e^{-1}) \quad (4.30)$$

and in the rate form

$$\dot{\mathbf{S}} = {}^4\mathbb{C}_{elas} : \dot{\mathbf{C}}_e, \quad (4.31)$$

with

$${}^4\mathbb{C}_{elas} = [\mu - \lambda \ln(J_e)] \mathbf{C}_e^{-1} \cdot {}^4\mathbb{I}^{RT} \cdot \mathbf{C}_e^{-1} + \frac{1}{2} \lambda \mathbf{C}_e^{-1} \otimes \mathbf{C}_e^{-1}. \quad (4.32)$$

Note that as a result of (4.14) and (4.15a), both $\dot{\mathbf{C}}_e$ and $\dot{\mathbf{S}}$ are defined in the reference configuration.

4.3.4 Thermo-viscoplastic model

The contribution of the viscoplastic deformation is considered next. A classical expression is used to describe the viscoplastic flow evolution, given by \mathbf{D}_{vp} , which assumes that the viscoplastic deformation accumulates in the direction of the deviatoric stress $\boldsymbol{\tau}^d$, and its magnitude is determined by the rate of the viscoplastic multiplier $\dot{\gamma}_{vp}$:

$$\mathbf{D}_{vp} = \dot{\gamma}_{vp} \mathbf{N}, \quad (4.33)$$

with \mathbf{N} the flow direction, defined in terms of the deviatoric part of the Kirchhoff stress tensor as:

$$\mathbf{N} = \frac{3}{2} \frac{\boldsymbol{\tau}^d}{\tau_{eq}}, \quad \tau_{eq} = \sqrt{\left(\frac{3}{2} \boldsymbol{\tau}^d : \boldsymbol{\tau}^d\right)}. \quad (4.34)$$

Note, that the relations (4.33) and (4.34) ensure the fulfillment of the inequality (4.26). The definition of the plastic flow given by equation (4.33) is completed by postulating a zero viscoplastic spin [36]:

$$\boldsymbol{\Omega}_{vp} = 0. \quad (4.35)$$

Next, $\dot{\gamma}_{vp}$ is defined by a Zener-Hollomon type decomposition [46, 152, 153]:

$$\dot{\gamma}_{vp} = \theta(T)Z(\varphi, D), \quad (4.36)$$

where $\theta(T) > 0$ is an Arrhenius type thermal function and $Z(\varphi, D) > 0$ is the Zener parameter, which is a temperature normalized measure of $\dot{\gamma}_{vp}$; $D > 0$ is the drag strength, accounting for the isotropic hardening. Viscoplastic deformation will take place provided that:

$$\varphi(\tau_{eq}, \tau_y) = \tau_{eq} - \tau_y(T) \geq 0. \quad (4.37)$$

where $\tau_y(T)$ is the yield stress, here assumed to depend on the temperature only, since hardening is accounted for in (4.36).

Evolution equations for the internal variables

To complete the model, a set of equations that describe the evolution of the internal variables, i.e. the viscoplastic strain rate and the drag strength, needs to be provided. The relevant expressions for the evolution of the viscoplastic strain were introduced in the previous section by equations (4.33) and (4.36). From (4.36), the magnitude of the viscoplastic strain rate can be obtained as a function of the current temperature, via $\theta(T)$, and the current stress and hardening levels, via $Z(\varphi, D)$.

Following the steps of [46], we now define the Zener parameter and the drag strength. For the Zener parameter, we depart, as done before by [95] and [46], from the hyperbolic sine function given by [49] for steady-state creep:

$$Z_{ss} \equiv \frac{(\dot{\gamma}_{vp})_{ss}}{\theta(T)} = A \sinh^n \left[\frac{\tau_{eq}}{C} \right], \quad (4.38)$$

where $A > 0$ and $n > 0$ are temperature independent material constants and C is the so-called power-law breakdown strength. The advantage of adopting a hyperbolic sine function for $Z(\varphi, D)$ is its ability to model either the power-law or exponential creep regime depending on the stress level. For stresses below the power-law breakdown, (4.38) reduces to power-law creep where dislocation climb is the rate controlling mechanism. On the other hand, for stresses above the power-law breakdown, where dislocation glide is the rate controlling mechanism, (4.38) becomes exponential [46].

To extend the steady-state Zener parameter to the transient regime, we use the requirement imposed by [46] that under steady-state conditions, the kinetics of viscoplasticity should reduce to the kinetics of creep. In other words, a relation should

exist between equation (4.38) and its transient counterpart. To this end, Freed and Walker [46] proposed that the steady-state and transient Zener parameters should have the same functional form but with a different argument. From this hypothesis an expression for the Zener parameter that accounts for the transient effects can be obtained by introducing the internal state variables that drive the evolution of the viscoplastic strain rate, i.e. the drag strength and the yield stress, into equation (4.38) resulting in the following expression [46]:

$$Z(\varphi, D) = A \sinh^n \left\langle \frac{\tau_{eq} - \tau_y(T)}{D} \right\rangle = A \sinh^n \left\langle \frac{\varphi}{D} \right\rangle, \quad (4.39)$$

The evolution equation for the drag strength is given by [46]:

$$\dot{D} = h(D) [\dot{\gamma}_{vp} - \theta(T)r(D)] = \theta(T)h(D) [Z(\varphi, D) - r(D)], \quad (4.40)$$

with the initial value D_0 the minimum or annealed drag strength. Equation (4.40) describes the evolution of the drag strength as the result of the interaction of strain hardening, dynamic recovery via $h(D)$, and thermal recovery via $r(D)$. The corresponding expressions for $h(D)$ and $r(D)$ are:

$$h(D) = h_D \left[\frac{(D - D_0)/\delta C}{\sinh[(D - D_0)/\delta C]} \right]^m = h_D \left[\frac{\varphi_D}{\sinh[\varphi_D]} \right]^m, \quad (4.41)$$

$$r(D) = A \sinh^n \left[\frac{(D - D_0)}{\delta C} \right] = A \sinh^n [\varphi_D], \quad (4.42)$$

with

$$\varphi_D = \frac{(D - D_0)}{\delta C}, \quad (4.43)$$

where δ and m are material parameters, whose physical meaning will be discussed in Section 4.5.

The effect of the yield stress, the drag strength and the viscoplastic strain rate on the flow stress can be investigated by combining (4.36) - (4.39), which leads to:

$$\tau_{eq} = \tau_y(T) + D \operatorname{arcsinh} \left[\frac{\dot{\gamma}_{vp}}{A\theta(T)} \right]^{\frac{1}{n}}. \quad (4.44)$$

This expression indicates that the flow stress is the result of the contributions of the yield stress $\tau_y(T)$, which depends on temperature only, and the second term that accounts for the isotropic hardening and the effect of the strain rate. The isotropic hardening is introduced in the model via the drag strength D . A non-evolving yield surface, defined by $\tau_y(T)$, is used here to pick up the marked yield point observed in the tensile response of pearlitic steels. The assumption of the yield surface independence of the strain rate, is based on experimental evidence from tensile tests on pearlitic steels [53, 137, 139]. These references indicate that pearlitic steels show a minor dependence of the yield stress on the strain rate, for the range of strain rates considered here.

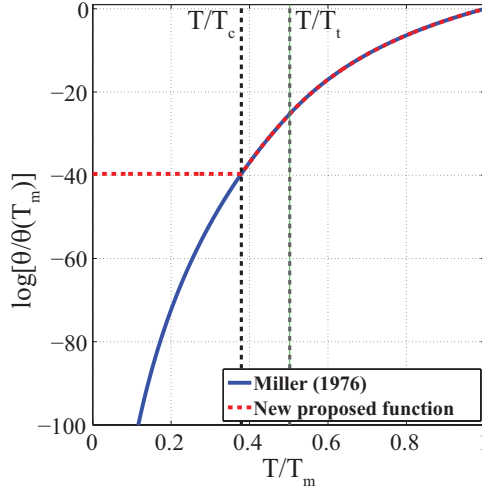


Figure 4.2: Variation of the thermal function θ with temperature. The blue line is the function proposed by [95], the red line illustrates the function proposed here.

Thermal function $\theta(T)$

The thermal function $\theta(T)$ incorporates the effect of temperature into the model in two ways: through expression (4.36) for $\dot{\gamma}_{vp}$, and the evolution equation (4.40) for D . Note, that equation (4.40) does not contain any other temperature dependent material parameters. The influence of temperature is solely introduced through $\theta(T)$.

The expression used here for $\theta(T)$ it is based on the one proposed by [95] (Figure 4.2), which assumes that the activation energy for the plastic flow depends on the temperature, and it is given by [46]:

$$\theta(T) = \begin{cases} \exp\left[\frac{-Q}{RT}\right] & \text{if } T_t \leq T < T_m, \\ \exp\left[\frac{-Q}{RT_t} \left(\ln\left(\frac{T_t}{T}\right) + 1\right)\right] & \text{if } 0 < T \leq T_t, \end{cases} \quad (4.45)$$

where Q is the activation energy for creep, $R = 8.314 \text{ J/molK}$ is the universal gas constant, T_m and $T_t = T_m/2$ are the melting and transition temperatures, respectively.

Based on our experimental observations for pearlitic steels (stress-strain curves at 20 °C, 350 °C, 420 °C and 500 °C, Figure 4.1.a), it can be concluded that below 350 °C the material viscoplastic behaviour presents a low sensitivity to temperature. In other words, below 350 °C, the rate at which plastic deformation and isotropic hardening evolve is hardly influenced by the temperature. Such a material response cannot be reproduced with a thermal function as the one given in equation (4.45). Therefore, a modification of this thermal function is proposed here, motivated by the

experimental data. The corrected thermal function $\theta(T)$ is temperature independent for temperatures below a second transition temperature $T_c = 350^\circ\text{C}$ (Figure 4.2):

$$\theta(T) = \begin{cases} \exp\left[\frac{-Q}{RT}\right] & \text{if } T_t \leq T < T_m, \\ \exp\left[\frac{-Q}{RT_t}\left(\ln\left(\frac{T_t}{T}\right) + 1\right)\right] & \text{if } T_c < T \leq T_t, \\ \exp\left[\frac{-Q}{RT_t}\left(\ln\left(\frac{T_t}{T_c}\right) + 1\right)\right] & \text{if } 0 < T \leq T_c. \end{cases} \quad (4.46)$$

Non-linear system of equations for the viscoplastic behaviour

To summarize, the viscoplastic constitutive model is described by the following set of equations:

$$\dot{\mathbf{S}} = {}^4\mathbb{C}_{elas} : \left[\dot{\mathbf{C}} - 2\mathbf{F}^T \cdot \dot{\gamma}_{vp} \mathbf{N} \cdot \mathbf{F} - 2\mathbf{F}^T \cdot \mathbf{D}_{th} \cdot \mathbf{F} \right], \quad (4.47a)$$

$$\dot{\gamma}_{vp} = \theta(T)Z(\varphi, D), \quad (4.47b)$$

$$\dot{D} = h(D) [\dot{\gamma}_{vp} - \theta(T)r(D)]. \quad (4.47c)$$

where (4.47a) is obtained by substituting equations (4.14), (4.15b), (4.33) and (4.15c) in equation (4.31), with \mathbf{D}_{th} given by (4.18a). The system of equations in (4.47) can be further simplified by introducing (4.47b) into (4.47a) and (4.47c), leading to:

$$\dot{\mathbf{S}} = {}^4\mathbb{C}_{elas} : \left[\dot{\mathbf{C}} - 2\mathbf{F}^T \cdot \theta(T)Z(\varphi, D)\mathbf{N} \cdot \mathbf{F} - 2\mathbf{F}^T \cdot \mathbf{D}_{th} \cdot \mathbf{F} \right], \quad (4.48a)$$

$$\dot{D} = \theta(T)h(D) [Z(\varphi, D) - r(D)]. \quad (4.48b)$$

4.4 Stress update algorithm - Numerical implementation

4.4.1 Incremental time integration

The objective of the constitutive model described in the previous section is to deliver the stress \mathbf{S} and internal variables, D and $\dot{\gamma}_{vp}$, at time $t + 1$ for a given strain or temperature increment, provided that the corresponding values of the stress and internal variables at time t are known. This requires a time integration of the rate equations (4.48). To this end, the first order backward Euler scheme is used here:

$$\mathbf{S} = \mathbf{S}_t + {}^4\mathbb{C}_{elas} : \left[\mathbf{C} - \mathbf{C}_t - 2\mathbf{F}^T \cdot \Delta t \theta(T)Z(\varphi, D)\mathbf{N} \cdot \mathbf{F} - 2\mathbf{F}^T \cdot \Delta t \mathbf{D}_{th} \cdot \mathbf{F} \right], \quad (4.49a)$$

$$D = D_t + \Delta t \theta(T)h(D) [Z(\varphi, D) - r(D)]. \quad (4.49b)$$

where the temperature T is assumed fixed at a given increment and the subscript $t + 1$ has been omitted for clarity.

Furthermore, to obtain the stress in terms of the Kirchhoff stress tensor, we perform the push-forward of \mathbf{S} towards the current configuration by means of \mathbf{F} , which provides the mapping between the reference and the current configuration, this yields:

$$\boldsymbol{\tau} = \mathbf{F}_\Delta \cdot \boldsymbol{\tau}_t \cdot \mathbf{F}_\Delta^T + {}^4\mathbb{H} : [\mathbf{e}_\Delta - \Delta t \theta(T)Z(\varphi, D)\mathbf{N} - \Delta t \mathbf{D}_{th}], \quad (4.50)$$

with the fourth order constitutive tensor ${}^4\mathbb{H}$ defined as:

$${}^4\mathbb{H} = 2\mathbf{F} \cdot \left[\mathbf{F} \cdot {}^4\mathbb{C}_{elas} \cdot \mathbf{F}^T \right]^{LT,RT} \cdot \mathbf{F}^T = 2[\mu - \lambda \ln(J_e)] {}^4\mathbb{I}^{RT} + \lambda \mathbf{I} \otimes \mathbf{I}, \quad (4.51)$$

and the incremental Almansi strain tensor \mathbf{e}_Δ given by:

$$\mathbf{e}_\Delta = \frac{1}{2} \left[\mathbf{I} - \mathbf{F}_\Delta^{-T} \cdot \mathbf{F}_\Delta^{-1} \right], \quad (4.52)$$

where \mathbf{F}_Δ is the incremental deformation gradient tensor, that is related to \mathbf{F} by:

$$\mathbf{F} = \mathbf{F}_\Delta \cdot \mathbf{F}_t. \quad (4.53)$$

Moreover, the elastic predictor of the Kirchhoff stress tensor, assuming no viscoplastic deformation, can be expressed as:

$$\boldsymbol{\tau}_e = \mathbf{F}_\Delta \cdot \boldsymbol{\tau}_t \cdot \mathbf{F}_\Delta^T + {}^4\mathbb{H} : [\mathbf{e}_\Delta - \Delta t \mathbf{D}_{th}]. \quad (4.54)$$

Note, that as a result of the selected multiplicative decomposition (4.8), the thermal velocity gradient tensor \mathbf{L}_{th} , and, consequently, the thermal rate of deformation tensor \mathbf{D}_{th} (both defined in the current configuration) do not involve elastic and viscoplastic terms. In this way, for a given temperature increment, \mathbf{D}_{th} can readily be computed according to (4.18a) and used in the elastic predictor (4.54). The subsequent viscoplastic corrector step can then be applied without any modifications with respect to the temperature independent viscoplastic model as presented by [140].

By introducing (4.54) into (4.50), the total stress can be described as the elastic predictor minus the viscoplastic contribution:

$$\boldsymbol{\tau} = \boldsymbol{\tau}_e - \Delta t \theta(T) Z(\varphi, D) {}^4\mathbb{H} : \mathbf{N}. \quad (4.55)$$

Now, from (4.55) and (4.40) the system of non-linear equations (4.49) can be rewritten as:

$$\mathbf{r}_\boldsymbol{\tau} = \boldsymbol{\tau} - \boldsymbol{\tau}_e + \Delta t \theta(T) Z(\varphi, D) {}^4\mathbb{H} : \mathbf{N} = 0, \quad (4.56a)$$

$$r_D = D - D_t - \Delta t \theta(T) h(D) [Z(\varphi, D) - r(D)] = 0. \quad (4.56b)$$

where $\mathbf{r}_\boldsymbol{\tau}$ and r_D refer to the tensorial residual of the stress equation and the scalar residual of the drag strength equation, respectively.

4.4.2 Newton-Raphson iterative procedure

In the stress update algorithm presented here, for every time increment, an initial trial elastic stress is determined from the predictor (4.54) and the yield condition (4.37) is evaluated. In case that the trial stress exceeds the yield limit, the non-linear system of equations (4.56) needs to be solved to determine the stress and the internal variables. This is performed via a standard Newton-Raphson iterative

procedure, from which the stress and drag strength at iteration $i + 1$ can be obtained as:

$$\boldsymbol{\tau}^{i+1} = \boldsymbol{\tau}^i + \delta\boldsymbol{\tau}, \quad (4.57a)$$

$$D^{i+1} = D^i + \delta D, \quad (4.57b)$$

where $\delta\boldsymbol{\tau}$ and δD are the iterative updates of the stress and drag strength. These iterative updates of the unknowns are determined from the solution of the linearized system of equations. In the present case, this requires the linearization of the residuals $r_{\boldsymbol{\tau}}$ and r_D with respect to the stress $\boldsymbol{\tau}$ and drag strength D yielding:

$$r_{\boldsymbol{\tau}}^{i+1} = r_{\boldsymbol{\tau}}^i + \left. \frac{\partial r_{\boldsymbol{\tau}}}{\partial \boldsymbol{\tau}} \right|_i : \delta\boldsymbol{\tau} + \left. \frac{\partial r_{\boldsymbol{\tau}}}{\partial D} \right|_i \delta D = 0, \quad (4.58a)$$

$$r_D^{i+1} = r_D^i + \left. \frac{\partial r_D}{\partial \boldsymbol{\tau}} \right|_i : \delta\boldsymbol{\tau} + \left. \frac{\partial r_D}{\partial D} \right|_i \delta D = 0. \quad (4.58b)$$

The expressions for the derivatives entering (4.58) are given in Appendix F.

4.5 Parameter identification

The model introduced in Section 4.3 has a total number of twelve material parameters: two elastic constants, E and ν , the thermal expansion coefficient α , and nine parameters describing the viscoplastic part of the model. The Young's modulus, Poisson's ratio and thermal expansion coefficient of carbon steels are well known and can be found in the literature. The values of the Young's modulus used here are given in Table 4.2 [39] and those of the thermal expansion coefficient in Table 4.3 [4]. The Poisson's ratio is assumed equal to 0.29 and temperature independent based on experimental evidence suggesting that there is only a small variation of the Poisson's ratio with temperature [32, 48].

Table 4.2: Elastic material constants of steels [39]

T [°C]	20	204	427	537	649
E [MPa]	207	186	155	134	124

The remaining parameters, except for the melting temperature T_m and activation energy Q , were determined from the experimental data presented in the previous section by means of parameter identification.

The melting temperature T_m was estimated from the Iron-Carbon phase diagram to be 1371 °C. For the activation energy Q , a value of 350 kJ/mol was adopted, which is in line with references found in the literature [53, 133] for the activation energy of pearlite.

Table 4.3: Thermal expansion coefficient [4]

T [°C]	0-100	0-200	0-300	0-400
α [$\mu\text{m}/\text{m}^\circ\text{C}$]	11.6	12.6	13.3	14.0

The parameter identification process is performed in two steps. First, the parameters related to the strain rate sensitivity, i.e. A , C and n , are identified based on the secondary creep data derived from Figure 4.1.b. Then, the yield stress τ_y and the parameters related to the hardening and recovery functions, h_D , δ and m , can be determined from the stress-strain data shown in Figure 4.1.a.

For the identification of A , C and n we follow the approach used by [46], which departs from Garofalo's expression for the steady-state Zener parameter given by equation (4.38). In order to use equation (4.38) in the identification process, data from the steady-state creep strain rate is required. Here, it has been assumed that during the secondary creep regime the material is in steady-state. Therefore, the steady-state creep strain rate $(\dot{\gamma}_{vp})_{ss}$ for each load level can be determined from the creep data shown in Figure 4.1.b, and used together with (4.38) to determine A , C and n . Equation (4.38) with the identified parameters is plotted in Figure 4.3 together with the steady-state experimental data. The values of the strain rate sensitivity parameters and those related to the thermal function are summarized in Table 4.4.

Table 4.4: Strain rate sensitivity and thermal function parameters

Q [kJ/mol]	T_m [°C]	A [s^{-1}]	C [MPa]	n
350	1371	$1.26 \cdot 10^{11}$	91.20	3.82

The last step in the parameter identification procedure consists in finding the yield stress $\tau_y(T)$ and the parameters influencing the hardening and recovery behaviour of the model: the isotropic hardening modulus h_D , the exponent m ($0 \leq m \leq n$) that defines the dominant recovery mechanism, and the parameter δ . When $m \approx 0$, thermal recovery is the dominant mechanism. Whereas, for $m \approx n$ dynamic recovery becomes dominant. $\tau_y(T)$, δ , h_D and m , are identified using the stress-strain data shown in Figure 4.1.a, where the model response is obtained from the solution of the system (4.58). Among these parameters, only $\tau_y(T)$ is temperature dependent. This temperature dependency is captured by identifying the discrete values of $\tau_y(T)$ at each temperature level, i.e. from room temperature to 500 °C, and then adopting

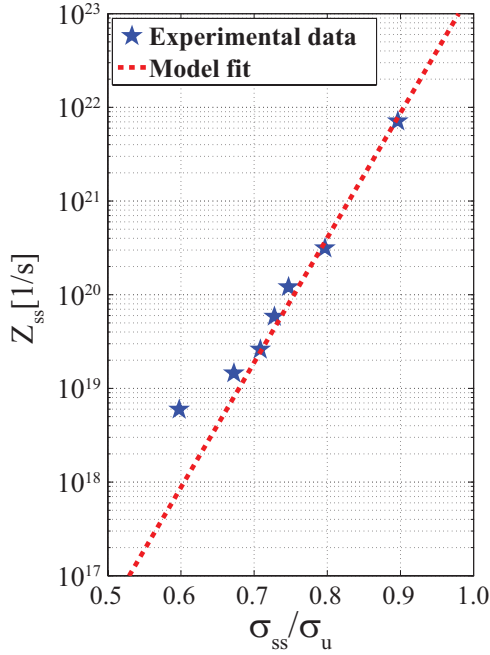


Figure 4.3: Steady-state Zener parameter at 420 °C, experimental data vs. model fit.

a linear variation of $\tau_y(T)$ between the discrete values. The resulting parameters are shown in Table 4.5.

Table 4.5: Yield stress, hardening and recovery parameters.

δ	h_D [MPa]	m	$\tau_y(T)$ [MPa]			
			20 °C	350 °C	420 °C	500 °C
0.075	3133	0.38	324	287	275	240

4.6 Assessment of the model performance under uniaxial loading conditions

In order to evaluate the model predictive capabilities, a set of uni-axial load cases is presented in this section. First, a comparison between the model predictions and the experimental data introduced in Section 4.2.2 is carried out. As evident

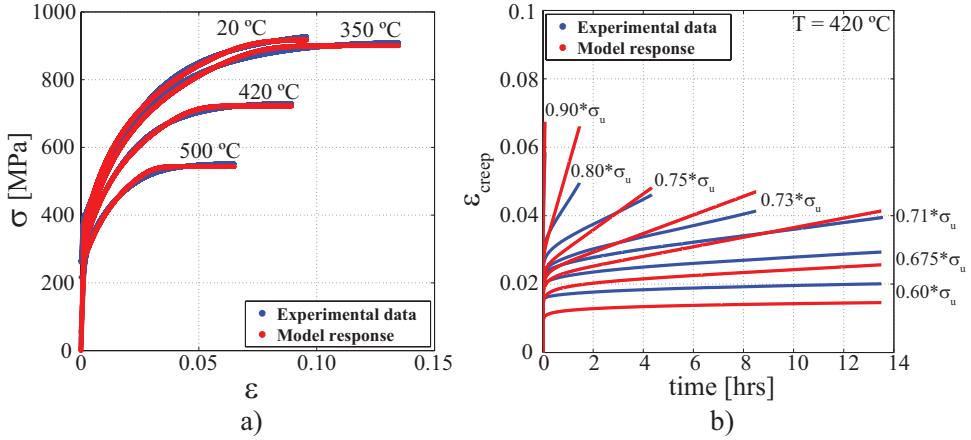


Figure 4.4: Model validation: a) tensile tests, experimental data vs. model response, and b) creep tests at 420 °C, experimental data vs. model prediction.

from the tensile results in Figure 4.4.a, there is an excellent agreement between the experimental data and the model. As for the creep tests (Figure 4.4.b), the comparison between the model predictions and the experimental data is restricted to primary and secondary creep, because the model does not take into account tertiary creep. As may be expected, the model prediction is not as good as in the previous case. However, the model captures well the intrinsic creep behaviour of the material, i.e. the influence of the applied stress on the creep strain and strain rate.

The next two examples, Figure 4.5, are used to illustrate the capabilities of the model to account for the effect of temperature on the material time dependent response. In the first example, Figure 4.5.a, a set of creep tests at different temperature levels are performed. For all the tests, the same stress $\sigma = 550$ MPa, is used. The results suggest that for the given stress level, creep becomes relevant for temperatures above 400 °C. Moreover, once the threshold of 400 °C is passed, a small increase in the temperature leads to a large increase in the creep strain rate (Figure 4.5.a).

The results shown in Figure 4.5.a are consistent with our experimental findings which indicated that above 350 °C the effect of temperature on the mechanical properties becomes significant. Therefore, in view of the experimental data (Figure 4.1) and the numerical examples (Figure 4.5.a) it can be concluded that there is a temperature threshold (between 350 °C to 400 °C) above which a strong temperature dependency of the mechanical properties is triggered. This leads to an increased thermal softening and creep strain rate. The overall effect is a deterioration of the mechanical properties with temperature that will drastically undermine the creep resistance of the material.

The second example (Figure 4.5.b) is aimed to illustrate the sensitivity of the model to small temperature variations. To this end, a temperature jump test is performed. This is a creep test in which a small instantaneous temperature variation ($\pm 10\text{ °C}$) is applied. This perturbation in the temperature should reflect a sharp change of

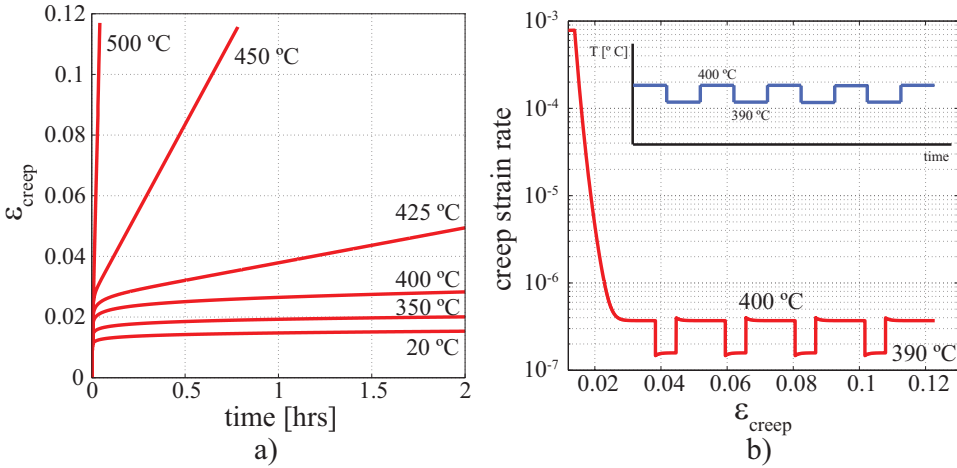


Figure 4.5: Assessment of the influence of temperature on the creep behaviour of pearlitic steel: a) creep at different temperature levels with constant stress $\sigma = 550$ MPa, and b) temperature jump tests between 400 °C and 390 °C.

the creep strain rate. The results shown in Figure 4.5.b, clearly demonstrate that this effect is reproduced by the model. When the test temperature is decreased from 400 °C to 390 °C, the creep strain rate decreases and less creep deformation accumulates during an equal period of time.

4.7 Conclusions

The goal of this chapter was to study the creep behaviour of pearlitic steels in the temperature range between 20 °C and 500 °C. To this end, an experimental-numerical approach was followed. Elevated temperature tests on pearlitic steels were performed and a finite strain thermo-viscoplastic model was developed. The tests gave insight into the elevated temperature mechanical response of pearlitic steels and provided the information required for the identification of the material parameters of the model. The model was also used to further investigate the effect of temperature and load on the elevated temperature response of pearlitic steels. To summarize, the novel aspects are:

- New experimental evidence on the mechanical response of pearlitic steels between 20 °C and 500 °C have been presented. The obtained experimental data (tensile and creep tests), provides clear evidence on the influence of temperature and load on the mechanical response of pearlitic steels.
- A thermo-viscoplastic model for the elevated temperature of pearlitic steels was proposed. The ability of the model to predict the mechanical behaviour of pearlitic steels was illustrated, showing a good agreement with the experimental data.

- Based on the analysis of the obtained experimental data and the numerical examples, it can be concluded that the influence of temperature on the mechanical behaviour of pearlitic steels becomes significant for temperatures above 350 – 400 °C. From this point onwards, there is a strong dependency of the mechanical properties on temperature. This results in a fast decrease of the material resistance to deformation with increasing temperature. This effect is observed in the drop of the flow stress and the sharp increase in the creep strain rate. Consequently, the creep resistance of the material deteriorates dramatically above the 350 – 400 °C temperature threshold and for certain stress levels failure can take place in a matter of hours.
- These results have important implications for the use of pearlite or pearlitic steels in engineering applications in which the material is subjected to temperatures in excess of 350 – 400 °C. At this temperature level, the material no longer exhibits its well known room temperature structural integrity and creep resistance. Therefore, certain combinations of temperature, load and holding time can considerably accelerate the failure of the material and related engineering component.

Time-dependent thermo-mechanical analysis of cast irons

Based on
J.C. Pina, V.G. Kouznetsova, M.P.F.H.L. van Maris, M.G.D. Geers,
Microstructural model for the time-dependent thermo-mechanical analysis of cast irons, submitted to
GAMM-Mitteilungen.

5.1 Introduction

Nowadays, several industrial applications rely on components operating at high temperatures over long periods of time. These applications require materials which can endure the demanding mechanical conditions as well as the often extreme thermal and environmental loads. Cast iron is a typical example of such a material, which has a good compromise between its mechanical and thermal properties, therefore is extensively used for high temperature thermo-mechanical applications. The most prominent examples hereof can be found in the automotive industry, e.g. in cylinder heads and blocks, exhaust manifolds and disk brakes.

The good combination of mechanical and thermal properties of cast iron ensues from its microstructure, composed of graphite inclusions embedded in a ferrite/pearlite matrix. The morphology of the graphite inclusions plays a fundamental role in defining the material properties [44, 116] and is frequently used to identify the different cast irons as: *Nodular or Spheroidal Graphite Iron (SGI)*; *Compacted or Vermicular Graphite Iron (CGI)* and *Flake or Lamellar Graphite Iron (FGI)*. In particular, in CGI and FGI the graphite particles form a 3D interconnected network that, combined with graphite's high thermal conductivity yields thermal properties that are superior to those of steels. Nevertheless, the presence of the graphite inclusions proves to be detrimental for the mechanical properties, because they introduce stress concentration sites promoting damage initiation during the early stages of the material's lifetime [33, 35, 38, 41, 62, 73, 111].

At elevated temperatures, the response of the material becomes more sensitive to temperature and time. This is reflected in thermal softening and higher creep or stress relaxations rates [21–23, 44, 56–58, 78, 91, 113, 114, 146, 154]. This combined with cast iron's highly heterogeneous microstructure, may significantly limit the thermo-

mechanical life performance of the material by accelerating damage initiation and propagation. Therefore, it is imperative to understand the elevated temperature behaviour of cast iron at different length and time scales in order to provide accurate lifetime predictions of the material and design engineering components accordingly. In recent years, a few phenomenological models for thermo-mechanical analyses of cast irons have been developed [118, 119, 134–136]. The main limiting requirement of these models is that they rely on a large amount of experimental data. They do not directly account for the influence of microstructural features on the material thermo-mechanical response (i.e. morphology and anisotropy of the graphite inclusions, matrix time and temperature dependent thermo-mechanical behaviour, interaction between the phases and interface behaviour).

In a different approach, microstructural modelling has been used in the past to study the mechanical response of cast irons: SGI [17, 25–27, 31, 41, 82, 129], CGI [47, 88, 89, 97, 110] and FGI [109]. In addition to the graphite morphology, typical for each cast iron type, other microstructural information has been included in these models:

- graphite anisotropy, to evaluate its influence on the local and global mechanical and thermo-mechanical response of FGI and CGI [109, 110],
- matrix time-dependent response for high strain rate applications (e.g. machining) [25–27, 88, 89, 96],
- graphite/matrix interface [96, 109] and damage [88, 89, 96].

In spite of the vast amount of work done, hardly any attention is given to the combined effect of time and temperature on the *microstructural* mechanical response of cast iron. Therefore, a microstructural model for the elevated temperature mechanical analyses of cast irons is here proposed. The model, is aimed at transient conditions such as the ones present in engines during their operating life in a temperature range between 20 °C and 500 °C. The point of departure for the present analyses is the cast iron microstructural models presented in Chapters 2 and 3, where the temperature dependent thermal and mechanical properties of the graphite and matrix are included, as well as the morphology and anisotropy of the graphite inclusions. Here, the time and temperature dependent behaviour of the pearlitic matrix is added by means of the thermo-viscoplastic model described in Chapter 4. The developed microstructural model is dedicated here to CGI but can be adapted to FGI or SGI in a straightforward manner by introducing the appropriate morphology of the graphite inclusions.

The goal of this chapter is to provide insight into the time-dependent response of CGI for temperatures up to 500 °C. The role played by the microstructure and temperature on the behaviour of the material at both the macro and micro scales is investigated.

In order to assess the validity of the model parameters identified on a pearlitic steel for the pearlitic matrix, micro-indentation tests have been performed.

The results from the elevated temperature analyses indicate that the sensitivity of the material to temperature rapidly increases for temperatures above 400 °C. The higher temperature sensitivity is driven by thermal recovery in the pearlitic matrix.

The combination of time, temperature and microstructural heterogeneity leads to higher local plastic deformation and earlier damage initiation at the microstructural level.

This chapter is organized as follows. In the next section the CGI microstructural model is introduced. In Section 5.2.2, the micro-indentation tests on C75 pearlitic steel and the CGI pearlite matrix are presented together with the pearlite model parameters. The constitutive behaviour of graphite is discussed in Section 5.2.1, and the thermo-viscoplastic model for the pearlitic matrix is described in Section 5.2.3. Then, in Section 5.3, the elevated temperature analyses on CGI are discussed starting with the tensile tests in Section 5.3.1, followed by the numerical stress relaxation tests in Section 5.3.2. The main conclusions are summarized in Section 5.4 and the finite element implementation of the pearlite thermo-viscoplastic model is attached in Appendix G.

5.2 CGI microstructural model

The cast iron investigated in this chapter is CGI with a carbon content between 3.5 to 3.8 wt% and a graphite volume fraction between 10 to 12 % [121]. The matrix is composed of pearlite (95 %) and ferrite (5 %). In CGI, the graphite particles predominantly reveal a vermicular morphology, even though nodular particles are always present [84]. Due to the complex and highly heterogeneous 3D morphology of the vermicular graphite particles, it is challenging and computationally demanding to incorporate all relevant microstructural features present in CGI in a descriptive model.

Here, as in [110] a Finite Element Method (FEM) based computational homogenization approach [80] is used to create a microstructural model for CGI. The Representative Volume Element (RVE) geometry is extracted from a 2D scanning electron microscope (SEM) micrograph. A 2D finite element mesh of this image is obtained by converting each pixel into a finite element. The different phases (matrix or graphite) are identified based on the pixel grey scale level. The main advantage of this method is that the 2D shape of the graphite particles is captured with the experimental resolution. One drawback of this 2D model is that it disregards the inherent 3D nature of the CGI microstructure. Nevertheless, these simplifications make it possible to incorporate microstructural details for a RVE size that would be computationally intractable in 3D, especially in the non-linear regime considered here. The CGI microstructure and the corresponding FEM model are shown in Figure 5.1. The size of the RVE is defined such that it includes a sufficient number of graphite particles with a graphite area fraction of 10.2% (typical for CGI), whereas the size is not too large to compromise the computations.

5.2.1 Graphite

In graphite, anisotropy dominates both the mechanical and thermal properties. This anisotropy is related to graphite's layered structure with strong covalent bonds within the basal planes and weak van der Waals bonds between them, which makes graphite a transversely isotropic material (Figure 5.1.c) [35, 44, 60, 66, 94, 122, 144].

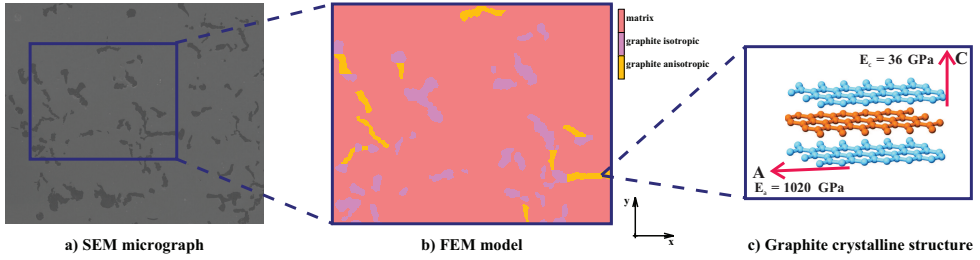


Figure 5.1: CGI microstructure and corresponding FEM model.

In previous work [109, 110], the pronounced effect of graphite’s anisotropy on the local and global response of cast iron has been studied in detail, both numerically and experimentally.

Within cast irons, graphite’s anisotropy is related to the crystalline structure of the graphite particle which in turn is defined by the particle principal growth mechanism [44, 60, 66, 122, 144]. The latter also controls the morphology of the particle. In nodular particles, the principal growth direction is the “c” crystallographic direction, which leads to a “onion” type crystalline structure. On the other hand, lamellar particles grow primarily in the “a” crystallographic direction leading to a crystalline structure in which the graphite platelets are mostly oriented parallel to the “a” direction [44, 60, 66, 94].

In CGI, the predominantly vermicular graphite particles have a growth mechanism that alternates between the “a” and “c” directions. This leads to particles in which some parts resemble the graphite crystalline structure of nodular graphite, while in other parts it resembles the crystalline structure of lamellar graphite [44, 60, 66, 144]. The nodular structure generally occurs close to the nucleus of the particle, whereas the lamellar type structure generally appears in the elongated “worm” shaped branches of the particle. In these parts, a more clearly oriented structure is present with stacked layers of graphite platelets running parallel to the graphite growth direction. It can therefore be reasonably assumed that the graphite in the elongated “worm” like branches of vermicular particles, behaves as transversely anisotropic, with its principal direction (i.e. “a” direction) oriented parallel to the particle growth direction (Figure 5.1.c). The corresponding elastic constants for graphite are given in Table 5.1. The remaining particles, will be assumed isotropic. The elastic constants for isotropic graphite are taken by averaging of the in-plane and out-of-plane properties of graphite, i.e. $E_{11} = E_{22} = 528 \text{ GPa}$ and $\nu_{12} = \nu_{23} = \nu_{31} = 0.0875$.

5.2.2 Matrix

For the pearlite matrix, the thermo-viscoplastic model presented in Chapter 4 is used to describe the time-dependent behaviour of CGI. Because of the complexity of performing an independent model parameter identification process for pearlite within CGI, the same material parameters as obtained in Chapter 4 will be used here. As discussed in Chapter 4, the experimental data required to identify the dif-

Table 5.1: Graphite elastic constants: in-plane (directions 1 & 2) and out-of-plane (direction 3) Young's moduli, Poisson's ratios and shear moduli [15].

$E_{11} = E_{22}$ [GPa]	E_{33} [GPa]	$G_{23} = G_{31}$ [GPa]	ν_{12}	$\nu_{23} = \nu_{31}$
1020.4	36.364	0.280	0.163	0.012

ferent material parameters of the model is obtained from elevated temperature tests (tensile and creep tests) on a C75 pearlitic steel (0.708 weight percent of carbon). To assess whether the pearlitic steel used in the model parameter identification is a valid substitute for the pearlite present in CGI, room temperature micro-indentation tests were performed on both materials. The results from the tests, are shown in Table 5.2, indicating that there is an adequate agreement between both materials in terms of the Young's modulus and the hardness.

Table 5.2: Micro-indentation tests on pearlite in CGI and C75 pearlitic steel

	Pearlite (CGI)	C75
Young's modulus [GPa]	184.0 ± 14.6	190.3 ± 10.7
Hardness [GPa]	3.66 ± 0.54	3.16 ± 0.18

The pearlite thermo-viscoplastic model makes use of twelve material parameters: two elastic constants, E and ν , the thermal expansion coefficient α , and nine parameters describing the viscoplasticity. The value of the Young's modulus used here are given in Table 5.3 [39] and those of the thermal expansion coefficient in Table 5.4 [4]. Poisson's ratio is assumed equal to 0.29 and temperature independent based on experimental evidence showing its minor temperature sensitivity in the considered temperature range [32, 48].

The remaining parameters, except for the melting temperature T_m and activation energy Q , were determined from experimental data on C75 pearlitic steel (from monotonic tensile tests at different temperatures and creep tests at 420 °C). Details are given in Chapter 4. The strain rate sensitivity and thermal function parameters are given in Table 5.5, and those corresponding to the yield stress, hardening and recovery functions are given in Table 5.6. The significance of the different parameters is discussed in the following subsection.

Table 5.3: Elastic material constants of steels [39]

T [°C]	20	204	427	537	649
E [MPa]	207	186	155	134	124

Table 5.4: Thermal expansion coefficient [4]

T [°C]	0-100	0-200	0-300	0-400
α [$\mu\text{m}/\text{m}^\circ\text{C}$]	11.6	12.6	13.3	14.0

Table 5.5: Strain rate sensitivity and thermal function parameters

Q [kJ/mol]	T_m [°C]	A [s^{-1}]	C [MPa]	n
350	1371	$1.26 \cdot 10^{11}$	91.20	3.82

Table 5.6: Yield stress, hardening and recovery parameters.

δ	D_0 [MPa]	h_D [MPa]	m	$\tau_y(T)$ [MPa]			
				20 °C	350 °C	420 °C	500 °C
0.075	9.12	3133	0.38	324	287	275	240

5.2.3 Pearlite thermo-viscoplastic model

The model developed by Pina *et al.* Chapter 4 is used here to account for the time and temperature dependent behaviour of the pearlitic matrix. The model is based on earlier work by Freed and Walker [46]. The viscoplastic strain rate is based on the Zener-Hollomon relation [152, 153], in which the viscoplastic strain rate is obtained as the product of two functions: an Arrhenius type thermal function, and a function

known as the Zener parameter. The thermal function accounts for the sensitivity of the viscoplastic strain rate to temperature, whereas the Zener parameter characterizes the strain rate sensitivity. This provides a simple way to incorporate the influence of temperature on the viscoplastic strain rate. The evolution of the internal variables due to isotropic hardening, as well as dynamic and thermal recovery are also taken into account.

Kinematics

In the present model the kinematics is described in terms of the right Cauchy-Green strain tensor $\mathbf{C} = \mathbf{F}^T \cdot \mathbf{F}$, where $\mathbf{F} = (\vec{\nabla}_0 \vec{x})^T$ is the deformation gradient tensor with $\vec{\nabla}_0$ the gradient with respect to the reference configuration, and \vec{x} the position vector in the current deformed configuration.

The material velocity is taken into account by the spatial velocity gradient tensor \mathbf{L} and its symmetric and skew-symmetric parts, i.e., the rate-of-deformation tensor \mathbf{D} and the spin tensor $\mathbf{\Omega}$ respectively:

$$\mathbf{L} = \dot{\mathbf{F}} \cdot \mathbf{F}^{-1} = \mathbf{D} + \mathbf{\Omega}, \quad (5.1)$$

where the superimposed dot denotes the material time derivative.

The rate of the right Cauchy-Green deformation tensor is determined by taking the material time derivative of \mathbf{C} , that is:

$$\dot{\mathbf{C}} = \mathbf{F}^T \cdot \dot{\mathbf{F}} + \dot{\mathbf{F}}^T \cdot \mathbf{F} = 2\mathbf{F}^T \cdot \mathbf{D} \cdot \mathbf{F}. \quad (5.2)$$

The thermal and mechanical contributions to the thermo-mechanical deformation process are defined through the multiplicative decomposition of the deformation gradient tensor \mathbf{F} into a thermal part \mathbf{F}_{th} and a mechanical part \mathbf{F}_M [59]:

$$\mathbf{F} = \mathbf{F}_{th} \cdot \mathbf{F}_M. \quad (5.3)$$

The tensor \mathbf{F}_M expresses the mapping from the reference configuration Ω_0 to the intermediate mechanical configuration Ω_M , and \mathbf{F}_{th} maps the deformation from Ω_M to the current configuration Ω . The mechanical part \mathbf{F}_M is further decomposed into an elastic and a viscoplastic part via:

$$\mathbf{F}_M = \mathbf{F}_e \cdot \mathbf{F}_{vp}. \quad (5.4)$$

The plastic flow is taken volume-preserving, i.e. $J_{vp} = \det \mathbf{F}_{vp} = 1$ [36].

Considering equations (5.3) and (5.4), the expression for the spatial velocity gradient tensor \mathbf{L} in terms of its thermal, elastic and viscoplastic parts can be obtained as an additive decomposition:

$$\mathbf{L} = \mathbf{L}_e + \mathbf{L}_{vp} + \mathbf{L}_{th} = (\mathbf{D}_e + \mathbf{\Omega}_e) + (\mathbf{D}_{vp} + \mathbf{\Omega}_{vp}) + (\mathbf{D}_{th} + \mathbf{\Omega}_{th}), \quad (5.5)$$

where \mathbf{L}_e , \mathbf{L}_{vp} and \mathbf{L}_{th} are given by:

$$\mathbf{L}_e = \mathbf{F}_{th} \cdot \dot{\mathbf{F}}_e \cdot \mathbf{F}_e^{-1} \cdot \mathbf{F}_{th}^{-1}, \quad (5.6a)$$

$$\mathbf{L}_{vp} = \mathbf{F}_{th} \cdot \mathbf{F}_e \cdot \dot{\mathbf{F}}_{vp} \cdot \mathbf{F}_{vp}^{-1} \cdot \mathbf{F}_e^{-1} \cdot \mathbf{F}_{th}^{-1}, \quad (5.6b)$$

$$\mathbf{L}_{th} = \dot{\mathbf{F}}_{th} \cdot \mathbf{F}_{th}^{-1}. \quad (5.6c)$$

Finally, an expression for the additive split of $\dot{\mathbf{C}}$ in its thermal, elastic and viscoplastic parts can be obtained by introducing equations (5.3) and (5.4) into (5.2). This yields:

$$\dot{\mathbf{C}} = \dot{\mathbf{C}}_e + \dot{\mathbf{C}}_{vp} + \dot{\mathbf{C}}_{th}, \quad (5.7)$$

with

$$\begin{aligned} \dot{\mathbf{C}}_e &= \mathbf{F}^T \cdot \left[\mathbf{F}_{th} \cdot \dot{\mathbf{F}}_e \cdot \mathbf{F}_e^{-1} \cdot \mathbf{F}_{th}^{-1} + \mathbf{F}_{th}^{-T} \cdot \mathbf{F}_e^{-T} \cdot \dot{\mathbf{F}}_e^T \cdot \mathbf{F}_{th}^T \right] \cdot \mathbf{F} \\ &= 2\mathbf{F}^T \cdot \mathbf{D}_e \cdot \mathbf{F}, \end{aligned} \quad (5.8a)$$

$$\begin{aligned} \dot{\mathbf{C}}_{vp} &= \mathbf{F}^T \cdot \left[\mathbf{F}_{th} \cdot \mathbf{F}_e \cdot \dot{\mathbf{F}}_{vp} \cdot \mathbf{F}^{-1} + \mathbf{F}^{-T} \cdot \dot{\mathbf{F}}_{vp}^T \cdot \mathbf{F}_e^T \cdot \mathbf{F}_{th}^T \right] \cdot \mathbf{F} \\ &= 2\mathbf{F}^T \cdot \mathbf{D}_{vp} \cdot \mathbf{F}, \end{aligned} \quad (5.8b)$$

$$\dot{\mathbf{C}}_{th} = \mathbf{F}^T \cdot \left[\dot{\mathbf{F}}_{th} \cdot \mathbf{F}_{th}^{-1} + \mathbf{F}_{th}^{-T} \cdot \dot{\mathbf{F}}_{th}^T \right] \cdot \mathbf{F} = 2\mathbf{F}^T \cdot \mathbf{D}_{th} \cdot \mathbf{F}. \quad (5.8c)$$

where \mathbf{D}_e , \mathbf{D}_{vp} and \mathbf{D}_{th} are respectively the elastic, viscoplastic and thermal rate-of-deformation tensors. The constitutive relations for \mathbf{D}_{vp} and \mathbf{D}_{th} will be defined in the following sections.

Thermal deformation

The thermal effects are incorporated in the model via the thermal part of the deformation gradient tensor \mathbf{F}_{th} , which is assumed to be purely volumetric [59, 85]. For mechanically and thermally isotropic materials \mathbf{F}_{th} , can be defined as:

$$\mathbf{F}_{th} = \phi(T)^{1/3} \mathbf{I}. \quad (5.9)$$

The scalar function $\phi(T)$ describes the volumetric deformation induced by a temperature change $(T - T_0)$ relative to the reference temperature T_0 . The simplest form for $\phi(T)$ is [59, 85]:

$$\phi(T) = 1 + \alpha(T - T_0), \quad (5.10)$$

where α is the volumetric thermal expansion coefficient which, in general, can be temperature dependent.

Furthermore, from equations (5.6c) and (5.9) the symmetric and skew symmetric parts of \mathbf{L}_{th} can be obtained as:

$$\mathbf{D}_{th} = \frac{1}{2} \left[\mathbf{L}_{th} + \mathbf{L}_{th}^T \right] = \frac{1}{3} \frac{\dot{\phi}(T)}{\phi(T)} \mathbf{I} = \mathbf{L}_{th}, \quad (5.11a)$$

$$\mathbf{\Omega}_{th} = \frac{1}{2} \left[\mathbf{L}_{th} - \mathbf{L}_{th}^T \right] = 0, \quad (5.11b)$$

Elastic model

In the constitutive framework applied here, the stress-strain relation is given by a small deformation elastic model which relates the rate of the 2nd Piola-Kirchhoff stress tensor $\dot{\mathbf{S}}$ to the rate of the elastic right Cauchy-Green strain tensor $\dot{\mathbf{C}}_e$. The 2nd Piola-Kirchhoff stress tensor \mathbf{S} is defined as:

$$\mathbf{S} = \mathbf{J} \mathbf{F}^{-1} \cdot \boldsymbol{\sigma} \cdot \mathbf{F}^{-T} = \mathbf{F}^{-1} \cdot \boldsymbol{\tau} \cdot \mathbf{F}^{-T}, \quad (5.12)$$

where $\boldsymbol{\sigma}$ and $\boldsymbol{\tau} = J\boldsymbol{\sigma}$ are the Cauchy and the Kirchhoff stress tensors, respectively. The conventional constitutive relation between $\dot{\mathbf{S}}$ and $\dot{\mathbf{C}}_e$ is then expressed as:

$$\dot{\mathbf{S}} = {}^4\mathbb{C}_{elas} : \dot{\mathbf{C}}_e, \quad (5.13)$$

where ${}^4\mathbb{C}_{elas}$ is the fourth-order elasticity tensor, for an isotropic material given by [140]:

$${}^4\mathbb{C}_{elas} = [\mu - \lambda \ln(J_e)] \mathbf{C}_e^{-1} \cdot {}^4\mathbb{I}^{RT} \cdot \mathbf{C}_e^{-1} + \frac{1}{2} \lambda \mathbf{C}_e^{-1} \otimes \mathbf{C}_e^{-1}, \quad (5.14)$$

with ${}^4\mathbb{I}^{RT}$ the right transpose of the fourth-order identity tensor defined as:

$${}^4\mathbb{I}^{RT} : \mathbf{A} = \mathbf{A}^T. \quad (5.15)$$

In (5.14), λ and μ are Lamé's constants, which can be expressed as functions of the Young's modulus, E , and Poisson's ratio, ν :

$$\lambda = \frac{\nu E}{(1 + \nu)(1 - 2\nu)}, \quad \mu = \frac{E}{2(1 + \nu)}. \quad (5.16)$$

Thermo-viscoplastic model

A classical expression is used to describe the viscoplastic flow, given by \mathbf{D}_{vp} , which assumes that the viscoplastic deformation accumulates in the direction of the deviatoric stress $\boldsymbol{\tau}^d$, whereby its magnitude is determined by the rate of the viscoplastic multiplier $\dot{\gamma}_{vp}$:

$$\mathbf{D}_{vp} = \dot{\gamma}_{vp} \mathbf{N}, \quad (5.17)$$

with \mathbf{N} the flow direction, defined in terms of the deviatoric part of the Kirchhoff stress tensor as:

$$\mathbf{N} = \frac{3}{2} \frac{\boldsymbol{\tau}^d}{\tau_{eq}}, \quad \tau_{eq} = \sqrt{\left(\frac{3}{2} \boldsymbol{\tau}^d : \boldsymbol{\tau}^d \right)}. \quad (5.18)$$

The definition of the plastic flow given by equation (5.17) is completed by postulating a zero viscoplastic spin [36]:

$$\boldsymbol{\Omega}_{vp} = 0. \quad (5.19)$$

Next, $\dot{\gamma}_{vp}$ is defined by a Zener-Hollomon type decomposition [46, 152, 153]:

$$\dot{\gamma}_{vp} = \theta(T) Z(\varphi, D), \quad (5.20)$$

where $\theta(T) > 0$ is an Arrhenius type thermal function and $Z(\varphi, D) > 0$ is the Zener parameter; with $D > 0$ the drag strength, accounting for the isotropic hardening. Viscoplastic deformation will take place provided that:

$$\varphi(\tau_{eq}, \tau_y) = \tau_{eq} - \tau_y(T) \geq 0. \quad (5.21)$$

where $\tau_y(T)$ is the yield stress, which here depends on the temperature only, since hardening is already accounted for in (5.20).

The Zener parameter is defined as:

$$Z(\varphi, D) = A \sinh^n \left\langle \frac{\varphi}{D} \right\rangle = A \sinh^n \left\langle \frac{\tau_{eq} - \tau_y(T)}{D} \right\rangle, \quad (5.22)$$

where $A > 0$ and $n > 0$ are temperature independent rate sensitivity parameters. The expression for $\theta(T)$ is given by:

$$\theta(T) = \begin{cases} \exp \left[\frac{-Q}{RT} \right] & \text{if } T_t \leq T < T_m, \\ \exp \left[\frac{-Q}{RT_t} \left(\ln \left(\frac{T_t}{T} \right) + 1 \right) \right] & \text{if } T_c < T \leq T_t, \\ \exp \left[\frac{-Q}{RT_t} \left(\ln \left(\frac{T_t}{T_c} \right) + 1 \right) \right] & \text{if } 0 < T \leq T_c. \end{cases} \quad (5.23)$$

where Q is the activation energy for creep, $R = 8.314 \text{ J/molK}$ is the universal gas constant, T_m is the melting temperature and $T_t = T_m/2$ and $T_c = 350^\circ\text{C}$ are the transition temperatures.

Finally, the evolution equation for the drag strength D is given by [46]:

$$\dot{D} = h(D) [\dot{\gamma}_{vp} - \theta(T)r(D)] = \theta(T)h(D) [Z(\varphi, D) - r(D)], \quad (5.24)$$

with the initial value $D = D_0$ the minimum or annealed drag strength. Equation (5.24) describes the evolution of the drag strength as the result of the interaction of strain hardening, dynamic recovery via $h(D)$, and thermal recovery via $r(D)$. The corresponding expressions for $h(D)$ and $r(D)$ are:

$$h(D) = h_D \left[\frac{(D - D_0)/\delta C}{\sinh[(D - D_0)/\delta C]} \right]^m = h_D \left[\frac{\varphi_D}{\sinh[\varphi_D]} \right]^m, \quad (5.25)$$

$$r(D) = A \sinh^n \left[\frac{(D - D_0)}{\delta C} \right] = A \sinh^n [\varphi_D], \quad (5.26)$$

with

$$\varphi_D = \frac{(D - D_0)}{\delta C}, \quad (5.27)$$

where C is the power-law breakdown strength, h_D is the isotropic hardening modulus, δ and m are material parameters related to thermal and dynamic recovery.

Non-linear system of equations for the viscoplastic behaviour

To summarize, the viscoplastic constitutive model is described by the following set of equations:

$$\dot{\mathbf{S}} = {}^4\mathbf{C}_{elas} : \left[\dot{\mathbf{C}} - 2\mathbf{F}^T \cdot \theta(T)Z(\varphi, D)\mathbf{N} \cdot \mathbf{F} - 2\mathbf{F}^T \cdot \mathbf{D}_{th} \cdot \mathbf{F} \right], \quad (5.28a)$$

$$\dot{D} = \theta(T)h(D) [Z(\varphi, D) - r(D)]. \quad (5.28b)$$

where (5.28a) is obtained by substituting equations (5.7), (5.8b), (5.17) and (5.8c) in equation (5.13), with \mathbf{D}_{th} given by (5.11a), and using expression (5.20) for $\dot{\gamma}_{vp}$. For the numerical solution of boundary value problems involving this constitutive model, a finite element formulation has been developed and implemented, briefly summarized in Appendix G.

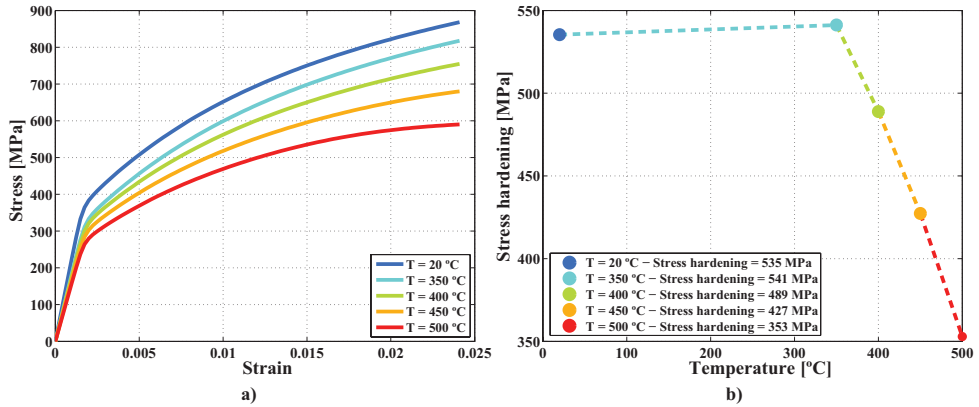


Figure 5.2: Influence of temperature on the uniaxial tensile response of CGI as predicted by RVE simulations: a) homogenized macroscopic stress-strain response; b) stress hardening as a function of temperature.

5.3 Numerical simulations on CGI RVE

In this section, the CGI RVE is used to investigate effect of time, temperature and graphite anisotropy on the mechanical response of CGI. First, monotonic tensile tests at 20, 350, 400, 450 and 500 °C are performed to assess the influence of temperature. Then, the time-dependency is investigated by means of stress relaxation tests, which are carried out at the same temperatures as used in the tensile tests. For all the RVE analyses discussed in this section, periodic boundary conditions, as described in Appendix B, are used.

5.3.1 Elevated temperature uniaxial tensile response

The tensile tests are performed by prescribing a macroscopic strain of 2.5 % to the RVE in the horizontal direction (see Figure 5.1). The deformation is applied in 50 seconds, i.e. with a strain rate of $5 \cdot 10^{-4} \text{ s}^{-1}$. The boundary conditions have been prescribed in such a way that the overall stress state remains uniaxial (see Appendix B).

The resulting macroscopic stress-strain response for the different temperatures is presented in Figure 5.2. From the results shown in Figure 5.2.a, it is obvious that the mechanical performance degrades with increasing temperature. Figure 5.2.b, reveals that also the hardening of the material due to plastic deformation decreases with temperature.

The thermal softening observed in Figure 5.2.a, can also be noticed when comparing the matrix response at 20 °C and 500 °C. The drop in stress hardening with temperature can be traced back to the decrease of drag strength with increasing temperature, following Equation (5.24), as shown in Figure 5.3. At higher temperatures, a higher activation energy promotes thermal recovery which counteracts the effect of strain hardening due to plastic deformation. This is illustrated in Figure 5.4 where the con-

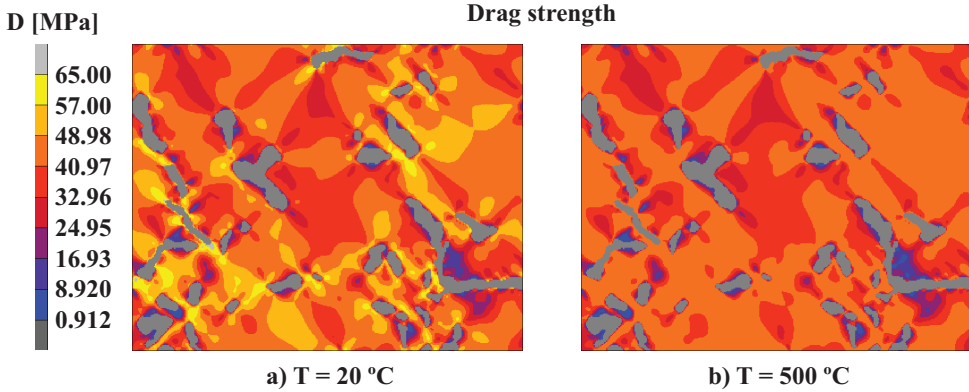


Figure 5.3: Uniaxial tensile test, drag strength D in the matrix phase at the end of macroscopic loading: a) at 20 °C; b) at 500 °C.

contributions to the drag strength from plastic deformation, $D_{\dot{\gamma}_{vp}} = h(D)\Delta t\dot{\gamma}_{vp}$, and thermal recovery, $D_r = -h(D)\Delta t\theta(T)r(D)$, are separately presented. Figures 5.4.a and 5.4.b, reveal that the higher activation energy at 500 °C not only enables thermal recovery but also enhances plastic flow, leading to a higher contribution of $D_{\dot{\gamma}_{vp}}$ to the drag strength. Nevertheless, with the pearlite parameters used, the increase in $D_{\dot{\gamma}_{vp}}$ at 500 °C is counteracted by the thermal recovery such that the overall drag strength D is lower than at 20 °C.

The high microstructural heterogeneity of cast irons (graphite morphology and properties of the phases), and the temperature-dependency, has an important effect on the distribution of the local microstructural fields. As shown in Figures 5.5.a and 5.5.b, high stress and strain concentrations arise at various locations surrounding the graphite particles. The most critical areas, are those in the vicinity of anisotropic graphite particles whose long axis is oriented at 45° with respect to the loading direction, especially in regions where several particles are clustered together (see Figure 5.1). The anisotropic graphite particles oriented transversely to the loading direction show little resistance to deformation upon loading. Consequently, high strains are observed within these graphite particles (Figure 5.6), and in the matrix adjacent to the tip of the particles, which behaves as a notch in the matrix. The magnitude of the strains at these spots extends far into the matrix leading to the formation of strain percolation paths (Figures 5.5.c and 5.5.d). At higher temperatures, this effect is enhanced even further as demonstrated in Figures 5.5.b and 5.5.d. At 500 °C, the stress fields are only half the magnitude of those at 20 °C, yet they entail higher and more extensive plastic strains. Therefore, it can be expected that damage will initiate earlier and propagate faster at higher temperatures.

5.3.2 Stress relaxation

The stress relaxation simulations are carried out at the same temperatures as the uniaxial tensile tests described in the previous section: 20, 350, 400, 450 and 500 °C.

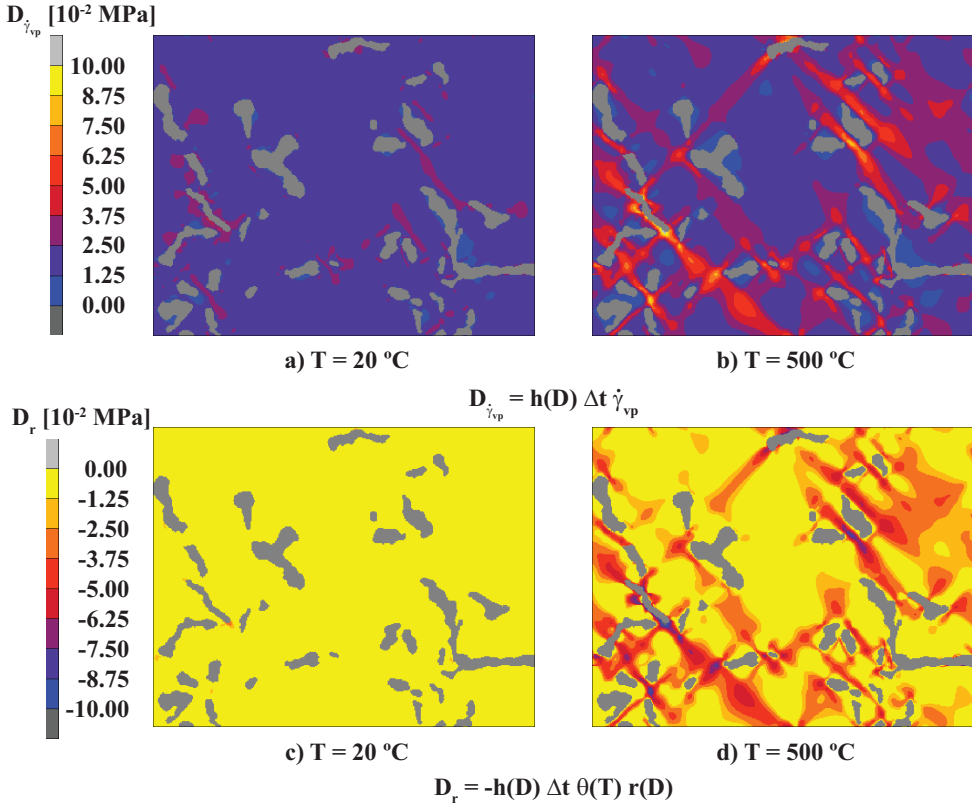


Figure 5.4: Uniaxial tensile test, contributions to the drag strength D from plastic deformation (top) and thermal recovery (bottom) at the end of macroscopic loading: left) at 20°C ; right) at 500°C .

The boundary conditions are prescribed such that an overall uniaxial stress state is reproduced (Appendix B). Two load steps are considered: *i*) pre-load: a macroscopic strain of 1 % is prescribed on the RVE in the horizontal direction (see Figure 5.1) in 20 seconds, i.e. at a strain rate of $5 \cdot 10^{-4} \text{ s}^{-1}$; *ii*) stress relaxation: once the prescribed macroscopic strain is reached, the RVE is held in its deformed state for 2 hours allowing the stress to relax.

The results are presented in Figure 5.7, where the stress relaxation is defined as the drop in stress between the peak stress reached at the end of the pre-load $\tau_{t=20s}$, and the stress at the end of the relaxation period $\tau_{t=2h}$:

$$Sr = \left[\frac{\tau_{t=2h} - \tau_{t=20s}}{\tau_{t=20s}} \right] * 100\%. \quad (5.29)$$

Figure 5.7 gives a clear indication of the effect of the temperature on the time-dependent behaviour of CGI. Below 350°C , there is a negligible difference in the

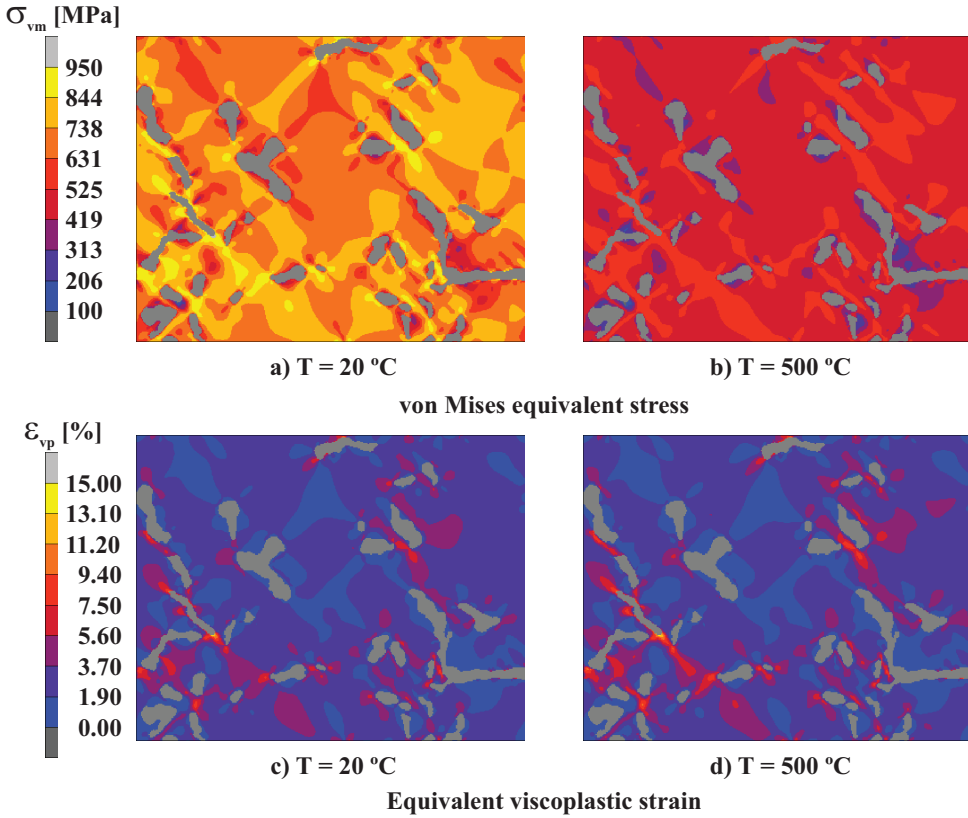


Figure 5.5: Uniaxial tensile test, equivalent von Mises stresses (top) and equivalent viscoplastic strain (bottom) in the matrix phase at the end of macroscopic loading: a) and c) at 20 °C; b) and d) at 500 °C.

relaxation response of the material. From this point onwards, increasing the temperature leads to a sharp increase in the amount of stress relaxation.

The observed behaviour is driven by the elevated temperature response of the pearlitic matrix, captured by the model described in Section 5.2.3, and calibrated on the experimental data for pearlitic steel, as discussed in Chapter 4. Experiments indicated that pearlitic phases present a low sensitivity to temperature below 350 °C, while above this temperature, the resistance of the material to creep deteriorates drastically which explains the response observed in Figure 5.7.

In general terms, stress relaxation is driven by the time- and temperature-dependent plastic deformation of the material. As discussed in the previous section, the resistance to plastic deformation is described in the model by the drag strength. At lower temperatures, high stresses can exceed the drag strength and enable plastic deformation and hence stress relaxation. At higher temperatures, the stresses are lower yet, a higher stress relaxation is observed, which can be explained by the thermal

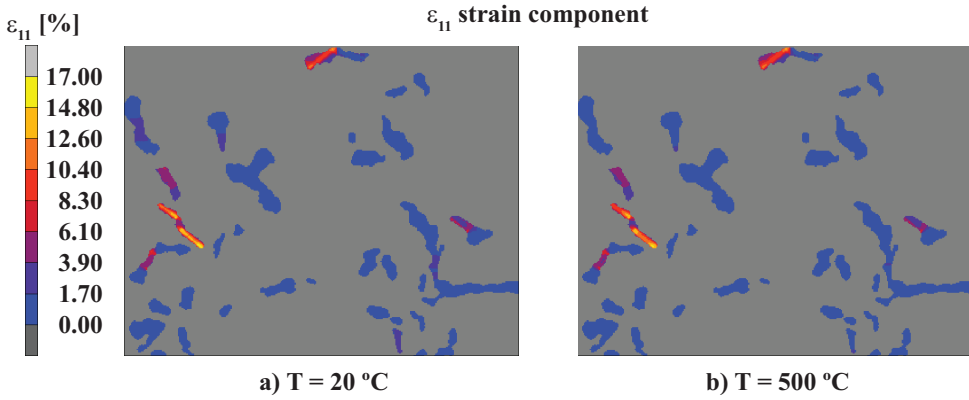


Figure 5.6: Uniaxial tensile test, ε_{11} strain component in the graphite particles: a) at 20 °C; b) at 500 °C.

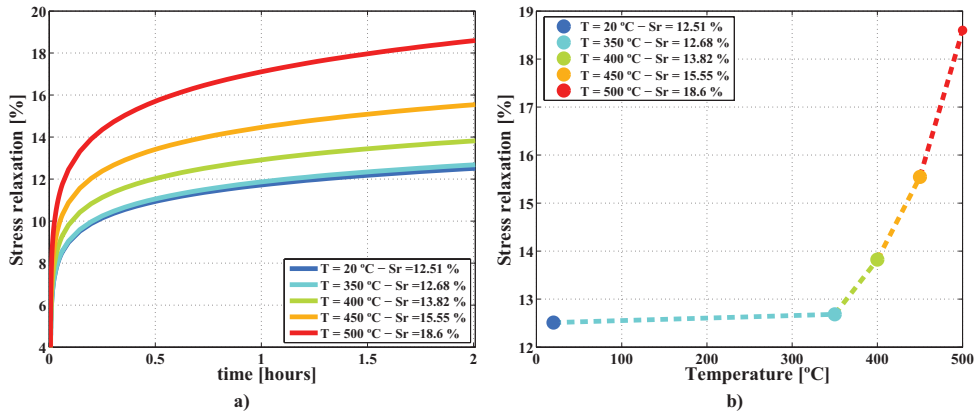


Figure 5.7: Stress relaxation of CGI as predicted by RVE simulations: a) stress relaxation percentage vs. time for the different temperatures; b) stress relaxation percentage as a function of temperature.

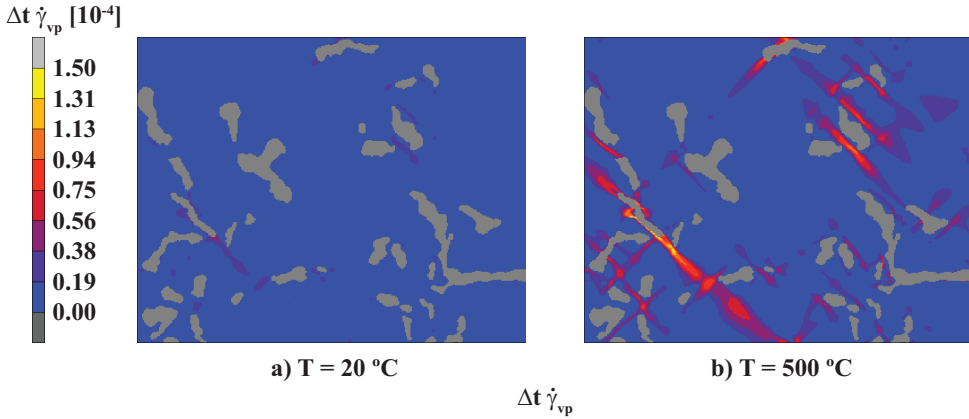


Figure 5.8: Stress relaxation test, incremental viscoplastic strain $\Delta t \dot{\gamma}_{vp}$ in the matrix phase at the end of stress relaxation: a) response at 20 °C; b) response at 500 °C.

recovery. As a consequence of a higher activation energy, thermal recovery becomes more pronounced at higher temperatures. It counteracts the strain hardening effect of the drag strength enabling plastic deformation. Hence, in spite of the lower stresses, a higher stress relaxation takes place at higher temperature.

To illustrate this situation, Figures 5.8 and 5.9 show the incremental viscoplastic strain $\Delta t \dot{\gamma}_{vp}$ and the contributions to D from the plastic deformation and thermal recovery in the matrix. Figure 5.8 reveals a marked difference in the matrix incremental viscoplastic strains $\Delta t \dot{\gamma}_{vp}$, at the end of stress relaxation at 20 °C and 500 °C. Moreover, the difference in $\Delta t \dot{\gamma}_{vp}$ can be traced back to the the drag strength and thermal recovery. The higher thermal recovery at 500 °C (Figure 5.9) induces a lower drag strength. This results in a higher amount of plastic deformation and hence more stress relaxation.

The combined effect of microstructural heterogeneity and temperature can be also appreciated in Figures 5.8 and 5.9. The presence of the graphite particles introduces stress concentrations in their neighbourhood in the microstructure. At 500 °C the contribution to the drag strength D from thermal recovery is twice as high as the contribution from plastic deformation. Therefore, over time the drag strength decreases resulting in higher plastic strain rates and the formation of strain percolation paths (Figure 5.8). It is expected that this triggers damage at the microstructural level.

5.4 Conclusions

The aim of this chapter was to investigate the elevated temperature mechanical behaviour of cast irons. For this purpose, a new microstructural based model for elevated temperature mechanical analyses of CGI has been developed. The model incorporates the time and temperature dependent response of the matrix and the

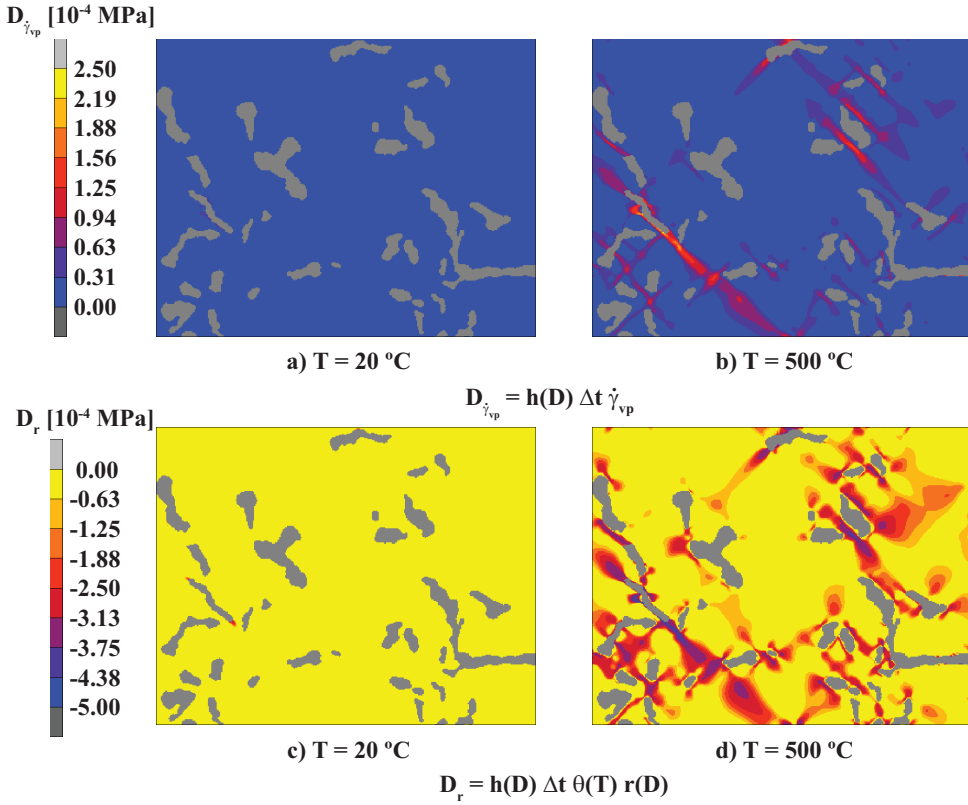


Figure 5.9: Stress relaxation test, contributions to the drag strength D from plastic deformation (top) and thermal recovery (bottom) at the end of stress relaxation: left) response at 20 °C; right) response at 500 °C.

morphology of the graphite inclusions along with the intrinsic mechanical anisotropy of graphite. The behaviour of the pearlitic matrix is modelled through the thermo-viscoplastic model introduced in Chapter 4 and implemented here in a finite element framework. To validate the representativeness of the material parameters identified on C75 pearlitic steels for the behaviour of the pearlitic matrix, micro-indentation tests have been performed on the pearlitic matrix of CGI as well as on a C75 pearlitic steel. The results, in terms of Young's modulus and hardness, revealed an adequate agreement between the two materials.

From the numerical results of the elevated temperature tests on CGI it can be concluded that:

- The effect of temperature on the mechanical response of CGI is dominant for temperatures above 350 °C. This is confirmed by the tensile tests as well as the stress relaxation tests. In the former, a sharp decrease in the hardening rate with temperature has been observed at the macroscopic level. In a similar

fashion, a fast increase in the resulting stress relaxation is perceived in the latter for temperatures exceeding 350 °C.

- For higher temperatures, the amount of thermal recovery overcomes the contribution of plastic deformation to hardening, leading to a reduction of the drag strength. This, directly influences either the hardening or the relaxation of the material at the local and global level.
- At lower temperatures, the effect of thermal recovery is negligible and the only driver for stress relaxation is dynamic recovery.
- At a microstructural level, the highly heterogeneous microstructure of cast irons leads to stress concentrations in the areas surrounding the graphite particles. As the temperature is increased, the combined effect of time, temperature and heterogeneity promotes local plastic deformation at the microstructural scale. This may accelerate the damage initiation and evolution, therefore reducing the time to failure of the material.

Conclusions and recommendations

The aim of this thesis was twofold. The first goal was to develop a cast iron microstructural model for elevated temperature mechanical and thermal analyses. The second, was to gain further insight into the micromechanical phenomena that drive the response of cast iron at temperatures up to 500 °C. These two objectives are tightly connected to each other because the development of such a model requires a deep understanding on how the microstructure drives the response of the material at the micro and macro level. For that reason, when input for the model was missing, either in terms of knowledge of the underlying micromechanics, material parameters or constitutive behaviour of the microconstituents, experiments were performed to provide the missing input.

6.1 Cast iron microstructural model

The models discussed in this thesis were developed within the framework of computational homogenization as proposed in [80]. A 3D unit cell model was considered to incorporate the inherent 3D nature of the graphite inclusions within cast iron. This unit cell was aimed to study the mechanical, thermal and thermo-mechanical behaviour of Lamellar Graphite Iron (FGI). The idealized unit cell model captured the main morphological features of FGI, such as the sharpness and the 3D connectivity of the graphite particles, which are critical for the thermo-mechanical properties of the FGI.

The higher morphological heterogeneity of Compacted Graphite Iron (CGI) as compared to FGI, implied that a unit cell model as developed for FGI would not be sufficiently representative of the material microstructure. For that reason, a 2D Representative Volume Element (RVE), based on CGI micrographs was introduced. The geometry of the RVE was obtained by transforming every pixel of the micrograph into a finite element. The different phases were distinguished based on the grey scale level of each pixel. This methodology allowed to capture a higher level of microstructural detail and include a larger part of the material microstructure, yielding a more representative microstructural model. Moreover, the model computational cost are considerably reduced for a 2D model, making it possible to account

for more complex constitutive behaviours at the micro level.

The constitutive behaviour of the different phases included mechanical (matrix) as well as thermal non-linearities (matrix and graphite). The mechanical and thermal anisotropy of graphite, induced by its crystallographic anisotropy, were also incorporated in the model.

The matrix behaviour was initially modelled using an elasto-plastic constitutive law, where the flow stress evolution of the ferrite/pearlite mixture was determined based on the work by Allain and Bouaziz [5]. As the next step, the matrix behaviour was modelled using a thermo-viscoplastic description developed *ad hoc* for pearlite and pearlitic steels. This was included to incorporate the time and temperature dependency of the cast iron RVE. The thermo-viscoplastic description is an extension of the one proposed by Freed and Walker [46] to finite strains. Furthermore, a yield surface was introduced to account for the marked yield point present in pearlite and perlitic steels, and the thermal function was modified based on experimental observations.

6.2 Summary of the results

The main conclusions from these investigations can be summarized as follows:

On the mechanics of the graphite particles. An experimental and numerical approach was used to investigate the mechanical anisotropy of the vermicular graphite particles found in CGI. The main conclusions of this study are:

- Experimental evidence was obtained confirming the mechanical anisotropy of vermicular graphite particles in cast irons.
- The strains in the graphite particles computed using the 2D CGI microstructural models show a qualitatively good agreement with the experimentally measured strains. This provides a solid confirmation of the hypothesis on graphite is mechanical anisotropy in vermicular graphite particles in cast irons.
- The nonlinearity of the strains in the graphite particles, as a function of the global applied strain, is the result of the increased plastic yielding of the matrix in the areas surrounding the graphite particles.

On the temperature dependent mechanics of pearlitic steels and pearlite. The new experimental evidence obtained from tensile and creep tests provides clear evidence of the influence of temperature and load on the mechanical response of pearlitic steels. A finite strain thermo-viscoplastic model for the elevated temperature behaviour of pearlitic steels was proposed. The ability of the model to predict the mechanical behaviour of pearlitic steels was illustrated, showing a good agreement with the experimental data. From the analyses of the obtained experimental data and the numerical examples, it can be concluded that:

- The influence of temperature on the mechanical behaviour of pearlitic steels is negligible below 350–400 °C. For higher temperatures, the mechanical properties depend strongly on temperature. The material's resistance to deformation decreases rapidly for increasing temperatures. This effect is observed in the drop of the flow stress and the sharp increase in the creep strain rate. As a consequence, the creep resistance of the material deteriorates dramatically above the 350 – 400 °C temperature threshold and for certain stress levels failure can take place in a matter of hours.
- These results have important implications for the use of pearlite or pearlitic steels in engineering applications in which the material is subjected to temperatures in excess of 350 – 400 °C. At this temperature level, the material no longer exhibits its well known room temperature structural integrity and creep resistance. Therefore, certain combinations of temperature, load and holding time can considerably accelerate the failure of the material and related engineering components.

On lamellar graphite iron. A 3D unit cell model was employed to examine the mechanical, thermal and thermo-mechanical response of lamellar graphite irons. Although the focus was on lamellar graphite irons, the conclusions apply to other composite materials with anisotropic phases and a 3D interconnected microstructure. The primary findings of this study are:

- Anisotropy plays a key role in the mechanical, thermal and thermo-mechanical response of heterogeneous materials at the micro and macro scale. Neglecting the anisotropy, by replacing an anisotropic constituent with an isotropic one yields an incorrect estimation of the micro-level deformation and temperature fields. This leads to an erroneous prediction of the macroscopic material response. In addition, mechanisms that are strongly related to the local response of the material, e.g. damage, cannot be predicted reliably.
- The interface condition between the microstructural phases (fixed or loose) has an important influence on the tensile response of the material, while it has virtually no influence on the response in compression. In the thermo-mechanical analysis, for the thermo-mechanical conditions considered here, the interface has a limited effect on the overall thermal expansion of heterogeneous materials with a 3D interconnected microstructure.

On compacted graphite irons. A 2D RVE type microstructural model was developed to investigate the mechanical response of compacted graphite for temperatures up to 500 °C. The model incorporated the morphology of the graphite inclusions together with the mechanical anisotropy of the graphite, and the time and temperature dependent behaviour of the pearlitic matrix. The most relevant conclusions can be summarized as follows:

- The mechanical anisotropy of graphite appears to have an insignificant effect at the macroscopic level, where the response of CGI is dominated by the

pearlitic matrix. However, at the microscopic level the influence of graphite's mechanical anisotropy cannot be disregarded. The location and intensity of critical spots, in terms of stress and strain concentrations, are determined not only by the morphology of the graphite particles but also by their mechanical anisotropy. As a consequence, neglecting graphite's mechanical anisotropy can lead to wrong conclusions regarding the location of the damage initiation sites as well as the damage propagation path. Furthermore, as the temperature is increased, the combined effect of time, temperature and cast iron microstructural heterogeneity enhances plastic deformation and damage evolution hereby reducing the time to failure of the material.

- The effect of temperature on the mechanical response of CGI becomes relevant for temperatures above 350 °C. This is observed on both the tensile tests and the stress relaxation tests. In the former, a fast drop in the hardening rate with temperature was observed at the macroscopic level. In a similar fashion, a fast increase in stress relaxation was perceived in the latter for temperatures exceeding 350 °C.
- For higher temperatures, the amount of thermal recovery overcomes the contribution of plastic deformation to hardening, leading to a reduction on the drag strength. This, directly influences the hardening and the relaxation of the material at the local and global level. At lower temperatures, the effect of thermal recovery is negligible and the sole driver for stress relaxation is dynamic recovery.

To summarize, in this thesis the mechanical and thermo-mechanical behaviour of cast irons have been investigated. Throughout this work the aim was to understand the underlying micromechanics of cast irons as a first step to predict its response. This led to new findings on the constitutive behaviour of two of cast iron's microconstituents, i.e. the graphite and the pearlitic matrix. The mechanical anisotropy of vermicular graphite particles in cast irons was confirmed, and the elevated temperature mechanical response of pearlite and pearlitic steels was resolved. Furthermore, the temperature threshold (i.e. 350 – 400 °C) upon which the sensitivity of the mechanical properties of pearlite to temperature is dramatically increased was also identified. Finally, it was shown how the thermo-mechanical response of cast iron, at the micro and macro level, is determined by its high microstructural heterogeneity, the anisotropy of the graphite particles and time and temperature dependent behaviour of pearlite.

6.3 Recommendations for future developments

In this thesis, a numerical-experimental approach was followed to investigate the response of cast irons under different mechanical and thermal conditions. Besides the inherent benefits of this approach concerning the possibility to explore the material response at both the micro and macro levels, the predictive capability of the model was determined by the fidelity of the incorporated the underlying microstructural physics. In this regard, the knowledge on the morphological features of the

different microstructural components, their constitutive behaviour and the interaction among them is of utmost importance. Therefore, any further endeavours on microstructural modelling of cast irons should first seek to gather a solid knowledge of the microstructural response of the material. If possible, microstructural scale experiments should be performed to provide material input and validated constitutive hypotheses. Such an approach was successfully used here, leading to new insights into the constitutive behaviour of graphite particles and pearlitic matrix.

From a modelling perspective, to perform thermo-mechanical fatigue simulations of cast irons, the pearlite thermo-viscoplastic model needs to be extended to include the effect of the change in material parameters due to temperature variations, as present during thermo-mechanical cycling. This requires to incorporate the contribution of the related temperature rate terms into the constitutive equations of the rate form stress-strain relation and the internal variables, e.g. as discussed in [20, 92]. In addition, the extension of the pearlite thermo-viscoplastic model to the non-isothermal regime requires non-isothermal experimental data, which is in general difficult to obtain.

Another subject that needs to be further explored is microstructural damage in cast irons under TMF conditions. Several studies in the literature point to the matrix/graphite interface as a preferential site for damage initiation [33, 35, 38, 41, 51, 62, 73, 87, 111]. A crack then propagates along the matrix/graphite interface or by graphite internal cracking. To incorporate crack initiation and propagation phenomena into the model, an in depth study of the physics of the complex matrix/graphite interface is required. This investigation should not only focus on the interface behaviour under static room temperature conditions, but it should also aim to understand and characterize the interface behaviour under TMF conditions. This requires an insight into the impact of cyclic thermo-mechanical loads and environmental effects (e.g. oxidation and decarburization) on the interface response. Next, an interface model needs to be developed to include the interface response under TMF conditions into the cast iron RVE. One possibility is to use a cohesive zone modelling approach coupled with environmental effects as discussed in [105].

After the initial stage in which damage propagates preferentially through the interface, cracks will develop within the matrix linking the graphite inclusions across the crack path [33, 35, 38, 41, 51, 62, 73, 87, 111]. To account for the fracture development through the matrix, a non-local damage model and crack evolution approach as discussed in [75, 93, 107, 141] could be implemented. Furthermore, damage could be further accelerated due to microstructural evolution effects such as oxidation, decarburization and pearlite decomposition. Consequently, this can be incorporated in a later stage.

The inherent 3D nature of the graphite particles in cast iron was considered in this thesis via the unit cell model developed in Chapter 2. Although the model captures the main morphological features of FGI, it cannot be used for CGI. After all, the morphology of the graphite particles varies between nodular, lamellar and vermicular. The larger microstructural heterogeneity found in CGI, makes it challenging to develop a unit cell that is representative for its microstructure. To capture the complex 3D morphology of CGI, a computer tomography-based modelling approach can be used [147, 148]. This technique could also be applied to create a 3D FGI

model and evaluate if the unit cell model introduced here is sufficiently representative of the random FGI microstructure. The main drawback of this method is high computational cost involved due to the large size of the 3D FEM models required. Finally, the high microstructural complexity of cast irons (e.g. morphology of the graphite inclusions, non-linear mechanical and thermal response of the different phases, anisotropy of the graphite particles, complex matrix/graphite interface behaviour, etc.) together with the complex load conditions present in TMF yield computationally intractable models. As a consequence, performing TMF life prediction simulations for cast irons will demand large computational resources for long periods of time. A possibility to reduce the high computational cost, is to implement model order reduction techniques in space and time. The former should be used to compute the large non-linear 3D microstructural cast iron models. The latter on the other hand, is aimed at performing efficient time integration of the fatigue cyclic loading and was preliminary investigated within the context of this project, within a 1D framework, but is outside of the scope of this thesis [13].



Tensor and vector operation notation

In this thesis Cartesian tensors and associated tensor products are used, using a Cartesian vector basis $\vec{e}_1, \vec{e}_2, \vec{e}_3$. The Einstein summation rule for repeated indices is used. Adopted notations are summarized below:

- Quantities:
 - Scalars: α, a, A ,
 - Vectors: $\vec{a} = a_i \vec{e}_i$,
 - Second order tensors: $\mathbf{A} = A_{ij} \vec{e}_i \otimes \vec{e}_j$,
 - Second order identity tensor: $\mathbf{I} = \delta_{ij} \vec{e}_i \otimes \vec{e}_j$,
 - Fourth order tensors: ${}^4\mathbb{A} = A_{ijkl} \vec{e}_i \otimes \vec{e}_j \otimes \vec{e}_k \otimes \vec{e}_l$,
 - Fourth order identity tensor: ${}^4\mathbb{I} = \delta_{il} \delta_{jk} \vec{e}_i \otimes \vec{e}_j \otimes \vec{e}_k \otimes \vec{e}_l$,
 - Right transposed of the fourth order identity tensor: ${}^4\mathbb{I}^{RT} = \delta_{ik} \delta_{jl} \vec{e}_i \otimes \vec{e}_j \otimes \vec{e}_k \otimes \vec{e}_l$.
- Operations:
 - Scalar multiplication: $c = ab, \vec{c} = a\vec{b}, \mathbf{C} = a\mathbf{B}$,
 - Dyadic product: $\mathbf{C} = \vec{a} \otimes \vec{b} = a_i b_j \vec{e}_i \otimes \vec{e}_j$,
 - Inner product: $c = \vec{a} \cdot \vec{b} = a_i b_j, \mathbf{C} = \mathbf{A} \cdot \mathbf{B} = A_{ij} B_{jk} \vec{e}_i \otimes \vec{e}_k$,
 - Double inner product: $c = \mathbf{A} : \mathbf{B} = A_{ij} B_{ji}, \mathbf{C} = \mathbb{A} : \mathbf{B} = A_{ijkl} B_{lk} \vec{e}_i \otimes \vec{e}_j$,
 - Transpose: $\mathbf{A}^T = A_{ji} \vec{e}_i \otimes \vec{e}_j$,
 - Left transpose: $\mathbb{A}^{LT} = A_{jikl} \vec{e}_i \otimes \vec{e}_j \otimes \vec{e}_k \otimes \vec{e}_l$,
 - Right transpose: $\mathbb{A}^{RT} = A_{ijlk} \vec{e}_i \otimes \vec{e}_j \otimes \vec{e}_k \otimes \vec{e}_l$,
 - Gradient operator: $\vec{\nabla} = \vec{e}_i \frac{\partial}{\partial x_i}$

2D computational homogenization

Within the framework of the computational homogenization adopted for the microstructural modelling [80], the microstructural displacement fields $\vec{u}_m(\vec{x})$ in a given point \vec{x}_m in the current configuration can be described through a macroscopic contribution (resulting from the macroscopic deformation gradient tensor \mathbf{F}_M) and a microstructural fluctuation field $\vec{u}_f(\vec{x})$ that represents the local variations with respect to the average macroscopic fields. Expressing the displacement $\vec{u}_m(\vec{x})$ of an arbitrary chosen point within the microscopic volume relative to some chosen point k yields

$$\vec{u}_m(\vec{x}_m) = \vec{u}^k(\vec{x}_k) + (\mathbf{F}_M - \mathbf{I}) \cdot (\vec{X}_m - \vec{X}^k) + \vec{u}_f(\vec{x}_m), \quad (\text{B.1})$$

In the above expressions, the subscripts m , M and f refer to the *micro* and *macro* scale quantities and the microscopic fluctuation field, respectively. In equation (B.1) \vec{X} denotes the position vector in the reference configuration.

In computational homogenization framework, the macro-to-micro scale transition is achieved by imposing that the macroscopic deformation gradient tensor should be equal to the volume average of its microscopic counterpart, i.e.:

$$\mathbf{F}_M = \frac{1}{V_0} \int_{V_0} \mathbf{F}_m dV_0, \quad (\text{B.2})$$

From the expression of the microscopic displacement field (B.1), the microscopic deformation gradient tensor can be obtained and introduced in equation (B.2) leading to the following boundary integral:

$$\int_{\Gamma_0} \vec{u}_f \otimes \vec{n}_0 d\Gamma_0 = \mathbf{0}, \quad (\text{B.3})$$

where \vec{n}_0 is the normal to the RVE boundary in the reference configuration.

This condition can be fulfilled by means of different boundary conditions such as uniform displacement, uniform traction and periodic boundary conditions. In this work, periodic boundary conditions are used since they yield the better approximation to the apparent macroscopic properties [80]. In the case of a 2D RVE, as used

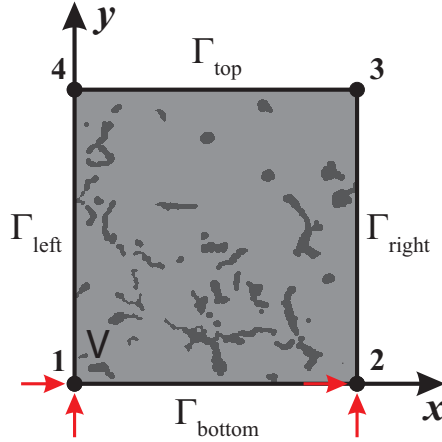


Figure B.1: Schematic representation of a 2D unit cell showing the boundary conditions with prescribed displacements at corner nodes for a 2D macroscopic uniaxial tensile stress condition.

in this work (Figure B.1), the periodic boundary conditions lead to the following displacement tyings [80]:

$$\vec{u}^+ = \vec{u}^- + (\mathbf{F}_M - \mathbf{I}) \cdot (\vec{X}^+ - \vec{X}^-), \quad (\text{B.4})$$

where superscript “+” refers to the top and right part of the boundary, while “-” refers to the bottom and left part (see Figure B.1).

Furthermore, the macroscopic gradient tensor \mathbf{F}_M is prescribed through the RVE corner nodes 1,2 and 4 in the form of displacements as:

$$\vec{u}_p = (\mathbf{F}_M - \mathbf{I}) \cdot \vec{X}_p, \quad p = 1, 2, 4 \quad (\text{B.5})$$

where \vec{u}_p are the prescribed microscopic displacements and \vec{X}_p are the position vectors of the respective corner nodes.

The micro-to-macro scale transition is based on the Hill-Mandel principle of macro-homogeneity. Based on this principle it can be shown that the micro-to-macro transitions can be expressed as [80]:

$$\mathbf{P}_M = \frac{1}{V_0} \int_{V_0} \mathbf{P}_m dV_0 = \frac{1}{V_0} \sum_{p=1,2,4} \vec{f}_p \otimes \vec{X}_p, \quad (\text{B.6})$$

where \mathbf{P} represents the first Piola-Kirchhoff stress tensor and \vec{f}_p are the reaction forces at the prescribed corner nodes. To derive the second equation in (B.7), the equilibrium condition on the RVE in combination with the divergence theorem and the periodic boundary conditions has been used, see [80] for the details.

From (B.7) it is clear that to obtain a homogenized uniaxial stress state in the horizontal direction, for the RVE illustrated in Figure B.1, the following boundary

conditions can be applied on the corner nodes:

$$\vec{u}_1 = \vec{0}, \quad u_2^x = u^*, \quad u_2^y = 0, \quad \vec{f}_4 = \vec{0}, \quad (\text{B.7})$$

with u^* the prescribed horizontal displacement. All the other nodes on the RVE boundary are linked through the periodic boundary conditions.

3D thermo-mechanical computational homogenization

C.1 Macro-to-micro scale transition

Within the framework of thermo-mechanical computational homogenization [80, 103, 104], the microstructural displacement and temperature fields at a given point \vec{x}_m in the current configuration can be described through a macroscopic contribution and a microstructural fluctuation field that represents the local variations with respect to the average fields. If the displacements $\vec{u}_m(\vec{x})$ and the temperature $\theta_m(\vec{x})$ are expressed with respect to the values of an arbitrary chosen point k within the microscopic volume, it yields [104]:

$$\vec{u}_m(\vec{x}) = \vec{u}^k(\vec{x}) + (\mathbf{F}_M - \mathbf{I}) \cdot (\vec{X} - \vec{X}^k) + \vec{u}_f(\vec{x}), \quad (\text{C.1})$$

$$\theta_m(\vec{x}) = \theta_m^k + (\vec{\nabla}_M \theta_M) \cdot (\vec{x} - \vec{x}^k) + \theta_f(\vec{x}). \quad (\text{C.2})$$

In the above expressions, the subscripts m , M and f refer to the *micro* and *macro* scale quantities and the microscopic fluctuation fields respectively. In equation (C.1) \vec{X} denotes the position vector in the reference configuration and \mathbf{F}_M is the macroscopic deformation gradient tensor. In the temperature equation (C.2), a formulation based on the current configuration is used, as discussed in [104].

In the first order computational homogenization, the macro-to-micro scale transition is achieved by imposing that the macroscopic gradients of the displacement and temperature fields should be equal to the volume average of their corresponding microscopic counterparts, i.e.:

$$\mathbf{F}_M = \frac{1}{V_0} \int_{V_0} \mathbf{F}_m dV_0, \quad (\text{C.3})$$

$$\vec{\nabla}_M \theta_M = \frac{1}{V} \int_V \vec{\nabla}_m \theta_m dV. \quad (\text{C.4})$$

From the expressions of the microscopic displacement (C.1) and temperature (C.2) fields, the microscopic deformation gradient tensor and the temperature gradient can

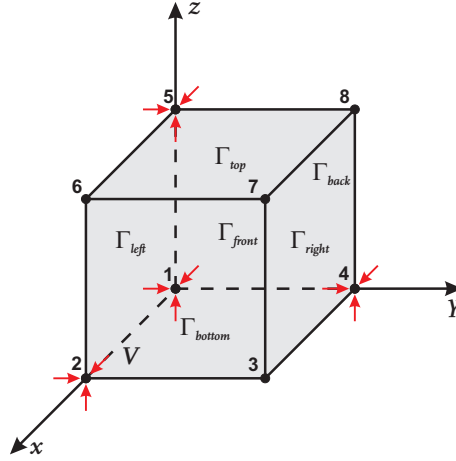


Figure C.1: Schematic representation of the 3D unit cell showing prescribed corner nodes.

be obtained and introduced in equations (C.3) and (C.4) leading to the following boundary integrals:

$$\int_{\Gamma_0} \bar{\mathbf{u}}_f \otimes \bar{\mathbf{n}}_0 d\Gamma_0 = 0, \quad (\text{C.5})$$

$$\int_{\Gamma} \theta_f \bar{\mathbf{n}} d\Gamma = 0. \quad (\text{C.6})$$

where $\bar{\mathbf{n}}_0$ and $\bar{\mathbf{n}}$ are the normals to the RVE boundary in the reference and current configurations respectively.

Equations (C.5) and (C.6) imply that the volume averages of the microscopic fluctuation fields need to vanish on the boundary of the micro-scale domain. This condition can be fulfilled by means of different boundary conditions such as uniform displacement, uniform traction and periodic boundary conditions. In this paper, periodic boundary conditions are used since they yield the best approximation to the apparent macroscopic properties [80]. In the case of the 3D unit cell used in this work (Figure C.1) the periodic boundary conditions lead to the following displacement and temperature tyings [104]:

$$\bar{\mathbf{u}}^+ = \bar{\mathbf{u}}^- + (\mathbf{F}_M - \mathbf{I}) \cdot (\bar{\mathbf{X}}^+ - \bar{\mathbf{X}}^-), \quad (\text{C.7})$$

$$\theta^+ = \theta^- + \bar{\nabla}_M \theta_M \cdot (\bar{\mathbf{x}}^+ - \bar{\mathbf{x}}^-), \quad (\text{C.8})$$

with superscript “+” referring to top, right and front parts of the boundary, while “-” refers to bottom, left and back parts (see Figure C.1).

The temperature distribution at the micro level is results from the thermal equilibrium of the unit cell under the prescribed boundary conditions using the temperature dependent conductivities of the different phases. An additional constraint is required to determine the reference temperature θ_m^k and to obtain a unique temperature profile at the micro level, see [103]. This constraint, which enforces the consistency

of the stored heat at the macro and micro levels, is known as the thermal energy consistency condition and is expressed as:

$$(\rho c_V)_M \theta_M = \frac{1}{V} \int_V (\rho c_V)_m \theta_m dV. \quad (\text{C.9})$$

In this equation, $(\rho c_V)_M$ is the macroscopic heat storage, which is obtained as the volume average of its microscopic counterpart:

$$(\rho c_V)_M = \frac{1}{V} \int_V (\rho c_V)_m dV, \quad (\text{C.10})$$

where ρ_m and c_{V_m} are the microscopic density and heat capacity, both dependent on the different microconstituents.

C.2 Micro-to-macro scale transition

The micro-to-macro scale transition is based on the Hill-Mandel principle of macro-homogeneity for the mechanical field and the conservation of thermal energy for the temperature field. Based on these it can be shown that the micro-to-macro transitions can be expressed as [104]:

$$\mathbf{P}_M = \frac{1}{V_0} \int_{V_0} \mathbf{P}_m dV_0, \quad (\text{C.11})$$

where \mathbf{P} refers to the First Piola-Kirchhoff stress tensor, and

$$\vec{q}_M = \frac{1}{V} \int_V \vec{q}_m dV \quad (\text{C.12})$$

where \vec{q} refers to the heat flux.

Furthermore, from the homogenized heat flux \vec{q}_M , the macroscopic thermal conductivity is determined as $\vec{q}_M = \mathbf{K}_M \cdot \vec{\nabla}_M \theta_M$. Note that for isotropic material $\mathbf{K}_M = K_M \cdot \mathbf{I}$, where K_M is the macroscopic thermal conductivity.



Rule of mixture and Turner's model

The expressions for rule of mixtures and Turner's model are:

- Rule of mixtures

$$\alpha_c = \alpha_m V_m + \alpha_g V_g, \quad (\text{D.1})$$

- Turner's model

$$\alpha_c = \frac{\alpha_m K_m V_m + \alpha_g K_g V_g}{K_m V_m + K_g V_g}. \quad (\text{D.2})$$

In these expressions, the subscript m refers to the matrix and the subscript g refers to graphite. V_m and V_g are the matrix and graphite volume fractions, α_m and α_g are the matrix and graphite CTEs and K_m and K_g are the matrix and graphite bulk moduli.



CTE and elastic mismatch study

In heterogeneous materials, such as cast iron, the mismatch between the phases in terms of elastic properties and CTE plays a crucial role in the resulting overall and local thermal expansion. Here, this issue is discussed in more detail. To this aim, two analyses were carried out to uncouple the effects of the elastic mismatch and the CTE mismatch. To make the interpretation of the results more transparent, the matrix and graphite are both assumed linear elastic and graphite's anisotropy is not taken into account.

In the CTE mismatch study two situations are compared: constant CTE mismatch and a variable CTE mismatch depending on temperature. In the first case, the CTEs of the matrix and the graphite are temperature dependent but the difference is kept constant with increasing temperature (Figure E.1.a top). In the second case, the same temperature dependent matrix CTE is used, while graphite's CTE is taken temperature independent (Figure E.1.a top), leading to a CTE mismatch that increases with temperature.

In both cases the same temperature independent bulk moduli were used for both phases (Figure E.1.a bottom), i.e. the effect of the elastic mismatch is excluded. Therefore, the composite CTE can be straightforwardly determined by the rule of mixtures (ROM). Then, at any given temperature the composite CTE will be equal to the weighted sum of the phases CTEs at that temperature.

The results of the CTE mismatch study are presented in Figure E.1.b. In the example presented here, the constant CTE mismatch model yields a higher macroscopic CTE, since at all temperatures the CTE of the graphite is higher than the one used for the temperature dependent CTE mismatch.

For the elastic mismatch study, a constant CTE mismatch is considered (Figure E.2.a top). For the elastic properties, first a constant mismatch is considered, by assuming that both matrix and graphite bulk moduli are temperature independent (Figure E.2.a top). For the second model, a temperature dependent matrix bulk modulus was used while the graphite bulk modulus was kept constant. This combination leads to an elastic mismatch that increases with temperature (Figure E.2.a bottom).

In Figure E.2.b the macroscopic CTEs based on the constant and variable elastic

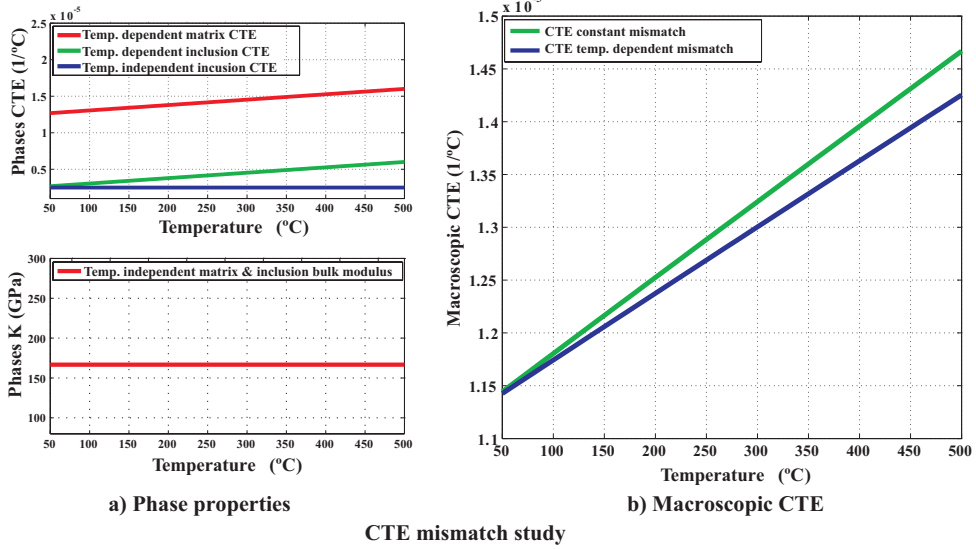


Figure E.1: Study of the influence of a microstructural CTE mismatch on the overall CTE: a) Micro-scale CTEs and bulk moduli; b) Estimated macroscopic CTE.

mismatches are compared. As the elastic mismatch is increased, the macroscopic CTE is significantly reduced. Moreover, the temperature dependent bulk modulus of the matrix for the variable elastic mismatch model leads to a non-linear macroscopic composite CTE (Figure E.2.b). This non-linear behaviour is not observed if only a CTE mismatch is present in the material (Figure E.1.b).

It is obvious that for cast iron, the impact on the overall response of an elastic mismatch is stronger than the impact of a CTE mismatch. As the bulk modulus mismatch increases with temperature, the macroscopic CTE drops fast. The elastic mismatch study demonstrates that the observed non-linear CTE behaviour of cast irons (Figure 2.10) is the result of the temperature dependent elastic mismatch, which in the considered case is due to the temperature dependent bulk modulus of the matrix.

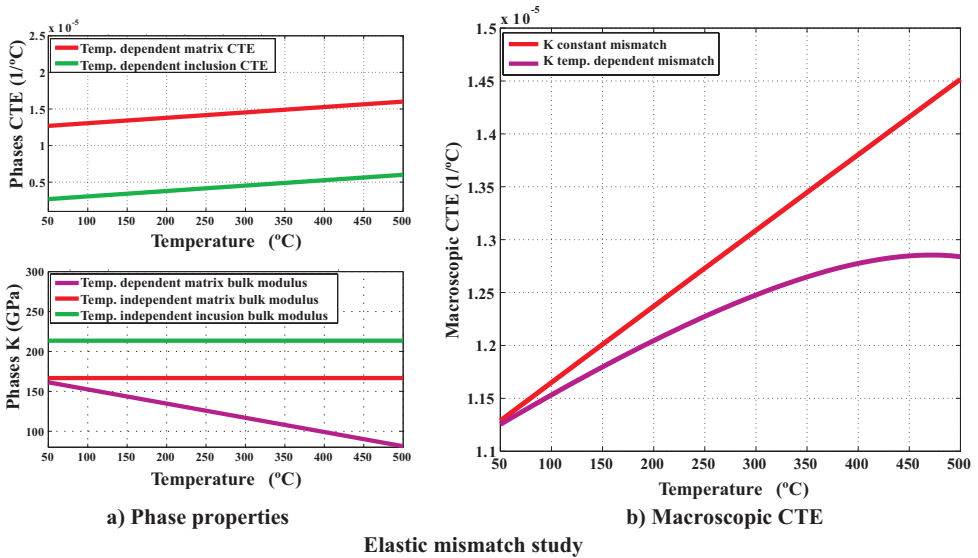


Figure E.2: Study of the influence of a microstructural elastic mismatch on the overall CTE: a) Micro-scale CTEs and bulk moduli; b) Estimated macroscopic CTE.



Thermo-viscoplastic model Jacobian terms and derivatives

In the solution of the (4.58), the Jacobian terms given are required. These can be determined by taking the partial derivatives of the residuals \mathbf{r}_τ and r_D with respect to the unknowns τ and D . This yields the following expressions:

$$\left. \frac{\partial \mathbf{r}_\tau}{\partial \tau} \right|_i = {}^4\mathbb{I} + \Delta t \theta(T) {}^4\mathbb{H}^i : \left[Z(\varphi^i, D^i) \left. \frac{\partial \mathbf{N}}{\partial \tau} \right|_i + \mathbf{N}^i \otimes \left. \frac{\partial Z(\varphi, D)}{\partial \tau} \right|_i \right], \quad (\text{F.1})$$

$$\left. \frac{\partial \mathbf{r}_\tau}{\partial D} \right|_i = \Delta t \theta(T) \left. \frac{\partial Z(\varphi, D)}{\partial D} \right|_i {}^4\mathbb{H}^i : \mathbf{N}^i, \quad (\text{F.2})$$

$$\left. \frac{\partial r_D}{\partial \tau} \right|_i = -\Delta t \theta(T) h(D^i) \left. \frac{\partial Z(\varphi, D)}{\partial \tau} \right|_i \quad (\text{F.3})$$

and

$$\begin{aligned} \left. \frac{\partial r_D}{\partial D} \right|_i = & 1 - \Delta t \theta(T) \left\{ h(D^i) \left[\left. \frac{\partial Z(\varphi, D)}{\partial D} \right|_i - \left. \frac{dr(D)}{dD} \right|_i \right] + \right. \\ & \left. \left. \left. \frac{dh(D)}{dD} \right|_i [Z(\varphi^i, D^i) - r(D^i)] \right\} \end{aligned} \quad (\text{F.4})$$

Furthermore the required derivatives are:

$$\left. \frac{\partial Z(\varphi, D)}{\partial \tau} \right|_i = \frac{nZ(\varphi^i, D^i)}{D^i} \coth \left[\frac{\varphi^i}{D^i} \right] \mathbf{N}^i, \quad (\text{F.5})$$

$$\left. \frac{\partial Z(\varphi, D)}{\partial D} \right|_i = -\frac{nZ(\varphi^i, D^i)}{D^{i2}} \coth \left[\frac{\varphi^i}{D^i} \right] \varphi^i, \quad (\text{F.6})$$

$$\left. \frac{\partial \mathbf{N}}{\partial \tau} \right|_i = \frac{1}{\tau_{eq}} \left[\frac{3}{2} {}^4\mathbb{I} - \frac{1}{2} \mathbf{I} \otimes \mathbf{I} - \mathbf{N}^i \otimes \mathbf{N}^i \right], \quad (\text{F.7})$$

$$\left. \frac{dh(D)}{dD} \right|_i = \frac{m}{\delta C \varphi_D^i} [1 - \varphi_D^i \coth[\varphi_D^i]] h(D^i), \quad (\text{F.8})$$

$$\left. \frac{dr(D)}{dD} \right|_i = \frac{n}{\delta C} \coth[\varphi D^i] r(D^i), \quad (\text{F.9})$$



Thermo-viscoplastic model finite element implementation

In the absence of body forces, the momentum equation in its strong form can be written as:

$$\vec{\nabla} \cdot \boldsymbol{\sigma}(\vec{x}) = \vec{0}, \quad (\text{G.1})$$

where $\boldsymbol{\sigma}$ is the Cauchy stress tensor and $\vec{\nabla}$ denotes the gradient operator with respect to the current configuration.

The first step to derive the weak form of the momentum equation, is to write the weighted residual form of (G.1). This is done by taking the scalar product of (G.1) with a vector valued test function $\vec{w}(\vec{X}_0)$, which is a function of the position vector in the undeformed reference configuration, followed by an integration over the entire volume of the body Ω . This yields:

$$\int_{\Omega} \vec{w}(\vec{X}_0) \cdot (\vec{\nabla} \cdot \boldsymbol{\sigma}(\vec{x})) d\Omega = 0, \quad (\text{G.2})$$

which must be satisfied for all admissible test functions $\vec{w}(\vec{X}_0)$. By applying the chain rule and the divergence theorem to (G.2), the weak form of the momentum equation can be obtained, leading to:

$$\int_{\Omega} (\vec{\nabla} \vec{w}(\vec{X}_0))^T : \boldsymbol{\sigma}(\vec{x}) d\Omega = \int_{\Gamma} \vec{w}(\vec{X}_0) \cdot \vec{t}(\vec{x}) d\Gamma, \quad (\text{G.3})$$

where $\vec{t}(\vec{x}) = \vec{n}(\vec{x}) \cdot \boldsymbol{\sigma}(\vec{x})$ is the traction vector and $\vec{n}(\vec{x})$ is the normal to the external surface Γ of Ω .

Expression (G.3) represents the weak form in the current deformed configuration, which needs to be solved for the problem at hand. It is convenient to express the left hand side of (G.3) in terms of the reference configuration. To that end, the following relations are:

$$d\Omega = Jd\Omega_0, \quad J = \det \mathbf{F}, \quad (\text{G.4})$$

and,

$$\vec{\nabla} = \mathbf{F}^{-T} \cdot \vec{\nabla}_0. \quad (\text{G.5})$$

The latter expression relates the gradient operator in the current configuration to the one in the reference configuration via de deformation gradient tensor \mathbf{F} .

The weak form (G.3) is written in the reference configuration as:

$$\int_{\Omega_0} (\vec{\nabla}_0 \vec{w}(\vec{X}_0))^T : (\mathbf{F}^{-1}(\vec{x}) \cdot \boldsymbol{\sigma}(\vec{x})) J(\vec{x}) d\Omega_0 = \int_{\Gamma} \vec{w}(\vec{X}_0) \cdot \vec{t}(\vec{x}) d\Gamma. \quad (\text{G.6})$$

In addition, considering the relation between the Cauchy stress tensor and the Kirchhoff stress tensor, $\boldsymbol{\tau} = J\boldsymbol{\sigma}$, expression (G.6) can be expressed as:

$$\int_{\Omega_0} (\vec{\nabla}_0 \vec{w}(\vec{X}_0))^T : (\mathbf{F}^{-1}(\vec{x}) \cdot \boldsymbol{\tau}(\vec{x})) d\Omega_0 = \int_{\Gamma} \vec{w}(\vec{X}_0) \cdot \vec{t}(\vec{x}) d\Gamma. \quad (\text{G.7})$$

Now, considering the classical finite element discretization, the weak form (G.7) can be expressed on the discretized domain Ω_0^h . First, the unknown field of the position vectors in the current configuration $\vec{x}(\vec{X}_0, t)$ can be approximated by

$$\vec{x}^h(\vec{X}_0, t) = \mathbb{N}^T(\vec{X}_0) \vec{\underline{x}}(t), \quad (\text{G.8})$$

where $\mathbb{N}^T(\vec{X}_0)$ is the column containing the shape functions and $\vec{\underline{x}}(t)$ is the column of the nodal position vectors, both of length n equal to the total number of nodes. Furthermore, the test functions are discretized using the same shape functions $\mathbb{N}^T(\vec{X}_0)$ as used for the unknown field of the position vectors, i.e.

$$\vec{w}^h(\vec{X}_0) = \mathbb{N}^T(\vec{X}_0) \vec{\underline{w}}, \quad (\text{G.9})$$

where the column $\vec{\underline{w}}$ contains n nodal vectors \vec{w}_i . Then, the gradient of the test functions is given by:

$$\vec{\nabla}_0 \vec{w}^h(\vec{X}_0) = (\vec{\nabla}_0 \mathbb{N}(\vec{X}_0))^T \vec{\underline{w}}, \quad (\text{G.10})$$

and the column of the gradient of the shape functions $\vec{\nabla}_0 \mathbb{N}(\vec{X}_0)$ is defined as

$$\vec{\nabla}_0 \mathbb{N}(\vec{X}_0) = \left[\vec{\nabla}_0 N_1(\vec{X}_0) \quad \vec{\nabla}_0 N_2(\vec{X}_0) \quad \dots \quad \vec{\nabla}_0 N_n(\vec{X}_0) \right]^T. \quad (\text{G.11})$$

After introducing expression (G.10) into (G.7) the weak form can be written as

$$\int_{\Omega_0^h} \vec{\underline{w}}^T \vec{\nabla}_0 \mathbb{N}(\vec{X}_0) : (\mathbf{F}^{-1}(\vec{x}) \cdot \boldsymbol{\tau}(\vec{x})) d\Omega_0 = \int_{\Gamma^h} \mathbb{N}^T(\vec{X}_0) \vec{\underline{w}} \cdot \vec{t}(\vec{x}) d\Gamma. \quad (\text{G.12})$$

Furthermore, taking the column with nodal test function vectors (independent of \vec{X}_0) out of the integrals

$$\vec{\underline{w}}^T \cdot \left(\int_{\Omega_0^h} \vec{\nabla}_0 \mathbb{N}(\vec{X}_0) \cdot (\mathbf{F}^{-1}(\vec{x}) \cdot \boldsymbol{\tau}(\vec{x})) d\Omega_0 \right) = \vec{\underline{w}}^T \cdot \int_{\Gamma^h} \mathbb{N}(\vec{X}_0) \vec{t}(\vec{x}) d\Gamma. \quad (\text{G.13})$$

The weak form (G.7) must be satisfied for all test function columns \vec{w} , this implies that

$$\int_{\Omega_0^h} \vec{\nabla}_0 \mathbb{N}(\vec{X}_0) \cdot (\mathbf{F}^{-1}(\vec{x}) \cdot \boldsymbol{\tau}(\vec{x})) d\Omega_0 = \int_{\Gamma^h} \mathbb{N}(\vec{X}_0) \vec{t}(\vec{x}) d\Gamma, \quad (\text{G.14})$$

which is a set of nonlinear algebraic equations, where the unknowns are the nodal positions $\vec{\underline{x}}(t)$.

G.1 Linearization

The system of equations given in (G.14), can be expressed as

$$\vec{\tilde{r}} = \vec{\tilde{f}}^{int} - \vec{\tilde{f}}^{ext} = \vec{0}, \quad (\text{G.15})$$

where the columns of the internal forces $\vec{\tilde{f}}^{int}$ and the external forces $\vec{\tilde{f}}^{ext}$ are given by

$$\vec{\tilde{f}}^{int}(\vec{\tilde{x}}) = \int_{\Omega_0^h} \vec{\nabla}_0 \mathbb{N}(\vec{X}_0) \cdot (\mathbf{F}^{-1}(\vec{x}) \cdot \boldsymbol{\tau}(\vec{x})) d\Omega_0, \quad (\text{G.16a})$$

$$\vec{\tilde{f}}^{ext}(\vec{\tilde{x}}) = \int_{\Gamma^h} \mathbb{N}(\vec{X}_0) \cdot \vec{t}(\vec{x}) d\Gamma, \quad (\text{G.16b})$$

and $\vec{\tilde{r}}$ represents the unbalanced residual between the internal and external forces. The non-linear system of equations is solved using the Newton-Raphson method. If $\vec{\tilde{x}}^i$ is an approximate solution obtained at iteration i , then at the next iteration $i + 1$ the approximate solution can be expressed as $\vec{\tilde{x}}^{i+1} = \vec{\tilde{x}}^i + \delta\vec{\tilde{x}}$, where $\delta\vec{\tilde{x}}$ is the iterative correction. The residual at iteration $i + 1$ is:

$$\vec{\tilde{r}}(\vec{\tilde{x}}^{i+1}) = \vec{\tilde{f}}^{int}(\vec{\tilde{x}}^{i+1}) - \vec{\tilde{f}}^{ext} = \vec{0}, \quad (\text{G.17})$$

where the internal forces at iteration $i + 1$ can be expressed as:

$$\vec{\tilde{f}}^{int}(\vec{\tilde{x}}^{i+1}) = \int_{\Omega_0^h} \vec{\nabla}_0 \mathbb{N}(\vec{X}_0) \cdot (\mathbf{F}^{-1}(\vec{x}^{i+1}) \cdot \boldsymbol{\tau}(\vec{x}^{i+1})) d\Omega_0. \quad (\text{G.18})$$

Then, the Kirchhoff stress tensor $\boldsymbol{\tau}(\vec{x}^{i+1})$, the deformation gradient tensor $\mathbf{F}(\vec{x}^{i+1})$ and its inverse $\mathbf{F}^{-1}(\vec{x}^{i+1})$ at iteration $i + 1$ can be expressed as the sum of their corresponding values at the previous iteration and the iterative corrections:

$$\boldsymbol{\tau}(\vec{x}^{i+1}) = \boldsymbol{\tau}(\vec{x}^i) + \delta\boldsymbol{\tau} \equiv \boldsymbol{\tau}^i + \delta\boldsymbol{\tau}, \quad (\text{G.19a})$$

$$\mathbf{F}(\vec{x}^{i+1}) = \mathbf{F}(\vec{x}^i) + \delta\mathbf{F} \equiv \mathbf{F}^i + \delta\mathbf{F}, \quad (\text{G.19b})$$

$$\mathbf{F}^{-1}(\vec{x}^{i+1}) = \mathbf{F}^{-1}(\vec{x}^i) + \delta\mathbf{F}^{-1} \equiv (\mathbf{F}^i)^{-1} + \delta\mathbf{F}^{-1}, \quad (\text{G.19c})$$

Note that $\delta\mathbf{F}^{-1}$ represents the iterative correction of \mathbf{F}^{-1} and not the inverse of the incremental correction of $\delta\mathbf{F}$.

Now, introducing (G.19a) and (G.19c) in (G.18) and neglecting the higher order terms

$$\vec{\tilde{f}}^{int}(\vec{\tilde{x}}^{i+1}) = \int_{\Omega_0^h} \vec{\nabla}_0 \mathbb{N}(\vec{X}_0) \cdot ((\mathbf{F}^i)^{-1} \cdot \boldsymbol{\tau}^i + (\mathbf{F}^i)^{-1} \cdot \delta\boldsymbol{\tau} + \delta\mathbf{F}^{-1} \cdot \boldsymbol{\tau}^i) d\Omega_0, \quad (\text{G.20})$$

and substituting (G.20) into (G.17), yields:

$$\int_{\Omega_0^h} \vec{\nabla}_0 \mathbb{N}(\vec{X}_0) \cdot ((\mathbf{F}^i)^{-1} \cdot \delta\boldsymbol{\tau} + \delta\mathbf{F}^{-1} \cdot \boldsymbol{\tau}^i) d\Omega_0 = \vec{\tilde{f}}^{ext} - \vec{\tilde{f}}^{int}(\vec{\tilde{x}}^i), \quad (\text{G.21})$$

with

$$\tilde{\mathbf{f}}^{int}(\tilde{\mathbf{x}}^i) = \int_{\Omega_0^h} \vec{\nabla}_0 \mathbb{N}(\vec{X}_0) \cdot ((\mathbf{F}^i)^{-1} \cdot \boldsymbol{\tau}^i) d\Omega_0. \quad (\text{G.22})$$

In these relations, the initial undeformed configuration is used as the reference configuration to compute the gradients and integrals. Using an updated Lagrange procedure, in each iteration the last known configuration can be used as the reference configuration. That is, the solution estimate of the unknown position vector field $\tilde{\mathbf{x}}^i$ obtained at the previous iteration is taken as the last known configuration. Then, using the deformation gradient tensor $\mathbf{F}^i = (\vec{\nabla}_0 \tilde{\mathbf{x}}^i)^T$, the infinitesimal volume in the undeformed configuration $d\Omega_0$ can be related to the infinitesimal volume $d\Omega^i$ in the last iterative configuration as:

$$d\Omega_0 = \frac{1}{\det(\mathbf{F}^i)} d\Omega^i = \frac{1}{J^i} d\Omega^i, \quad (\text{G.23})$$

and the gradient operators are related as:

$$\vec{\nabla}_0 = (\mathbf{F}^i)^T \cdot \vec{\nabla}^i. \quad (\text{G.24})$$

Using (G.23) and (G.24), expressions (G.21) and (G.22) can be formulated in the last known configuration, yielding:

$$\int_{\Omega_i^h} \vec{\nabla}^i \mathbb{N}(\vec{X}_0) \cdot (\mathbf{F}^i \cdot \delta \mathbf{F}^{-1} \cdot \boldsymbol{\tau}^i + \delta \boldsymbol{\tau}) \frac{1}{J^i} d\Omega^i = \tilde{\mathbf{f}}^{ext} - \tilde{\mathbf{f}}^{int}(\tilde{\mathbf{x}}^i), \quad (\text{G.25})$$

and

$$\tilde{\mathbf{f}}^{int}(\tilde{\mathbf{x}}^i) = \int_{\Omega_i^h} \vec{\nabla}^i \mathbb{N}(\vec{X}_0) \cdot \boldsymbol{\tau}^i \frac{1}{J^i} d\Omega^i. \quad (\text{G.26})$$

Now, introducing the second order tensor \mathbf{L}_δ ,

$$\mathbf{L}_\delta = \delta \mathbf{F} \cdot (\mathbf{F}^i)^{-1} = (\vec{\nabla}^i \delta \tilde{\mathbf{x}})^T, \quad (\text{G.27})$$

and performing the linearizations of $\delta \boldsymbol{\tau}$ and $\delta \mathbf{F}^{-1}$ with respect to $\delta \tilde{\mathbf{x}}$, expression (G.25) can be written as:

$$\int_{\Omega_i^h} \vec{\nabla}^i \mathbb{N}(\vec{X}_0) \cdot ([-{}^4\mathbb{I}^{RT} \cdot \boldsymbol{\tau}^i] : \mathbf{L}_\delta^T + \delta \boldsymbol{\tau}) \frac{1}{J^i} d\Omega^i = \tilde{\mathbf{f}}^{ext} - \tilde{\mathbf{f}}^{int}(\tilde{\mathbf{x}}^i). \quad (\text{G.28})$$

From the left hand side of (G.28), the element tangent stiffness matrix can be derived. In the first term, ${}^4\mathbb{I}^{RT} \cdot \boldsymbol{\tau}^i$, gives rise to the so-called *geometric stiffness* whereas the second term, $\delta \boldsymbol{\tau}$, is the starting point to obtain the *material stiffness*. The latter, requires to derive an expression for $\delta \boldsymbol{\tau}$ which yields the *material consistent tangent*. This is discussed next in G.3.

G.2 Stress update algorithm

G.2.1 Incremental time integration

The objective of the constitutive model described in Section 5.2.3 is to determine the stress \mathbf{S} and internal variables, D and $\dot{\gamma}_{vp}$, at time $t+1$ for a given strain increment,

provided that the corresponding values of the stress and internal variables at time t are known. This requires a time integration of the rate equations (5.28). To this end, a first order backward Euler scheme is used here:

$$\mathbf{S} = \mathbf{S}_t + {}^4\mathbf{C}_{elas} : \left[\mathbf{C} - \mathbf{C}_t - 2\mathbf{F}^T \cdot \Delta t \theta(T) Z(\varphi, D) \mathbf{N} \cdot \mathbf{F} - 2\mathbf{F}^T \cdot \Delta t \mathbf{D}_{th} \cdot \mathbf{F} \right], \quad (\text{G.29a})$$

$$D = D_t + \Delta t \theta(T) h(D) [Z(\varphi, D) - r(D)]. \quad (\text{G.29b})$$

where $\mathbf{D}_{th} = \mathbf{D}_{th}(T)$ temperature T are assumed fixed at a given increment. In the above expressions and in the following the subscript $t + 1$ is omitted for clarity.

To obtain the Kirchhoff stress tensor, the push-forward of \mathbf{S} towards the current configuration by means of \mathbf{F} is performed, which yields:

$$\boldsymbol{\tau} = \mathbf{F}_\Delta \cdot \boldsymbol{\tau}_t \cdot \mathbf{F}_\Delta^T + {}^4\mathbb{H} : [e_\Delta - \Delta t \theta(T) Z(\varphi, D) \mathbf{N} - \Delta t \mathbf{D}_{th}], \quad (\text{G.30})$$

with the fourth-order constitutive tensor ${}^4\mathbb{H}$ defined as:

$${}^4\mathbb{H} = 2\mathbf{F} \cdot \left[\mathbf{F} \cdot {}^4\mathbf{C}_{elas} \cdot \mathbf{F}^T \right]^{LT,RT} \cdot \mathbf{F}^T = 2[\mu - \lambda \ln(J_e)] {}^4\mathbb{H}^{RT} + \lambda \mathbf{I} \otimes \mathbf{I}. \quad (\text{G.31})$$

The incremental Almansi strain tensor e_Δ is given by:

$$e_\Delta = \frac{1}{2} \left[\mathbf{I} - \mathbf{F}_\Delta^{-T} \cdot \mathbf{F}_\Delta^{-1} \right], \quad (\text{G.32})$$

where \mathbf{F}_Δ is the incremental deformation gradient tensor, that is related to \mathbf{F} by:

$$\mathbf{F} = \mathbf{F}_\Delta \cdot \mathbf{F}_t. \quad (\text{G.33})$$

Moreover, the elastic predictor of the Kirchhoff stress tensor, i.e. assuming no viscoplastic deformation in the current increment, can be expressed as:

$$\boldsymbol{\tau}_e = \mathbf{F}_\Delta \cdot \boldsymbol{\tau}_t \cdot \mathbf{F}_\Delta^T + {}^4\mathbb{H} : [e_\Delta - \Delta t \mathbf{D}_{th}]. \quad (\text{G.34})$$

Note, that as a result of the selected multiplicative decomposition (4.8), the thermal velocity gradient tensor \mathbf{L}_{th} , and, consequently, the thermal rate of deformation tensor \mathbf{D}_{th} (both defined in the current configuration) do not involve elastic and viscoplastic terms. For a given temperature increment, \mathbf{D}_{th} can readily be computed according to (4.18a) and used in the elastic predictor (G.34). The subsequent viscoplastic corrector step can then be applied without any modifications with respect to the temperature independent viscoplastic model presented in [140].

By introducing (G.34) into (G.30), the total stress can be described as the elastic predictor minus the viscoplastic corrector:

$$\boldsymbol{\tau} = \boldsymbol{\tau}_e - \Delta t \theta(T) Z(\varphi, D) {}^4\mathbb{H} : \mathbf{N} \quad (\text{G.35})$$

Now, from (G.35) and (G.29b) the system of non-linear equations (G.29) can be rewritten as:

$$\mathbf{r}_\boldsymbol{\tau} = \boldsymbol{\tau} - \boldsymbol{\tau}_e + \Delta t \theta(T) Z(\varphi, D) {}^4\mathbb{H} : \mathbf{N} = \mathbf{0}, \quad (\text{G.36a})$$

$$r_D = D - D_t - \Delta t \theta(T) h(D) [Z(\varphi, D) - r(D)] = 0. \quad (\text{G.36b})$$

where $\mathbf{r}_\boldsymbol{\tau}$ and r_D refer to the tensorial residual of the stress equation and the scalar residual of the drag strength equation, respectively.

G.2.2 Newton-Raphson iterative procedure

In the stress update algorithm presented here, for every time increment, an initial trial elastic stress is determined from the predictor (G.34) and the yield condition (5.21) is evaluated. If the trial stress exceeds the yield limit, the non-linear system of equations (G.36) needs to be solved to determine the stress and the internal variables. This is performed via a standard Newton-Raphson iterative procedure, from which the stress and drag strength at iteration $i + 1$ can be obtained as:

$$\boldsymbol{\tau}^{i+1} = \boldsymbol{\tau}^i + \delta\boldsymbol{\tau}, \quad (\text{G.37a})$$

$$D^{i+1} = D^i + \delta D, \quad (\text{G.37b})$$

where $\delta\boldsymbol{\tau}$ and δD are the iterative updates of the stress and drag strength. These iterative updates of the unknowns are determined from the solution of the linearized system of equations. This requires the linearization of the residuals $\mathbf{r}_\boldsymbol{\tau}$ and r_D with respect to the stress $\boldsymbol{\tau}$ and drag strength D yielding:

$$\mathbf{r}_\boldsymbol{\tau}^{i+1} = \mathbf{r}_\boldsymbol{\tau}^i + \left. \frac{\partial \mathbf{r}_\boldsymbol{\tau}}{\partial \boldsymbol{\tau}} \right|_i : \delta\boldsymbol{\tau} + \left. \frac{\partial \mathbf{r}_\boldsymbol{\tau}}{\partial D} \right|_i \delta D = 0, \quad (\text{G.38a})$$

$$r_D^{i+1} = r_D^i + \left. \frac{\partial r_D}{\partial \boldsymbol{\tau}} \right|_i : \delta\boldsymbol{\tau} + \left. \frac{\partial r_D}{\partial D} \right|_i \delta D = 0. \quad (\text{G.38b})$$

The expressions for the partial derivatives entering (G.38) are given by:

$$\left. \frac{\partial \mathbf{r}_\boldsymbol{\tau}}{\partial \boldsymbol{\tau}} \right|_i = {}^4\mathbb{I} + \Delta t \theta(T) {}^4\mathbb{H}^i : \left[Z(\varphi^i, D^i) \left. \frac{\partial \mathbf{N}}{\partial \boldsymbol{\tau}} \right|_i + \mathbf{N}^i \otimes \left. \frac{\partial Z(\varphi, D)}{\partial \boldsymbol{\tau}} \right|_i \right], \quad (\text{G.39})$$

$$\left. \frac{\partial \mathbf{r}_\boldsymbol{\tau}}{\partial D} \right|_i = \Delta t \theta(T) \left. \frac{\partial Z(\varphi, D)}{\partial D} \right|_i {}^4\mathbb{H}^i : \mathbf{N}^i, \quad (\text{G.40})$$

$$\left. \frac{\partial r_D}{\partial \boldsymbol{\tau}} \right|_i = -\Delta t \theta(T) h(D^i) \left. \frac{\partial Z(\varphi, D)}{\partial \boldsymbol{\tau}} \right|_i, \quad (\text{G.41})$$

$$\begin{aligned} \left. \frac{\partial r_D}{\partial D} \right|_i &= 1 - \Delta t \theta(T) \left\{ h(D^i) \left[\left. \frac{\partial Z(\varphi, D)}{\partial D} \right|_i - \left. \frac{dr(D)}{dD} \right|_i \right] + \right. \\ &\quad \left. \left. \frac{dh(D)}{dD} \right|_i [Z(\varphi^i, D^i) - r(D^i)] \right\}. \end{aligned} \quad (\text{G.42})$$

In here, the required derivatives are:

$$\left. \frac{\partial Z(\varphi, D)}{\partial \boldsymbol{\tau}} \right|_i = \frac{nZ(\varphi^i, D^i)}{D^i} \coth \left[\frac{\varphi^i}{D^i} \right] \mathbf{N}^i, \quad (\text{G.43})$$

$$\left. \frac{\partial Z(\varphi, D)}{\partial D} \right|_i = -\frac{nZ(\varphi^i, D^i)}{D^{i2}} \coth \left[\frac{\varphi^i}{D^i} \right] \varphi^i, \quad (\text{G.44})$$

$$\left. \frac{\partial \mathbf{N}}{\partial \boldsymbol{\tau}} \right|_i = \frac{1}{\tau_{eq}} \left[\frac{3}{2} {}^4\mathbb{I} - \frac{1}{2} \mathbf{I} \otimes \mathbf{I} - \mathbf{N}^i \otimes \mathbf{N}^i \right], \quad (\text{G.45})$$

$$\left. \frac{dh(D)}{dD} \right|_i = \frac{m}{\delta C \varphi_D^i} [1 - \varphi_D^i \coth[\varphi_D^i]] h(D^i), \quad (\text{G.46})$$

$$\left. \frac{dr(D)}{dD} \right|_i = \frac{n}{\delta C} \coth[\varphi_D^i] r(D^i), \quad (\text{G.47})$$

G.3 Element tangent stiffness matrix

The element tangent stiffness matrix is obtained from the left hand side of (G.28). The first step, is to determine an expression for the variation of the stress $\delta\boldsymbol{\tau}$, which yields the material contribution to the element tangent stiffness. The starting point for this derivation is expression (G.35) Taking the variation thereof leads to

$$\delta\boldsymbol{\tau} = \delta\boldsymbol{\tau}_e - \delta [\Delta t \theta(T) Z(\varphi, D)^4 \mathbb{H} : \mathbf{N}]. \quad (\text{G.48})$$

$\delta\boldsymbol{\tau}_e$ represents the variation of the stress during and elastic increment and gives rise to the elastic consistent tangent ${}^4\mathbb{C}_e$,

$$\delta\boldsymbol{\tau}_e = \delta \left[\mathbf{F}_\Delta \cdot \boldsymbol{\tau}_t \cdot \mathbf{F}_\Delta^T + {}^4\mathbb{H} : [\mathbf{e}_\Delta - \Delta t \mathbf{D}_{th}] \right] \quad (\text{G.49})$$

$$\delta\boldsymbol{\tau}_e = \delta \mathbf{F}_\Delta \cdot \boldsymbol{\tau}_t \cdot (\mathbf{F}_\Delta^i)^T + \mathbf{F}_\Delta^i \cdot \boldsymbol{\tau}_t \cdot \delta \mathbf{F}_\Delta^T + \left. \frac{\partial {}^4\mathbb{H}}{\partial J_e} \right|_i : (\mathbf{e}_\Delta - \Delta t \mathbf{D}_{th}) \delta J_e + {}^4\mathbb{H}^i : \delta \mathbf{e}_\Delta \quad (\text{G.50})$$

$$\begin{aligned} \delta\boldsymbol{\tau}_e &= \left[2 {}^4\mathbb{I}^S : (\mathbf{F}_\Delta^i \cdot \boldsymbol{\tau}_t \cdot (\mathbf{F}_\Delta^i)^T) \right] : \mathbf{L}_\delta^T + \\ &\left[{}^4\mathbb{H}^i : \left[{}^4\mathbb{I}^S \cdot (\mathbf{F}_\Delta^i)^{-T} \cdot (\mathbf{F}_\Delta^i)^{-1} \right]^{RT} + J_e^i \left. \frac{\partial {}^4\mathbb{H}}{\partial J_e} \right|_i : (\mathbf{e}_\Delta - \Delta t \mathbf{D}_{th}) \otimes \mathbf{I} \right] : \mathbf{L}_\delta^T \end{aligned} \quad (\text{G.51})$$

$$\delta\boldsymbol{\tau}_e = {}^4\mathbb{C}_e : \mathbf{L}_\delta^T, \quad (\text{G.52})$$

where $\mathbf{L}_\delta = \delta \mathbf{F} \cdot (\mathbf{F}^i)^{-1} = \delta \mathbf{F}_\Delta \cdot (\mathbf{F}_\Delta^i)^{-1}$ have been used and ${}^4\mathbb{C}_e$ has been identified as

$$\begin{aligned} {}^4\mathbb{C}_e &= \left[2 {}^4\mathbb{I}^S : (\mathbf{F}_\Delta^i \cdot \boldsymbol{\tau}_t \cdot (\mathbf{F}_\Delta^i)^T) \right] + {}^4\mathbb{H}^i : \left[{}^4\mathbb{I}^S \cdot (\mathbf{F}_\Delta^i)^{-T} \cdot (\mathbf{F}_\Delta^i)^{-1} \right]^{RT} + \\ &J_e^i \left. \frac{\partial {}^4\mathbb{H}}{\partial J_e} \right|_i : (\mathbf{e}_\Delta - \Delta t \mathbf{D}_{th}) \otimes \mathbf{I}. \end{aligned} \quad (\text{G.53})$$

with

$$\left. \frac{{}^4\mathbb{H}}{\partial J_e} \right|_i = -2\lambda \frac{1}{J_e^i} {}^4\mathbb{I}^{RT}. \quad (\text{G.54})$$

During a viscoplastic increment, the contribution of the last term of (G.48) needs to be taken into account. Thus,

$$\begin{aligned} \delta [\Delta t \theta(T)^4 \mathbb{H} : (Z(\varphi, D) \mathbf{N})] &= \\ \Delta t \theta(T) \left[{}^4\mathbb{H}^i : \delta [Z(\varphi, D) \mathbf{N}] + \delta {}^4\mathbb{H} : [Z(\varphi^i, D^i) \mathbf{N}^i] \right]. \end{aligned} \quad (\text{G.55})$$

The first term on the right hand side $\delta [Z(\varphi, D)\mathbf{N}]$ is given by

$$\begin{aligned} \delta [Z(\varphi, D)\mathbf{N}] &= Z(\varphi^i, D^i) \frac{\partial \mathbf{N}}{\partial \boldsymbol{\tau}} \Big|_i : \delta \boldsymbol{\tau} + \left[\frac{\partial Z(\varphi, D)}{\partial \boldsymbol{\tau}} \Big|_i : \delta \boldsymbol{\tau} + \frac{\partial Z(\varphi, D)}{\partial D} \Big|_i \delta D \right] \mathbf{N}^i = \\ &= \left[Z(\varphi^i, D^i) \frac{\partial \mathbf{N}}{\partial \boldsymbol{\tau}} \Big|_i + \mathbf{N}^i \otimes \frac{\partial Z(\varphi, D)}{\partial \boldsymbol{\tau}} \Big|_i \right] : \delta \boldsymbol{\tau} + \frac{\partial Z(\varphi, D)}{\partial D} \Big|_i \mathbf{N}^i \delta D. \end{aligned} \quad (\text{G.56})$$

Considering that

$$\delta^4 \mathbb{H} = \frac{\partial^4 \mathbb{H}}{\partial J_e} \Big|_i \delta J_e = \left[-2\lambda \frac{1}{J_e^i} {}^4 \mathbb{I}^{RT} \right] \left[J_e^i \mathbf{I} : \mathbf{L}_\delta^T \right] = -2\lambda \left[\mathbf{I} : \mathbf{L}_\delta^T \right] {}^4 \mathbb{I}^{RT}, \quad (\text{G.57})$$

the second term on the right hand side of (G.55) can be written as

$$\delta^4 \mathbb{H} : [Z(\varphi^i, D^i)\mathbf{N}^i] = -2\lambda \left(Z(\varphi^i, D^i)\mathbf{N}^i \right) \left[\mathbf{I} : \mathbf{L}_\delta^T \right]. \quad (\text{G.58})$$

Now, substituting (G.52), (G.55), (G.56), (G.58) in (G.48) yields

$$\begin{aligned} \delta \boldsymbol{\tau} &= {}^4 \mathbb{C}_e : \mathbf{L}_\delta^T \\ &- \Delta t \theta(T) \left\{ {}^4 \mathbb{H}^i : \left[\left(Z(\varphi^i, D^i) \frac{\partial \mathbf{N}}{\partial \boldsymbol{\tau}} \Big|_i + \mathbf{N}^i \otimes \frac{\partial Z(\varphi, D)}{\partial \boldsymbol{\tau}} \Big|_i \right) : \delta \boldsymbol{\tau} \right. \right. \\ &\left. \left. + \frac{\partial Z(\varphi, D)}{\partial D} \Big|_i \mathbf{N}^i \delta D \right] - 2\lambda \left(Z(\varphi^i, D^i)\mathbf{N}^i \right) \left[\mathbf{I} : \mathbf{L}_\delta^T \right] \right\}, \end{aligned} \quad (\text{G.59})$$

which can be conveniently reworked as follows,

$$\begin{aligned} \delta \boldsymbol{\tau} + \Delta t \theta(T) {}^4 \mathbb{H}^i : \left[Z(\varphi^i, D^i) \frac{\partial \mathbf{N}}{\partial \boldsymbol{\tau}} \Big|_i + \mathbf{N}^i \otimes \frac{\partial Z(\varphi, D)}{\partial \boldsymbol{\tau}} \Big|_i \right] : \delta \boldsymbol{\tau} \\ + \Delta t \theta(T) {}^4 \mathbb{H}^i : \left[\frac{\partial Z(\varphi, D)}{\partial D} \Big|_i \mathbf{N}^i \right] \delta D = \end{aligned} \quad (\text{G.60})$$

$$\begin{aligned} &{}^4 \mathbb{C}_e : \mathbf{L}_\delta^T + \Delta t \theta(T) 2\lambda \left(Z(\varphi^i, D^i)\mathbf{N}^i \right) \left[\mathbf{I} : \mathbf{L}_\delta^T \right], \\ &\left\{ {}^4 \mathbb{I} + \Delta t \theta(T) {}^4 \mathbb{H}^i : \left[Z(\varphi^i, D^i) \frac{\partial \mathbf{N}}{\partial \boldsymbol{\tau}} \Big|_i + \mathbf{N}^i \otimes \frac{\partial Z(\varphi, D)}{\partial \boldsymbol{\tau}} \Big|_i \right] \right\} : \delta \boldsymbol{\tau} \\ &+ \Delta t \theta(T) {}^4 \mathbb{H}^i : \left[\frac{\partial Z(\varphi, D)}{\partial D} \Big|_i \mathbf{N}^i \right] \delta D = \end{aligned} \quad (\text{G.61})$$

$$\left[{}^4 \mathbb{C}_e + \Delta t \theta(T) 2\lambda Z(\varphi^i, D^i) \left(\mathbf{N}^i \otimes \mathbf{I} \right) \right] : \mathbf{L}_\delta^T.$$

Comparing the terms involving $\delta \boldsymbol{\tau}$ and δD with expressions (G.38), (G.39) and (G.40), it can be noticed that the left hand side of (G.61) represents the variation of the residual $\mathbf{r}_\boldsymbol{\tau}$. Making use of the definitions given in (G.39) and (G.40) yields,

$$\frac{\partial \mathbf{r}_\boldsymbol{\tau}}{\partial \boldsymbol{\tau}} \Big|_i : \delta \boldsymbol{\tau} + \frac{\partial \mathbf{r}_\boldsymbol{\tau}}{\partial D} \Big|_i \delta D = \left[{}^4 \mathbb{C}_e + \Delta t \theta(T) 2\lambda Z(\varphi^i, D^i) \left(\mathbf{N}^i \otimes \mathbf{I} \right) \right] : \mathbf{L}_\delta^T. \quad (\text{G.62})$$

In addition, introducing the fourth-order tensor ${}^4\mathbb{T}$,

$${}^4\mathbb{T} = 2\lambda\Delta t\theta(T) \left[Z(\varphi^i, D^i) \left(\mathbf{N}^i \otimes \mathbf{I} \right) \right], \quad (\text{G.63})$$

(G.62) can be expressed as

$$\left. \frac{\partial \mathbf{r}_\tau}{\partial \boldsymbol{\tau}} \right|_i : \delta \boldsymbol{\tau} + \left. \frac{\partial \mathbf{r}_\tau}{\partial D} \right|_i \delta D = \left[{}^4\mathbb{C}_e + {}^4\mathbb{T} \right] : \mathbf{L}_\delta^T. \quad (\text{G.64})$$

Equation (G.64) is defined in terms of $\delta \boldsymbol{\tau}$ and δD . To obtain an expression for $\delta \boldsymbol{\tau}$ only, the dependence of δD on $\delta \boldsymbol{\tau}$ needs to be eliminated from (G.64). The variation of δD yields,

$$\delta D = \delta \left\{ D_t + \Delta t \theta(T) h(D) [Z(\varphi, D) - r(D)] \right\}, \quad (\text{G.65})$$

$$\delta D = \Delta t \theta(T) \delta \left\{ h(D^i) \delta [Z(\varphi, D) - r(D)] + \delta h(D) [Z(\varphi^i, D^i) - r(D^i)] \right\}, \quad (\text{G.66})$$

$$\begin{aligned} \delta D = \Delta t \theta(T) & \left\{ h(D^i) \left. \frac{\partial Z(\varphi, D)}{\partial \boldsymbol{\tau}} \right|_i : \delta \boldsymbol{\tau} + \left[h(D^i) \left(\left. \frac{\partial Z(\varphi, D)}{\partial D} \right|_i - \left. \frac{dr(D)}{dD} \right|_i \right) + \right. \\ & \left. \left. \frac{dh(D)}{dD} \right|_i \left(Z(\varphi^i, D^i) - r(D^i) \right) \right\} \delta D, \end{aligned} \quad (\text{G.67})$$

$$\begin{aligned} \delta D - \Delta t \theta(T) & \left[h(D^i) \left(\left. \frac{\partial Z(\varphi, D)}{\partial D} \right|_i - \left. \frac{dr(D)}{dD} \right|_i \right) + \left. \frac{dh(D)}{dD} \right|_i \left(Z(\varphi^i, D^i) - r(D^i) \right) \right] \delta D = \\ & \Delta t \theta(T) \left[h(D^i) \left. \frac{\partial Z(\varphi, D)}{\partial \boldsymbol{\tau}} \right|_i \right] : \delta \boldsymbol{\tau}, \end{aligned} \quad (\text{G.68})$$

$$\begin{aligned} \left\{ 1 - \Delta t \theta(T) \left[h(D^i) \left(\left. \frac{\partial Z(\varphi, D)}{\partial D} \right|_i - \left. \frac{dr(D)}{dD} \right|_i \right) + \left. \frac{dh(D)}{dD} \right|_i \left(Z(\varphi^i, D^i) - r(D^i) \right) \right] \right\} \delta D = \\ \Delta t \theta(T) \left[h(D^i) \left. \frac{\partial Z(\varphi, D)}{\partial \boldsymbol{\tau}} \right|_i \right] : \delta \boldsymbol{\tau}, \end{aligned} \quad (\text{G.69})$$

Again, in (G.69) it is trivial to identify the derivatives of r_D , (G.41) and (G.42) in (G.69). Introducing these expressions in (G.69) and rearranging gives

$$\left. \frac{\partial r_D}{\partial \boldsymbol{\tau}} \right|_i : \delta \boldsymbol{\tau} + \left. \frac{\partial r_D}{\partial D} \right|_i \delta D = 0, \quad (\text{G.70})$$

from which it is possible to obtain the expression for δD as a function of $\delta \boldsymbol{\tau}$,

$$\delta D = - \left[\left. \frac{\partial r_D}{\partial D} \right|_i \right]^{-1} \left. \frac{\partial r_D}{\partial \boldsymbol{\tau}} \right|_i : \delta \boldsymbol{\tau}. \quad (\text{G.71})$$

Substituting (G.71) in (G.64) leads to

$$\left. \frac{\partial \mathbf{r}_\tau}{\partial \boldsymbol{\tau}} \right|_i : \delta \boldsymbol{\tau} - \left. \frac{\partial \mathbf{r}_\tau}{\partial D} \right|_i \left[\left. \frac{\partial r_D}{\partial D} \right|_i \right]^{-1} \otimes \left. \frac{\partial r_D}{\partial \boldsymbol{\tau}} \right|_i : \delta \boldsymbol{\tau} = \left[{}^4\mathbb{C}_e + {}^4\mathbb{T} \right] : \mathbf{L}_\delta^T. \quad (\text{G.72})$$

After some tensorial operations this yields

$$\delta \boldsymbol{\tau} = {}^4\mathbb{N} : \left[{}^4\mathbf{C}_e + {}^4\mathbb{T} \right] : \mathbf{L}_\delta^T, \quad (\text{G.73})$$

$$\delta \boldsymbol{\tau} = {}^4\mathbf{C}_{vp} : \mathbf{L}_\delta^T. \quad (\text{G.74})$$

where the viscoplastic consistent tangent is given by:

$${}^4\mathbf{C}_{vp} = {}^4\mathbb{N} : \left[{}^4\mathbf{C}_e + {}^4\mathbb{T} \right]. \quad (\text{G.75})$$

In (G.73), ${}^4\mathbb{N}$ is defined such that

$${}^4\mathbb{N} : \left\{ \left. \frac{\partial \mathbf{r}_\tau}{\partial \boldsymbol{\tau}} \right|_i - \left[\frac{\partial r_D}{\partial D} \right]_i^{-1} \left[\frac{\partial \mathbf{r}_\tau}{\partial D} \right]_i \otimes \frac{\partial r_D}{\partial \boldsymbol{\tau}} \right\} = {}^4\mathbb{I}, \quad (\text{G.76})$$

Next, using (G.74) for the variation of the stress in the left hand side of (G.28) and rearranging, leads to

$$\int_{\Omega_{i^h}} \vec{\nabla}^i \mathbb{N}(\vec{X}_0) \cdot (-{}^4\mathbb{I}^{RT} \cdot \boldsymbol{\tau}^i + {}^4\mathbf{C}_{vp}) : \mathbf{L}_\delta^T \frac{1}{J^i} d\Omega^i = \tilde{\mathbf{f}}^{ext} - \tilde{\mathbf{f}}^{int}(\vec{x}^i), \quad (\text{G.77})$$

Expressing \mathbf{L}_δ^T in terms of the column of iterative corrections to the position vectors of the nodes $\delta \vec{x}$ gives

$$\mathbf{L}_\delta^T = \vec{\nabla}^i \delta \vec{x} \approx \vec{\nabla}^i \delta \vec{x}^h = (\vec{\nabla}^i \mathbb{N}(\vec{X}_0))^T \delta \vec{x}, \quad (\text{G.78})$$

Now, introducing (G.78) into (G.77) and taking into account that $\delta \vec{x}^h$ contains the nodal degree of freedom that can be taken outside the integral, it gives

$$\left\{ \int_{\Omega_{i^h}} \vec{\nabla}^i \mathbb{N}(\vec{X}_0) \cdot (-{}^4\mathbb{I}^{RT} \cdot \boldsymbol{\tau}^i + {}^4\mathbf{C}_{vp}) \cdot (\vec{\nabla}^i \mathbb{N}(\vec{X}_0))^T \frac{1}{J^i} d\Omega^i \right\} \cdot \delta \vec{x} = \tilde{\mathbf{f}}^{ext} - \tilde{\mathbf{f}}^{int}(\vec{x}^i), \quad (\text{G.79})$$

from which the tensorial element stiffness matrix can be identified as

$$\underline{\mathbf{K}}^i = \int_{\Omega_{i^h}} \vec{\nabla}^i \mathbb{N}(\vec{X}_0) \cdot (-{}^4\mathbb{I}^{RT} \cdot \boldsymbol{\tau}^i + {}^4\mathbf{C}_{vp}) \cdot (\vec{\nabla}^i \mathbb{N}(\vec{X}_0))^T \frac{1}{J^i} d\Omega^i. \quad (\text{G.80})$$

Bibliography

- [1] *ASM Metals Handbook, Volume 1 - Properties and Selection: Irons, Steels, and High-Performance Alloys*. ASM International, United States of America, 1990.
- [2] *ASM Metals Handbook, Volume 19 - Fatigue and Fracture*. ASM International, United States of America, 1996.
- [3] *Gusseisen mit Lamellengraphit - Eigenschaften und Anwendung. Konstruieren + Giessen*. Zentrale für Gussverwendung. VDI-Verlag, Düsseldorf, 2000.
- [4] Aisi 1070 steel, hot rolled, 19-32 mm (0.75-1.25 in) round. *www.matweb.com*, January 2014.
- [5] S. Allain and O. Bouaziz. Microstructure based modeling for the mechanical behavior of ferrite–pearlite steels suitable to capture isotropic and kinematic hardening. *Materials Science and Engineering: A*, 496(1):329–336, 2008.
- [6] H. Altenbach, G.B. Stoychev, and K.N. Tushtev. On elastoplastic deformation of grey cast iron. *International Journal of Plasticity*, 17(5):719–736, 2001.
- [7] R.J. Arsenault and M. Taya. Thermal residual stress in metal matrix composite. *Acta Metallurgica*, 35(3):651–659, 1987.
- [8] J.M. Atienza and M. Elices. Behavior of prestressing steels after a simulated fire: Fire-induced damages. *Construction and Building Materials*, 23(8):2932–2940, 2009.
- [9] D.K. Balch, T.J. Fitzgerald, V.J. Michaud, A. Mortensen, Y.-L. Shen, and S. Suresh. Thermal Expansion of Metals Reinforced with Ceramic Particles and Microcellular Foams. *Metallurgical and Materials Transactions A*, 27A:3700–3717, 1996.
- [10] C. Berdin, M.J. Dong, and C. Prioul. Local approach of damage and fracture toughness for nodular cast iron. *Engineering Fracture Mechanics*, 68(9):1107–1117, 2001.
- [11] L.I.J.C. Bergers, J.P.M. Hoefnagels, and M.G.D. Geers. On-wafer time-dependent high reproducibility nano-force tensile testing. *Journal of Physics D: Applied Physics*, 47(49):495306, 2014.

- [12] L.I.J.C. Bergers, J. Neggers, M.G.D. Geers, and J.P.M. Hoefnagels. Enhanced global digital image correlation for accurate measurement of microbeam bending. In *Advanced Materials Modelling for Structures*, pages 43–51. Springer, 2013.
- [13] M. Beusink. Multi-time scale methods for an efficient finite element analysis of fatigue problems. Master’s thesis, Eindhoven University of Technology, 2013.
- [14] P.A. Blackmore and K. Morton. Structure-property relationships in graphitic cast irons. *International Journal of Fatigue*, 4(3):149–155, 1982.
- [15] O.L. Blakslee, D.G. Proctor, E.J. Seldin, G.B. Spence, and T. Weng. Elastic constants of compression-annealed pyrolytic graphite. *Journal of Applied Physics*, 41(8):3373–3382, 1970.
- [16] A.R. Boccaccini. Young’s modulus of cast-iron as a function of volume content, shape and orientation of graphite inclusions. *Zeitschrift für Metallkunde*, 88:23–26, 1997.
- [17] N. Bonora and A. Ruggiero. Micromechanical modeling of ductile cast iron incorporating damage. Part I: Ferritic ductile cast iron. *International Journal of Solids and Structures*, 42:1401–1424, 2005.
- [18] S.Y. Buni, N. Raman, and S. Seshan. The role of graphite morphology and matrix structure on the low frequency thermal cycling of cast irons. *Sadhana*, 29(1):117–127, 2004.
- [19] W.D. Callister. *Materials science and engineering: an introduction*. John Wiley & Sons, Inc, United States of America, 2003.
- [20] J.L. Chaboche. A review of some plasticity and viscoplasticity constitutive theories. *International Journal of Plasticity*, 24:1642–1693, 2008.
- [21] C.G. Chao, T.S. Lui, and M.H. Hon. The effect of triaxial stress field on intermediate temperature embrittlement of ferritic spheroidal graphite cast irons. *Metallurgical Transactions A*, 19(5):1213–1219, 1988.
- [22] C.G. Chao, T.S. Lui, and M.H. Hon. A study of tensile properties of ferritic compacted graphite cast irons at intermediate temperatures. *Journal of Materials Science*, 24:2610–2614, 1989.
- [23] C.G. Chao, T.S. Lui, and M.H. Hon. The effect of microstructure of ferritic spheroidal graphite cast irons on intergranular fracture at intermediate temperatures. *Metallurgical Transactions A*, 20(3):431–436, 1989.
- [24] C. Chen and T.J. Lu. A phenomenological framework of constitutive modelling for incompressible and compressible elasto-plastic solids. *International Journal of Solids and Structures*, 37(52):7769–7786, 2000.

- [25] L. Chuzhoy, R.E. DeVor, D.J. Bammann, S.G. Kapoor, and A.J. Beaudoin. Machining simulation of ductile iron and its constituents, part 1: Estimation of material model parameters and their validation. *Journal of Manufacturing Science and Engineering*, 125(2):181–191, 2003.
- [26] L. Chuzhoy, R.E. DeVor, and S.G. Kapoor. Machining simulation of ductile iron and its constituents, part 2: Numerical simulation and experimental validation of machining. *Journal of Manufacturing Science and Engineering*, 125(2):192–201, 2003.
- [27] L. Chuzhoy, R.E. DeVor, S.G. Kapoor, and D.J. Bammann. Microstructure-level modeling of ductile iron machining. *Journal of Manufacturing Science and Engineering*, 124(2):162–169, 2002.
- [28] CLAASGUSS. Grey lamellar graphite cast iron. *Technical information No. 1*, Rev. 01/04, 2006.
- [29] CLAASGUSS. Spheroidal cast iron EN-GJS (formerly GGG). *Technical information No. 2*, Rev. 01/04, 2006.
- [30] CLAASGUSS. Vermicular graphite cast iron. *Technical information No. 12*, 2006.
- [31] L. Collini and G. Nicoletto. Determination of the relationship between microstructure and constitutive behaviour of nodular cast iron with a unit cell model. *The Journal of Strain Analysis for Engineering Design*, 40(2):107–116, 2005.
- [32] G.M.E. Cooke. An introduction to the mechanical properties of structural steel at elevated temperatures. *Fire Safety Journal*, 13(1):45–54, 1988.
- [33] C.A. Cooper, R. Elliot, and R.J. Young. Investigation of elastic property relationships for flake and spheroidal cast irons using Raman spectroscopy. *Acta Materialia*, 50:4037–4046, 2002.
- [34] G. Daehn. Thermal cycling and related strain mismatch in metal matrix composites. *Comprehensive Composite Materials*, 3:419–445, 2000.
- [35] P.Q. Dai, Z.R. He, W.Q. Wu, and Z.Y. Mao. Mechanical behaviour of graphite in fracture of autempered ductile iron. *Materials Science and Technology*, 18(9):1052–1056, 2002.
- [36] E.A. de Souza Neto, D. Peric, and D.R.J. Owen. *Computational Methods for Plasticity: Theory and Applications*. John Wiley & Sons, 2008.
- [37] F. Delannay. Thermal stresses and thermal expansion in MMCs. *Comprehensive Composite Materials*, 3:341–369, 2000.
- [38] P. Dierickx, C. Verdu, and A. Reynaud. A study of physico-chemical mechanics responsible for damage of the heat treated and as-cast ferritic spheroidal graphite cast irons. *Scripta Materialia*, 34(2):261–268, 1996.

- [39] G.E. Dieter. *Mechanical Metallurgy*. McGraw-Hill Education, UK, 1989.
- [40] M. Dollar, I.M. Bernstein, and A.W. Thompson. Influence of deformation substructure on flow and fracture of fully pearlitic steel. *Acta Metallurgica*, 36(2):311–320, 1988.
- [41] M.J. Dong, C. Prioul, and D. François. Damage effect on the fracture toughness of nodular cast iron: Part I. Damage characterization and plastic flow stress modeling. *Metallurgical and Materials Transactions A*, 28(11):2245–2254, 1997.
- [42] S.D. Downing and D.F. Socie. Stress/strain simulation model for grey cast iron. *International Journal of Fatigue*, 4(3):143–148, 1982.
- [43] J.R. Dryden, A.S. Deakin, and G.S. Purdy. Elastic analysis of deformation near a spherical carbon particle embedded in iron. *Acta Metallurgica*, 35(3):681–689, 1987.
- [44] J.R. Davis (editor). *ASM Specialty Handbook: Cast Irons*. ASM International, United States of America, 1996.
- [45] E.I. Saavedra Flores and E.A. de Souza Neto. Remarks on symmetry conditions in computational homogenisation problems. *Engineering Computations*, 27(4):551–575, 2010.
- [46] A.D. Freed and K.P. Walker. Viscoplasticity with creep and plasticity bounds. *International Journal of Plasticity*, 9:213–242, 1993.
- [47] N.K. Fukumasu, P.L. Pelegrino, G. Cueva, R.M. Souza, and A. Sinatora. Numerical analysis of the stresses developed during the sliding of a cylinder over the compact graphite iron. *Wear*, 259:1400–1407, 2005.
- [48] E. Garofalo, P.R. Malenock, and G.V. Smith. The influence of temperature on the elastic constants of some commercial steels. *Determination of Elastic Constants, Special Technical Publication, American Society for Testing and Materials*, page 10, 1952.
- [49] F. Garofalo. An empirical relation defining the stress dependence of minimum creep rate in metals. *Transactions of the Metallurgical Society AIME*, 227(2):351–355, 1963.
- [50] W. Gaudig, R. Mellert, U. Weber, and S. Schmauder. Self-consistent one-particle 3d unit cell model for simulation of the effect of graphite aspect ratio on Young’s modulus of cast-iron. *Computational materials science*, 28(3):654–662, 2003.
- [51] S. Ghodrati. *Thermo-mechanical fatigue of compacted graphite iron in diesel engine components*. PhD thesis, TU Delft, Delft University of Technology, 2013.

- [52] T. Gocmez and S. Trampert. Cast Irons for Diesel Cylinder Heads: Modelling, Failure Analysis and Trends. *Niedernhausen near Wiesbaden, Germany, December 5 - 6*, NAFEMS Seminar: "Materials Modeling - FE Simulations of the Behavior of Modern Industrial Materials Including their Failure(1):1–15, 2006.
- [53] B.M. Gonzalez, L.A. Marchi, da E.J. Fonseca, P.J. Modenesi, and V.T. Buono. Measurement of dynamic strain aging in pearlitic steels by tensile test. *ISIJ International*, 43(3):428–432, 2003.
- [54] C. Guillemer-Neel, X. Feaugas, and M. Clavel. Mechanical behavior and damage kinetics in nodular cast iron: Part I. damage mechanisms. *Metallurgical and Materials Transactions A*, 31(12):3063–3074, 2000.
- [55] C. Guillemer-Neel, X. Feaugas, and M. Clavel. Mechanical behavior and damage kinetics in nodular cast iron: Part II. hardening and damage. *Metallurgical and Materials Transactions A*, 31(12):3075–3085, 2000.
- [56] R.B. Gundlach. Elevated temperature properties of alloyed gray irons for diesel engine components. *AFS International Cast Metal Journal*, 4(3):11–20, 1979.
- [57] R.B. Gundlach. Thermal Fatigue resistance of alloyed gray irons for diesel engine components. *Transactions of the American Foundrymen's Society*, 87:551–560, 1980.
- [58] R.B. Gundlach. The effect of alloying elements on the elevated temperature properties of gray irons. *Transactions of the American Foundrymen's Society*, 91:389–422, 1983.
- [59] S. Hartmann. Comparison of the multiplicative decompositions $F = F_\theta F_M$ and $F = F_M F_\theta$ in finite strain thermo-elasticity. *Fakultät für Mathematik/Informatik und Maschinenbau, Technische Universität Clausthal*, Fac3-12-02:1–13, 2012.
- [60] A. Hatton, M. Engstler, P. Leidbenguth, and F. Mücklich. Characterization of graphite crystal structure and growth mechanisms using FIB and 3D image analysis. *Advanced Engineering Materials*, 13(3):136–144, 2010.
- [61] P. Haupt. *Continuum Mechanics and Theory of Materials*. Springer, 2000.
- [62] Z.R. He, G.X. Lin, and D. Ji. A new understanding on the relation among microstructure micro interfacial mechanical behaviour and macro mechanical properties in cast iron. *Materials Science and Engineering A*, 234–236:161–164, 1997.
- [63] J. Helsing and G. Grimvall. Thermal conductivity of cast iron: Models and analysis of experiments. *Journal of applied physics*, 70(3):1198–1206, 1991.
- [64] H.E. Hjelm. Yield surface for grey cast iron under biaxial stress. *Journal of engineering materials and technology*, 116(2):148–154, 1994.

- [65] D. Holmgren, A. Dioszegi, and I.L. Svensson. Effects of nodularity on thermal conductivity of cast iron. *International Journal of Cast Metals Research*, 20(1):30–40, 2007.
- [66] D. Holmgren, R. Källbom, and I.L. Svensson. Influences of the graphite growth direction on the thermal conductivity of cast iron. *Metallurgical and Materials Transactions A*, 38(2):268–275, 2007.
- [67] D.M. Holmgren. Review of thermal conductivity of cast iron. *International Journal of Cast Metals Research*, 18(6):331–345, 2005.
- [68] D.M. Holmgren, A. Diószegi, and I.L. Svensson. Effects of transition from lamellar to compacted graphite on thermal conductivity of cast iron. *International Journal of Cast Metals Research*, 19(6):303–313, 2006.
- [69] G.A. Holzapfel. *Nonlinear Solid Mechanics: a Continuum Approach for Engineering*. John Wiley & Sons Ltd., 2000.
- [70] K. Hono, M. Ohnuma, M. Murayama, S. Nishida, A. Yoshie, and T. Takahashi. Cementite decomposition in heavily drawn pearlite steel wire. *Scripta Materialia*, 44(6):977–984, 2001.
- [71] E. Hornbogen. Fracture toughness and fatigue crack growth of grey cast irons. *Journal of Materials Science*, 20:3897–3905, 1985.
- [72] C.L. Hsieh and W.H. Tuan. Thermal expansion behaviour of a model ceramic-metal composite. *Materials Science and Engineering A*, 460–461:453–458, 2007.
- [73] F. Iacovello, O. Di Bartolomeo, V. Di Cocco, and V. Piacente. Damaging micromechanisms in ferritic-pearlitic ductile cast irons. *Materials Science and Engineering A*, 478:181–186, 2008.
- [74] A. Inoue, T. Ogura, and T. Masumoto. Microstructures of deformation and fracture of cementite in pearlitic carbon steels strained at various temperatures. *Metallurgical Transactions A*, 8(11):1689–1695, 1977.
- [75] H.R. Javani, R.H.J. Peerlings, and M.G.D. Geers. Three dimensional modelling of non-local ductile damage: element technology. *International Journal of Material Forming*, 2(1):923–926, 2009.
- [76] B.L. Josefson, U. Stigh, and H.E. Hjelm. A nonlinear kinematic hardening model for elastoplastic deformations in grey cast iron. *Journal of engineering materials and technology*, 117(2):145–150, 1995.
- [77] A.D. Kammers and S. Daly. Digital image correlation under scanning electron microscopy: Methodology and validation. *Experimental Mechanics*, 53(9):1743–1761, 2013.
- [78] J.R. Kattus and B. McPherson. *Report on Properties of Cast Iron at Elevated Temperatures - ASTM Special Technical Publication No. 248*. American Society for Testing Materials, Philadelphia, 1959.

- [79] N.V.V.R. Murthy Kolluri, M.H.L. Thiessen, J.P.M. Hoefnagels, J.A.W. van Dommelen, and M.G.D. Geers. In-situ characterization of interface delamination by a new miniature mixed mode bending setup. *International Journal of Fracture*, 158(2):183–195, 2009.
- [80] V.G. Kouznetsova, W.A.M. Brekelmans, and F.P.T. Baaijens. An approach to micro-macro modeling of heterogeneous materials. *Computational Mechanics*, 27(1):37–48, 2001.
- [81] G. Krauss. *Steels: processing, structure, and performance*. ASM International, 2005.
- [82] M. Kuna and D.-Z. Sun. Analyses of void growth and coalescence in cast iron by cell models. *Journal De Physique IV*, 6:113–122, 1996.
- [83] G. Langford. Deformation of pearlite. *Metallurgical and Materials Transactions A*, 8(6):861–875, 1977.
- [84] S.-C. Lee and Y.-B. Chang. Fracture toughness and crack growth rate of ferritic and pearlitic compacted graphite cast irons at at 25 °C and 150 °C. *Metallurgical Transactions A*, 22(11):2645–2653, 1991.
- [85] A. Lion. Constitutive modelling in finite thermo-viscoplasticity: a physical approach based on nonlinear rheological models. *International Journal of Plasticity*, 16(5):469–494, 2000.
- [86] J.H. Liu, X.Y. Hao, G.L. Li, and G.S. Liu. Microvoid evaluation of ferrite ductile iron under strain. *Materials letters*, 56(5):748–755, 2002.
- [87] J.H. Liu, X.Y. Hao, G.L. Li, and G.Sh. Liu. Microvoid evaluation of ferrite ductile iron under strain. *Materials Letters*, 56:748–755, 2002.
- [88] G. Ljustina, M. Fagerström, and R. Larsson. Hypo- and hyper-inelasticity applied to modeling of compacted graphite iron machining simulations. *European Journal of Mechanics-A/Solids*, 37:57–68, 2013.
- [89] G. Ljustina, R. Larsson, and M. Fagerström. A FE based machining simulation methodology accounting for cast iron microstructure. *Finite Elements in Analysis and Design*, 80:1–10, 2014.
- [90] V.A. Lubarda. Constitutive theories based on the multiplicative decomposition of deformation gradient: Thermoelasticity, elastoplasticity and biomechanics. *Applied Mechanics Reviews*, 57(2):95–108, 2004.
- [91] T.S. Lui and C.G. Chao. High-temperature properties of ferritic spheroidal graphite cast iron. *Journal of Materials Science*, 24:2503–2507, 1989.
- [92] D.L. McDowell. A nonlinear kinematic hardening theory for cyclic thermoplasticity and thermoviscoplasticity. *International Journal of Plasticity*, 8(6):695–728, 1992.

- [93] J. Mediavilla, R.H.J. Peerlings, and M.G.D. Geers. A nonlocal triaxiality-dependent ductile damage model for finite strain plasticity. *Computer Methods in Applied Mechanics and Engineering*, 195(33):4617–4634, 2006.
- [94] B. Miao, D.O. North Wood, W. Bian, K. Fang, and M.H. Fan. Structure and growth of platelets in graphite spherulites in cast iron. *Journal of Materials Science*, 29(1):255–261, 1994.
- [95] A. Miller. An inelastic constitutive model for monotonic, cyclic, and creep deformation: Part I - equations development and analytical procedures. *ASME, Transactions, Series H-Journal of Engineering Materials and Technology*, 98:97–105, 1976.
- [96] W. M. Mohammed, E.G. Ng, and M.A. Elbestawi. On stress propagation and fracture in compacted graphite iron. *The International Journal of Advanced Manufacturing Technology*, 56(1):233–244, 2011.
- [97] W.M. Mohammed, E.G. Ng, and M.A. Elbestawi. On stress propagation and fracture in compacted graphite iron. *The International Journal of Advanced Manufacturing Technology*, 56(1-4):233–244, 2011.
- [98] W.C. Morgan. Thermal expansion coefficients of graphite crystals. *Carbon*, 10:73–79, 1972.
- [99] M. Muscalu and D. Fatu. Considerations on the thermal behaviour and oxidation resistance of cast iron. *Journal of Thermal Analysis*, 52:425–438, 1998.
- [100] T. Nakamura and S. Suresh. Effects of thermal residual stresses and fiber packing on deformation of metal-matrix composites. *Acta metallurgica et materialia*, 41(6):1665–1681, 1993.
- [101] J. Neggers, J.P.M. Hoefnagels, F. Hild, S. Roux, and M.G.D. Geers. Direct stress-strain measurements from bulged membranes using topography image correlation. *Experimental Mechanics*, 54(5):717–727, 2014.
- [102] M. Olsson, A.E. Giannakopoulos, and S. Suresh. Elastoplastic analysis of thermal cycling: ceramic particles in a metallic matrix. *Journal of the Mechanics and Physics of Solids*, 43(10):1639–1671, 1995.
- [103] I. Özdemir, W.A.M. Brekelmans, and M.G.D. Geers. Computational homogenization for heat conduction in heterogeneous solids. *International journal for numerical methods in engineering*, 73(2):185–204, 2008.
- [104] I. Özdemir, W.A.M. Brekelmans, and M.G.D. Geers. Fe2 computational homogenization for the thermo-mechanical analysis of heterogeneous solids. *Computer Methods in Applied Mechanics and Engineering*, 198(3):602–613, 2008.
- [105] I. Özdemir, W.A.M. Brekelmans, and M.G.D. Geers. A thermo-mechanical cohesive zone model. *Computational Mechanics*, 46(5):735–745, 2010.

- [106] K.B. Palmer. Creep Tests on a Flake Graphite Cast Iron at 300 °C. *BCIRA Journal*, 9(Report 603):537–539, 1961.
- [107] R.H.J. Peerlings, M.G.D. Geers, R. De Borst, and W.A.M. Brekelmans. A critical comparison of nonlocal and gradient-enhanced softening continua. *International Journal of Solids and Structures*, 38(44):7723–7746, 2001.
- [108] P. Perzyna. Thermodynamic theory of viscoplasticity. *Advances in Applied Mechanics*, 11:313–354, 1971.
- [109] J.C. Pina, V.G. Kouznetsova, and M.G.D. Geers. Thermo-mechanical analyses of heterogeneous materials with a strongly anisotropic phase: the case of cast iron. Submitted for publication.
- [110] J.C. Pina, S. Shafqat, V.G. Kouznetsova, Hoefnagels J.P.M., and M.G.D. Geers. Microstructural study of the mechanical response of compacted graphite iron: and experimental and numerical approach. Submitted for publication.
- [111] H. Pirgazi, S. Ghodrati, and L.A.I. Kestens. Three-dimensional EBSD characterization of thermo-mechanical fatigue crack morphology in compacted graphite iron. *Materials Characterization*, 90:13–20, 2014.
- [112] D.A. Porter, K.E. Easterling, and G.D.W. Smith. Dynamic studies of the tensile deformation and fracture of pearlite. *Acta Metallurgica*, 26(9):1405–1422, 1978.
- [113] P. Rodriguez and S.L. Mannan. High temperature low cycle fatigue. *Sadhana*, 20(1):123–164, 1995.
- [114] K. Roehrig. Thermal fatigue of gray and ductile cast irons. *Transactions of the American Foundrymen's Society*, 86:75–88, 1978.
- [115] B.W. Rosen and Z. Hashin. Effective thermal expansion coefficients and specific heats of composite materials. *International Journal of Engineering Science*, 8:157–173, 1970.
- [116] K.B. Rundman. Cast Irons. *Encyclopedia of Materials: Science and Technology*, pages 1003 – 1010, 2001.
- [117] R.A. Schapery. Thermal expansion coefficients of composite materials based on energy principles. *Journal of Composite Materials*, 2(3):380–404, 1968.
- [118] T. Seifert, G. Maier, A. Uihlein, K.-H. Lang, and H. Riedel. Mechanism-based thermomechanical fatigue life prediction of cast iron. Part II: Comparison of model predictions with experiments. *International Journal of Fatigue*, 32(8):1368–1377, 2010.
- [119] T. Seifert and H. Riedel. Mechanism-based thermomechanical fatigue life prediction of cast iron. Part I: Models. *International Journal of Fatigue*, 32(8):1358–1367, 2010.

- [120] G.F. Sergeant and E.R. Evans. Production and properties of compacted graphite irons. *Br. Foundryman*, 71(5):115–124, 1978.
- [121] S. Shao, S. Dawson, and M. Lampic. The mechanical and physical properties of compacted graphite iron. *Materialwissenschaft und Werkstofftechnik*, 29(8):397–411, 1998.
- [122] M.P. Shebatinov. A study of the fine structure of graphite inclusions in gray cast irons by means of the scanning electron microscope. *Metal Science and Heat Treatment*, 16(4):288–293, 1974.
- [123] Y.-L. Shen. Thermal expansion of metal-ceramic composites: a three dimensional analysis. *Materials Science and Engineering A*, 252:269–275, 1998.
- [124] Y.-L. Shen, A. Needleman, and S. Suresh. Coefficients of thermal expansion of metal-matrix composites for electronic packaging. *Metallurgical and Materials Transactions A*, 25(4):839–850, 1994.
- [125] T. Sjögren. *Influences of the graphite phase on elastic and plastic deformation behaviour of cast irons*. PhD Thesis, School of Engineering, Jönköping University, 2005.
- [126] T. Sjögren, D. Holmgren, and M. Rinvall. Study of the mechanical and thermal properties of pearlitic and ferritic cast iron matrices. *International Foundry Research/Giessereiforschung*, 59(3):14–21, 2007.
- [127] T. Sjögren, P.E. Persson, and P. Vomacka. Analysing the deformation behaviour of compacted graphite cast irons using digital image correlation techniques. *Key Engineering Materials*, 457:470–475, 2011.
- [128] T. Sjögren, P. Vomacka, and L.I. Svensson. Comparison of the mechanical properties in flake graphite and compacted graphite cast irons for piston rings. *International Journal of Cast Metals Research*, 17(2):65–71, 2004.
- [129] D. Steglich and W. Brocks. Micromechanical modelling of the behaviour of ductile materials including particles. *Computational Materials Science*, 9(1):7–17, 1997.
- [130] S. Suresh, A.E. Giannakopoulos, and M. Olsson. Elastoplastic analysis of thermal cycling: layered materials with sharp interfaces. *Journal of the Mechanics and Physics of Solids*, 42(6):979–1018, 1994.
- [131] M.A. Sutton, N. Li, D. Garcia, N. Cornille, J.J. Orteu, S.R. McNeill, HW Schreier, X Li, and AP Reynolds. Scanning electron microscopy for quantitative small and large deformation measurements Part II: experimental validation for magnifications from 200 to 10,000. *Experimental Mechanics*, 47(6):789–804, 2007.
- [132] M.A. Sutton, N. Li, D.C. Joy, A.P. Reynolds, and X. Li. Scanning electron microscopy for quantitative small and large deformation measurements Part I: SEM imaging at magnifications from 200 to 10,000. *Experimental Mechanics*, 47(6):775–787, 2007.

- [133] C.K. Syn, D.R. Leuser, O.D. Sherby, and E.M. Taleff. Stress-strain rate relations in ultra high carbon steels deformed in the ferrite range of temperature. *Materials Science Forum*, 426–432:853–858, 2003.
- [134] F. Szmytka, M.H. Maitournam, and L. Rémy. An implicit integration procedure for an elasto-viscoplastic model and its application to thermomechanical fatigue design of automotive parts. *Computers & Structures*, 119:155–165, 2013.
- [135] F. Szmytka, P. Michaud, L. Rémy, and A. Köster. Thermo-mechanical fatigue resistance characterization and materials ranking from heat-flux-controlled tests. Application to cast-irons for automotive exhaust part. *International Journal of Fatigue*, 55:136–146, 2013.
- [136] F. Szmytka, L. Rémy, H. Maitournam, A. Köster, and M. Bourgeois. New flow rules in elasto-viscoplastic constitutive models for spheroidal graphite cast-iron. *International Journal of Plasticity*, 26(6):905–924, 2010.
- [137] T. Takahashi and M. Nagumo. Flow stress and work-hardening of pearlitic steel. *Transactions of the Japan Institute of Metals*, 11(2):113–119, 1970.
- [138] Y. Takao and M. Taya. Thermal expansion coefficients and thermal stresses in an aligned short fiber composite with application to a short carbon fiber/aluminum. *Journal of Applied Mechanics*, 52(4):806–810, 1985.
- [139] K. Tsuzaki, Y. Matsuzaki, T. Maki, and I. Tamura. Fatigue deformation accompanying dynamic strain aging in a pearlitic eutectoid steel. *Materials Science and Engineering: A*, 142(1):63–70, 1991.
- [140] R.L.J.M. Ubachs, P.J.G. Schreurs, and M.G.D. Geers. Phase field dependent viscoplastic behaviour of solder alloys. *International Journal of Solids and Structures*, 42:2533–2558, 2005.
- [141] R.L.J.M. Ubachs, P.J.G. Schreurs, and M.G.D. Geers. Elasto-viscoplastic non-local damage modelling of thermal fatigue in anisotropic lead-free solder. *Mechanics of materials*, 39(7):685–701, 2007.
- [142] J. Van Beeck, J. Neggers, P.J.G. Schreurs, J.P.M. Hoefnagels, and M.G.D. Geers. Quantification of three-dimensional surface deformation using global digital image correlation. *Experimental Mechanics*, 54(4):557–570, 2014.
- [143] M.J. Van den Bosch, P.J.G. Schreurs, and M.G.D. Geers. An improved description of the exponential xu and needleman cohesive zone law for mixed-mode decohesion. *Engineering Fracture Mechanics*, 73(9):1220–1234, 2006.
- [144] A. Velichko, A. Wiegmann, and F. Mücklich. Estimation of the effective conductivities of complex cast iron microstructures using FIB-tomographic analysis. *Acta Materialia*, 57(17):5023–5035, 2009.

- [145] D.G. White. Growth and Scaling Characteristics of Cast Irons with Undercooled and Normal Flake Graphite. *BCIRA Journal*, 11(Report 689):223–230, 1963.
- [146] G. Winter, M. Riedler, R. Minichmayr, and W. Eichlseder. Cast iron versus aluminium cylinder head materials: their properties concerning to thermo-mechanical fatigue. *22nd DANUBIA–ADRIA Symposium on Experimental Methods in Solid Mechanics*, Monticelli Terme/Parma–Italy, Septmeber 28–October 1, 2005.
- [147] J.G.F. Wismans, L.E. Govaert, and J.A.W. Van Dommelen. X-ray computed tomography-based modeling of polymeric foams: The effect of finite element model size on the large strain response. *Journal of Polymer Science Part B: Polymer Physics*, 48(13):1526–1534, 2010.
- [148] J.G.F. Wismans, J.A.W. Van Dommelen, L.E. Govaert, H.E.H. Meijer, and B. Van Rietberg. Computed tomography-based modeling of structured polymers. *Journal of Cellular Plastics*, 45(2):157–179, 2009.
- [149] M. Wu and J. Campbell. Thermal fatigue in diesel engine cylinder head castings. In *One Hundred Second Annual Meeting of the American Foundrymen’s Society*, pages 485–495, 1998.
- [150] X-P. Xu and A. Needleman. Void nucleation by inclusion debonding in a crystal matrix. *Modeling and Simulation in Materials Science and Engineering*, 1:111–132, 1993.
- [151] V.M. Yuzvak, I.P. Volchok, and V.I. Gontarenko. Micromechanism of fracture of cast irons. *Metal Science and Heat Treatment*, 25(8):569–573, 1983.
- [152] C. Zener and J.H. Hollomon. Effect of strain rate upon plastic flow of steel. *Journal of Applied Physics*, 15(1):22–32, 1944.
- [153] C. Zener and J.H. Hollomon. Plastic flow and rupture of metals. *Transactions of ASM*, 33:163–235, 1944.
- [154] K.R. Ziegler and J.F. Wallace. The effect of matrix strucutre and alloying on the properties of compacted graphite iron. *Transactions of the American Foundrymen’s Society*, 92:735–748, 1984.

Acknowledgments

In January of 2009, my family and I embarked into a journey that lasted more than six years. They believed in me, and followed me without hesitation. Today, this journey is about to end, and although my family (in Eindhoven, in London, in Valence, in Santiago and in Mendoza) have been the backbone that provided me with the strength to reach the end, many people have contributed in several ways to the project, of which this thesis is the end result.

In first place, I am grateful to my promotor Marc Geers and copromotor Varvara Kouznetsova for giving me the opportunity to do my PhD at their group. During the last six years I have developed intellectually and grew as a person. You taught me to have a critical view on things, especially on my own work, and not to take anything for granted. Your insightful contributions and sharp comments were a fundamental contribution to this project. Besides my promotors, I am also grateful to Johan Hoefnagels and Ron Peerlings for their collaboration in different parts of my PhD project. I enjoyed working with you and appreciated your generosity.

I express my sincere gratitude to all the committee members, prof.dr.-ing. W. Bleck, prof.dr.ir. J.P. Ponthot, prof.dr. J. Sietsma and dr.ir. J.A. van Oijen, for their critical comments to this thesis and for their attendance to my defence.

I would like thank the Materials Innovation Institute for providing the funding for this project. Also, the collaboration from the people at the M2i office in all the administrative issues is gratefully acknowledged. In particular, I would like to thank Monica Reulink for helping my family and I to settle down in the Netherlands. Also, thanks for always been there to give a hand when needed.

Furthermore, I would like to acknowledge the contributions of our industrial partners, DAF Trucks N.V., and academic partners, TU Delft. Our discussions during the project meetings were always insightful and a source of inspiration for the project. Frank Mertens, Paul Steuten and Nico Kamperman from DAT Trucks N.V., it was a pleasure to meet you and work with you. I am also grateful to Jilt Sietsma, Leo Kestens, Michael Janssen, Ton Riemslog, Hans Hofman and Sepideh Ghodrat from TU Delft. Thank you for your valuable contributions to this project. Also, I would like to thank you for providing the facilities and the assistance to perform the elevated temperature test on pearlitic steels discussed in Chapter 4.

For her help in several issues that came along during the PhD I would like to thanks Alice van Litsenburg. Alice thanks a lot for your help, and for saving my desk for so long when I was no longer at the TU/e. I am also grateful to Leo Wouters for his help in all computer related matters. Thank you for your patience and understanding, in particular in the last part of my PhD.

Although the nature of this project was initially pure numerically, in the end several tests were carried out for this thesis. To this end, the help of Marc van Maris was extremely valuable. Marc thanks for your help and creative ideas. It was great fun working with you, as well as our technical and non-technical talks.

I am very thankful to all my students Leo, Daan, Luuk, Maurice and Salman for their valuable contributions to this thesis. Salman, thanks for your positive and proactive attitude. What some time back started as an internship project, lead to Chapter 3 of this thesis.

Also, I would like to thank Benoit Blaysat and Lambert van Breemen for their help in tackling the numerical problems in the implementation of the exponential and hyperbolic equations of the model discussed in Chapters 4 and 5.

To all my friends and colleagues at the TU/e, thanks for the good times at dinners, conferences, meetings, courses and at the coffee corner. Lars and Elitsa, thanks for your friendship. We enjoyed your company during dinners and BBQs, either if you were on your own or with any of your kids (Kim or Leong Hien). Lars thanks as well for the comments on the first and last chapters of this thesis. Nilgoon and Hadi, Emanuela and Ricardo, Rudy, Kim, Leong Hien, Benoit, Bart and Hamid thank you for the good times and thoughtful talks during dinners, BBQs and drinks. I would also like to thank my MoM colleagues and roommates: Salman, Jeroen, Cem, Erica, Gwen, Rene, Mary, Paul, Bart, Lambert, Jan, Francesco, Salman, Faizal, Peter, Michael, Murthy, Sol and Juan. Furthermore, I am grateful to our friends from the ISE (Molly and Kai, Elia and Roberto, Colette and Luc, Kriztina and Cristian, Alicia and John, Barbara and Fabio) for being there for my family during the past six years.

Por estar siempre presente a pesar de la distancia, quiero agradecer a la gran familia Pina-Molinari: a mis hermanos, Sol, Ine, Juan Andrés, Juan Esteban, María, Tito, Merce, Mari, Bertrand, Martín y José, y sobrinos, Ofé, Lucas, Justi, Juan Cruz y Guille. Mamá y papá, gracias por darme absoluta libertad para perseguir mis sueños. De ustedes aprendí a mirar siempre para adelante y no darme por vencido a pesar de las vaivenes que presenta el camino. Gloria y Juan, mis muy queridos "*bellos padres*", les agradezco hacerme sentir como un hijo más, y dejarme "*robarles*" a dos de sus princesas. Al igual que mis padres, su apoyo incondicional nos dio la fuerza para superar las dificultades que se presentaron en estos seis años.

Finalmente, quiero agradecer a las tres personas que me acompañaron día a día en esta aventura: Juanqui, Juana y Gabi. Juani Juani, tu espíritu indomable hizo posible que, a pesar de tantos cambios a tu temprana edad, nunca perdieras tu inmensa alegría de vivir y tu sonrisa. Juanqui, llegaste a mitad de camino y sumaste tu desbordante energía y felicidad. Gabi, gracias por seguirme en esta locura. Espero algún día poder devolverte algo de todo lo que me has dado. Esta tesis es tanto tuya como mía; jamás la hubiera terminado sin vos a mi lado. Gracias por empujarme cuando ya no encontraba ni fuerza ni razones para seguir. Gracias por tu cariño, amor y generosidad. Gracias por creer en mí, gracias por estar a mi lado, gracias por hacerme tan feliz.

Juan Carlos Pina
Veldhoven, March 2015

Curriculum Vitae

Juan Carlos Pina was born on the 8th of September 1979 in Mendoza, Argentina. After finishing the secondary school in 1997 at the Colegio San José de los Hermanos Maristas, he studied Civil Engineering at the Universidad Nacional de Cuyo in Mendoza, Argentina. In March 2005 he graduated majoring in structural engineering. Between December 2004 and July 2005 he was employed at Camps & Partners as a Junior Structural Engineering. From July 2005 to September 2007 he worked at Industrias Metallúrgicas Pescarmona S.A. as a Mechanical/Structural Design Engineering. During this period he was involved in the design of hydromechanical equipment for hydroelectric power plants. In October 2007, Juan Carlos went to the University of Swansea in Wales, for a Master degree in Computer Modelling and Finite Elements in Engineering Mechanics. In 2009, he graduated with Distinction within the Civil and Computational Engineering Centre with the thesis entitled “Yield strength of porous material - A multi-scale approach”, under the supervision of prof. E.A. de Souza Neto. After graduating, he started a PhD at the Eindhoven University of Technology in the Mechanics of Materials group under the supervision of prof.dr.ir. M.G.D. Geers and dr.ir. V.G. Kouznetsova. The title of his PhD project was “Microstructure-based material model for thermo-mechanical fatigue of cylinder heads” of which the results are presented in this dissertation. Since June 2013 he works as a Mechanical Analyst at ASML.

